1-1-2018

The Process-Structure-Property Relationships of a Laser Engineered Net Shaping (LENS) Titanium-Aluminum-Vanadium Alloy that is Functionally Graded with Boron

Denver W. Seely

Follow this and additional works at: https://scholarsjunction.msstate.edu/td

The process-structure-property relationships of a laser engineered net shaping (LENS)

titanium-aluminum-vanadium alloy that is functionally graded with boron

By

Denver W. Seely

A Dissertation
Submitted to the Faculty of
Mississippi State University
in Partial Fulfillment of the Requirements
for the Degree of Doctor of Philosophy
in Mechanical Engineering
in the Bagley College of Engineering

Mississippi State, Mississippi

May 2018

The process-structure-property relationships of a laser engineered net shaping (LENS)

titanium-aluminum-vanadium alloy that is functionally graded with boron

By

Denver W. Seely

Approved:

_____
Mark F. Horstemeyer
(Major Professor/Director of Dissertation)

_____
Hongjoo Rhee
(Minor Professor)

_____
Haitham El Kadiri
(Committee Member)

_____
Haley R. Doude
(Committee Member)

_____
Yucheng Liu
(Graduate Coordinator)

_____
Jason M. Keith
Dean
Bagley College of Engineering

Name: Denver W. Seely

Date of Degree: May 4, 2018

Institution: Mississippi State University

Major Field: Mechanical Engineering

Director of Dissertation: Mark F. Horstemeyer

Title of Study: The process-structure-property relationships of a laser engineered net shaping (LENS) titanium-aluminum-vanadium alloy that is functionally graded with boron

Pages in Study 103

Candidate for Degree of Doctor of Philosophy

In this study, we quantified the Chemistry-Process-Structure-Property (CPSP) relations of a Ti-6Al-4V/TiB functionally graded material to assess its ability to withstand large deformations in a high throughput manner. The functionally graded Ti-6Al-4V/TiB alloy was created by using a Laser Engineered Net Shaping (LENS) process. A complex thermal history arose during the LENS process and thus induced a multiscale hierarchy of structures that in turn affected the mechanical properties. Here, we quantified the functionally graded chemical composition; functionally graded TiB particle size, number density, nearest neighbor distance, and particle fraction; grain size gradient; porosity gradient. In concert with these multiscale structures, we quantified the associated functionally graded elastic moduli and overall stress-strain behavior of eight materials with differing amounts of titanium, vanadium, aluminum, and boron with just one experiment under compression using digital image correlation techniques. We then corroborated our experimental stress behavior with independent hardening experiments. This paper joins not only the Process-Structure-Property (PSP) relations, but couples the different chemistries in an efficient manner to effectively create the CPSP relationships

for analyzing titanium, aluminum, vanadium, and boron together. Since this methodology admits the CPSP coupling, the development of new alloys can be solved by using an inverse method. Finally, this experimental data now lays down the gauntlet for modeling the sequential CPSP relationships.

DEDICATION

To my God: You have created me in Christ Jesus unto good works, let me now walk in them. You have called me to be a soldier, let me not entangle myself with the affairs of this world that I may please You. You have called me to enjoin a battle not again flesh and blood, but against the principalities and powers in of this present darkness. The weapons I now forge are not carnal, but mighty through You; for tearing down of strongholds that exalt themselves against the knowledge of You; to take captive every thought to the obedience of Your Son. Your salvation is my helmet, Your Truth girds about me as a belt, I trust only in Your righteousness for my body armor, and I will wear the boots you have prepared for me to take the Good News to all held captive. Let me wield the shield of faith to compass and protect all you bring under my charge. When last I breathe this mortal air let it be said, "All God's words are true".

To my dear Jenny: you have walked with me on this journey and kept your promise to see me through the changes as the crucible removed dross and the forge imparted shape. May my heart be ever soft toward you in the solace of our garden, and let my arms be a wall of iron around our home.

To my children: as you have been a support to me in this training, I will now be a foundation for you.   It is for you and your generation that I began this labor. As I was prepared as a gift by my parents to a generation they will not see, so now I will prepare you to serve and join others in bringing the Good News.

To my parents Donald and Julie: Donald, although I surpassed you in volume of learning, the things of most importance, I learned in your house. Julie, you are my first and greatest cheerleader. No reward can ever repay the price of your investment in me.

To all that have enabled freedom of choice in education despite government opposition, you are the ground on which I stand.

To all that still long for freedom of choice in education both for themselves and their children, I pledge to be your champion.

ACKNOWLEDGEMENTS

TABLE OF CONTENTS

LIST OF TABLES

LIST OF FIGURES

x

AN ANALYSIS OF FUNCTIONALLY GRADED TITANIUM BASED ALLOY

ARMOR FOR MAXIMIZING ENERGY ABSORPTION

1.1 Introduction

Armor is used to protect equipment and personnel against disruptive energy. The agent of delivery of the disruptive energy may be a projectile, blast wave, chemical, and others. Armor systems can be subdivided into personal protective armor and equipment protective armor. The principle of protection of interest in this paper may be applied to both personal and equipment armor systems. There are several strategies for defeating armor systems depending on the disrupting objective after passing primary layer. These strategies include solid penetrator, spallation, explosively formed penetrator, and a few others. The primary threats for equipment armor under consideration in this work are penetrator and spallation. The history of different armor materials is presented in Figure 1.1.
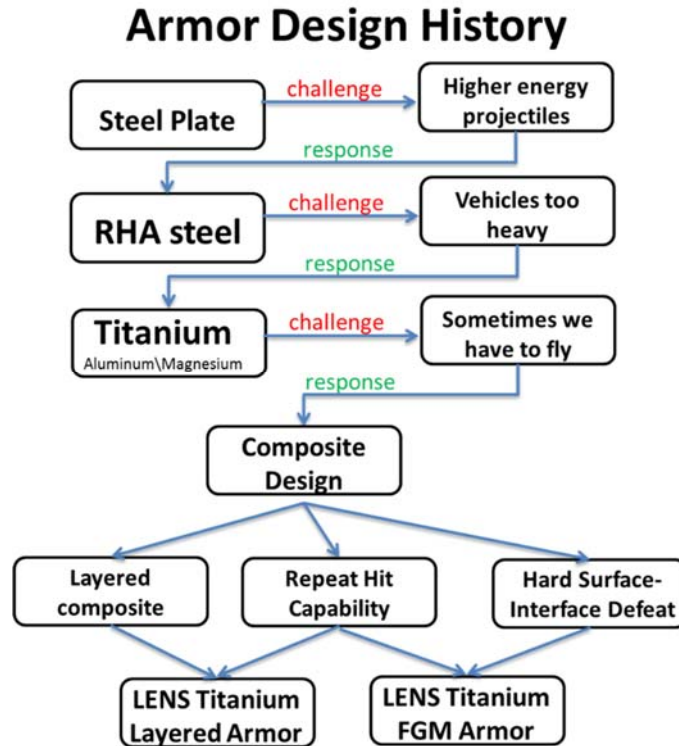
Figure 1.1   The design progression of armor from early steel plate to current composite titanium designs

1.1.2   The use of steel in armor

Rolled homogeneous armor (RHA) has been the standard military armor plate in use since WWII. This is a ductile steel alloy with a predictable performance against threats ranging from conventional small caliber munitions to large caliber armor piercing rounds. Armor assemblies are designed around mitigating the highest foreseeable threat, consequently, as the threat level increases, the required thickness of RHA increases along with the total weight of the armor assembly.

1.1.3   The search for lightweight alternatives

There are circumstances when the additional weight of the combat protective system interferes with either a vehicle functional constraint or mission constraint. A

vehicle that requires air-lift into a theater of operation is an example of a mission constrained by the logistic considerations of aircraft cargo capacity. Consequently, the offices of the U.S. Department of Defense are seeking lightweight alternative solutions to the range of known threats.

The weight reduction objective of the Army Research Laboratory is focused on metal matrix composites (Chin 1999). The order of plates affects the ballistic protection of an ordered armor system (Ben-Dor, Dubinsky et al. 1999).

1.1.4 The basis for alternative material system selection

A ballistic limit plot for armor shows the velocity of a standard projectile versus the thickness of a material necessary to prevent full or partial penetration. A critical factor in the design of protective armor systems is the ratio of the weight of the armor to its impact absorbing capacity. Because the armor is generally implemented in the form of plates of uniform thickness, the metric used is termed areal density which is the thickness of the plate, t, multiplied by the density, ρ. The formula for areal density is $A = \rho * t$. For some armor applications, maximizing this design variable is the most important consideration in design optimization. While a variety of steels have been used in armor systems successfully over the years, the weight of iron as the primary material has limited absorption to weight ratio. Figure 1.2 shows a comparison of the velocity limit versus the areal density for selected materials (RHA steel, Aluminum, and Ti6Al4V). Figure 1.2 illustrates why changing the base material to titanium for ballistic protection improves the energy absorption to weight ratio.
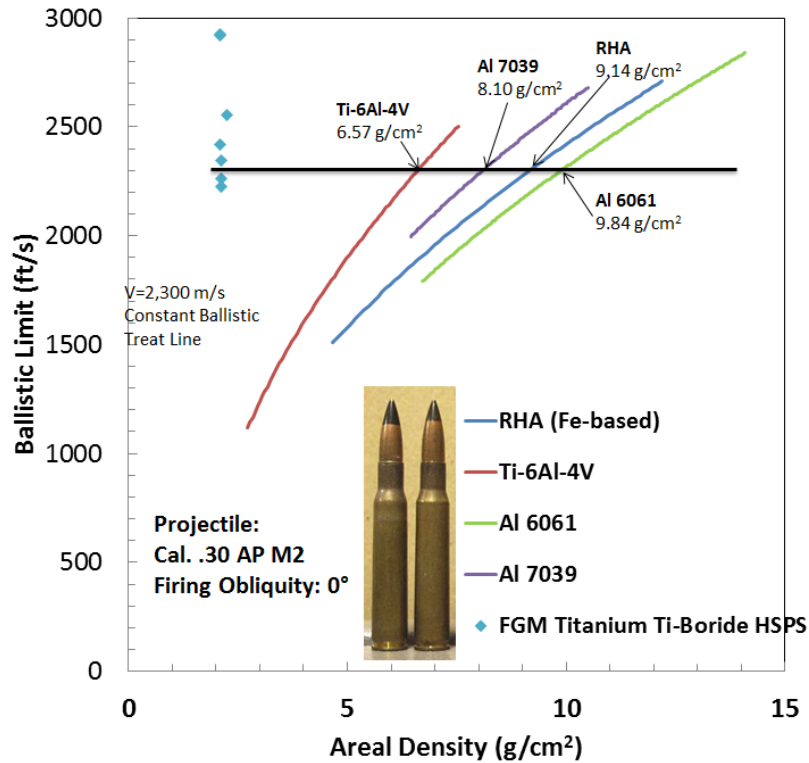
Figure 1.2   Ballistic limit versus areal density comparison for Cal .30 AP M2 armor piercing projectile.

The horizontal line shows areal density required for protection from the same threat for 4 different materials: Ti6Al4V, Al 7039, RHA, Al 6061.

1.1.5   Fabrication process for hierarchical metal structures

The LENS fabrication process can be applied to achieve a hierarchical structure. Laser Engineered Net Shaping (LENS) is a fabrication process whereby material is added to a part by melting a pool (called a weld pool) on the surface with a focused laser beam and then injecting a stream powdered filler material into the molten pool at the focal point of the beam. The laser continues to heat the weld pool enough to mix with and melt the injected powder. As the laser moves to heat another location, the weld pool cools and solidifies along with the added material.   A computer numerical controlled (CNC) table moves the part beneath the focal point of the laser beam and powder stream allowing

precise placement of the new material. In addition to controlling the placement of new material on the part, the LENS system can also control the type of material added by selecting which powder to inject into the weld pool. This capability of selectively controlling filler material can be used to vary the composition of a part from location to location by changing the powder.

1.2   Current State

1.2.1   History of steel in Armor

The use of iron in combat armor application has been closely linked with mobility since its first use in the American Civil War to protect naval vessels. Both parties utilized iron to defeat projectile threats, earning them the moniker Ironclads. The Confederate vessel, the C.S.S. Merrimac utilized iron plate above the waterline, inclined at an angle with wood plank backing and supported on a wooden substructure. The Union vessel, the U.S.S. Monitor implemented a low profile iron deck and employed a round iron turret to house cannons, relying on the curvature of the turret to both stiffen the structure and deflect projectiles. Both designs were superior in mitigating projectile threats in contest with contemporary conventional vessels. In direct contest with each other, the defeat of projectiles was so effective that tactical use of cannon fire was virtually nullified and engagements were resolved by superior maneuvers.

In the era of mechanized war, the protection of mobile combat equipment and personnel took on increased importance. Steel saw widespread use as a structural material during World War I for naval vessels and land vehicles, and limited application for armor in vehicles. A layer of steel 10 mm thick could defeat most infantry munitions. By the

advent of World War II, the kinetic energy of penetrators increased significantly

requiring counter increase in frontal armor thickness (Crouch 1988).

1.2.2   History of Titanium alloys as an armor material

The Titanium alloy Ti6Al4V was first developed in the United States in the

1940's as a dual phase alloy. The pure metal is allotropic with a phase transition

temperature of 872 degrees °C. Alloys that decrease the transition temperature are called

Beta stabilizers. Alloys that increase the transition temperature are called alpha

stabilizers, because they stabilize the alpha phase at high temperatures. Alloys that

contain both alpha and beta stabilizing elements are called alpha + beta alloys. Ti6Al4V

contains the alpha stabilizing element Aluminum and the Beta stabilizing element

Vanadium. Ti6Al4V is also called a dual phase alloy because after proper heat treatment,

a dual phase structure can be obtained which is stable down to room temperature.

Because titanium can undergo a martensitic phase transformation from BCC beta to HCP

alpha prime under high cooling rates, an alloy containing beta stabilizers will also reduce

the starting temperature of martensitic transformation. If sufficient alloy is added to

stabilize the beta phase to room temperature, then the martensitic transformation can be

avoided entirely. Consequently, if rapid cooling rates are unavoidable and a martensitic

structure is undesirable, then a beta alloy can be employed to meet design objectives.

Mechanical behavior of alpha phase and beta phase differ. Because of the dual phase

capability of Ti6Al4V, a microstructure can be achieved that improves the overall

ductility and fracture toughness compared to a microstructure of only alpha or only beta.

1.2.3   Mechanisms of armor defeat

There are two typical mechanisms for armor defeat. One is a shock wave impact, the next is a penetrator like an explosively formed projectile (Zukas, Nicholas et al. 1983, Zukas, Walters et al. 2002). The shock wave impingement onto armor is a diffuse attack such that the wave dissipation is the key in defeating the threat. When a penetrator strikes armor, the key if defeating the threat is to break up the projectile.

1.2.4   History of laminated materials

Bonded laminated metal plates were investigated by Woodward et al. (Corbett, Reid et al. 1996) Alternating layers with less than 1 mm alternating laminations of Ti6Al4V and TiAl$_3$ have been fabricated using metal-intermetallic laminate (MIL) method. This MIL structural assembly suffers from shrinkage cracking upon cooling from processing temperatures due to differences in thermal expansion coefficients between the layer constituents (Li, Olevsky et al. 2008).

1.2.5   History of functionally graded materials

The use of two different materials in a mechanically coherent system can produce a condition of incompatibility at the interface between the two materials. The incompatibility may arise during fabrication and manifest as reduced performance. When the selection of each material is constrained by a functional material requirement in a specified region, then the designer must find a means to maintain compatibility between the regions. One approach is to arrange the material in such a way that the aggregate material properties change slowly from one region to the other. This is called a functionally graded material.

1.2.6   History of using borides in titanium

Borides of Titanium have high modulus (4x greater) (Munro 2000), high hardness (3x greater) and coefficients of thermal expansion compatible with Titanium alloys. (Gorsse and Miracle, 2003)

Table 1.1   Mechanical properties of a titanium and titanium borides

	Titanium	TiB	TiB$_2$
Young's Modulus	~109 GPa	482 GPa	550 GPa
Hardness	3-4 GPa	28 GPa	30 GPa

The high hardness and modulus of Titanium monoboride suggest that it would be a good candidate for the hard layer of a composite armor system. Because of the compatible thermal properties, delamination of adjacent layers of Titanium and TiB by large temperature range of fabrication processes may be minimized.

Lepakova et al. (Lepakova, Raskolenko et al. 2000) prepared titanium boride phases by self-propagating high-temperature synthesis (SHS). Wang and Thompson (1999) produced a TiB$_2$ plate by self-propagating high-temperature synthesis and dynamic compaction (SHS-DC) with high density (99.3%) and large grain size (18 ± 3 μm). TiB has been fabricated by elemental powder spark plasma sintering (SPS)(Feng, Meng et al. 2005, Gupta, Basu et al. 2012), laser coating (Galvan, Ocelík et al. 2004), LENS pre-alloyed Ti64 and elemental boron (Genç, Banerjee et al. 2006).

1.2.7   History of LENS materials

The LENS method of material fabrication was introduced in the year 2002 (Gill 2002) as a method of consolidating powders by laser fusion. This process allows for the selective placement of material. In 2003 the LENS process was modified to allow

selective mixing of the feed powders. This allows for both selective placement and selective composition of material in a fully dense deposit.

1.2.8   Current state of modeling layered and FGM armors

Simulations of functionally graded material have been performed using the hydrocode EPIC using the material system AlN and Aluminum. The Johnson-Holmquist-Beissel ceramic model (JHB) material model was used for the brittle AlN and the Johnson Cook (JC) strength and fracture model was used for the metal. Kleponis et al. (2000) performed impact calculations using the solid-mechanics wave-propagation code CTH. They applied the Johnson Cook Material Model to a layered composite with initial material parameters of rolled homogeneous armor (RHA) as the softer layer and a coefficient modified RHA as the hard layer.   Kleponis suggested that the long standing design paradigm of placing the hardest layer on the outside as the first contact encountered by the penetrator may not be the optimal choice of topological arrangement of functionally graded layers. Birman et al. (Birman and Byrd 2007) presents a review of recent developments (2000-2007) in FGM among which are heat transfer, stress, dynamic analyses, testing, manufacturing and design, and fracture. Jha et al. (Jha, Kant et al. 2013) present a critical review of recent research on functionally graded plates.

Li and Meyers (Li, Olevsky et al. 2008) used ABAQUS to simulate cracking in Ti-6Al-4V-Al3Ti layered laminate driven by residual stress from cooling from a process temperature of 1023K.

1.2.9 Material Models applied to Ti-6Al-4V

The stress state dependence of Ti6Al4V alloy has been studied to understand its plasticity and fracture. Nemat-Nasser et al. (Nemat-Nasser, Guo et al. 2001) calibrated a material model to experimental data for conventional and hot isostatic pressed Ti6AlV4 under compression covering a range of strain rates. Peirs et al. (Peirs, Verleysen et al. 2011), Liu et al. (Liu, Siad et al. 2009, Liu, Tan et al. 2009) conducted high strain rate experiments under simple shear. Hammer et al. (Hammer, Yatnalkar et al. 2013) conducted high strain rate experiments under tension.

CHAPTER II

THE PROCESS-STRUCTURE RELATIONSHIPS OF A LASER ENGINEERED NET

SHAPING (LENS) TITANIUM-ALUMINUM-VANADIUM ALLOY THAT IS

FUNCTIONALLY GRADED WITH BORON

2.1   Abstract

We quantify the chemistry-process-structure relations of a titanium-aluminum-

vanadium alloy in which boron was added in a functionally graded assembly through a

Laser Engineered Net Shaping (LENS) process. This particular alloy system is used for

structural applications. The material gradient was made by pre-alloyed powder additions

to form an *in situ* melt of prescribed alloy concentration. The multiscale complex

heterogeneous structures arising from the LENS thermal history is discussed, and a new

term is proposed "Borlite," which is a eutectic structure containing orthorhombic titanium

monoboride (TiB) and titanium The β titanium grain size nonlinearly decreased until

reaching a saturation of approximately 100 μm when the boron weight fraction reached

0.3%. Similarly, the transformed α titanium grain size nonlinearly decreased until

reaching a saturation level, but the grain size was approximately 2 μm when the boron

weight fraction reached 0.6%. Alternatively, the α titanium grain size increased

nonlinearly from 1 to 5 μm as a function of the aluminum concentration increasing from

0% to 6% aluminum by weight and vanadium increasing from 0% to 4% by weight.

Finally, the cause-effect relations related to the creation of unwanted porosity was

11

quantified, which can help in further developments of additively manufactured metal alloys such as this one used LENS processing.

2.2   Introduction

Additive Manufacturing (AM) is currently very popular. Design engineers want the advantage of quickly moving information from a 3D CAD file to a finished part using a rapid prototyping paradigm which AM provides over the traditional bulk material subtractive machining processes or long lead time casting processes. The AM objective is to reduce the iteration time of the design cycle. For metal based AM, the laser metal sintering process was the first to achieve net shape geometries from 3D CAD files (Griffith *et al.,* 1996), but high porosity levels limited mechanical product applications constrained by fatigue performance (Xue *et al.,* 2010). Hence, understanding the role of heterogeneous microstructures and in particular porosity becomes an important focus for AM processing. Improvements in process control have brought metal AM parts from the role of prototyping in the design cycle to fully functional, and in some applications, finished parts (Grujicic *et al.,* 2001).

The typical metals used for AM include Ti-6Al-4V (Kobryn and Semiatin 2001), 316 SS (Griffith, Schlieriger *et al*. 1999), Inconel (Grujicic, Hu *et al*. 2001), SS410 steel (Wang, Felicelli *et al*. 2008), and H13 tool steel (Griffith, Schlieriger *et al*. 1999). Candidate metals used for metal AM are typically drawn from known alloys systems, because much is already known about them from years of use, and quality feed stock are available from which to produce powders. When selecting a material for AM product design, constraints for material properties such as corrosion resistance or high temperature performance can impose pressure for selection of known alloy families;

12

however, many alloys derive their desirable properties from a specific processing history chosen to achieve a finished microstructure. The advantage of using the AM process is to achieve a desired net shape in a single step that may be lost if subsequent processing is required to meet a certain property or performance objective.

Powder bed methods have since improved process control to minimize pore defects enabling near fully dense parts with material properties approximating rapid solidification. Process control development has now been shifted to predictively control solidification rates to achieve a preferential microstructure. With a catalog of process parameters such as laser power, scan speed and pattern, hatch spacing, and beam shape correlated with a predictable microstructure, laser based additive manufacturing methods present the possibility to selectively tailor location specific microstructures. Powder-bed fusion methods have typically been limited to a single powder composition.

Blown powder AM methods (Gu, Meiners *et al*. 2012) add an additional degree of freedom: chemical composition. By integrating multiple feeders, powder metals of varying composition can be blended in the melt pool to achieve an *in situ* composition of choice. Elemental powders and pre-alloyed master alloys have been used.

The challenge with fusion based powder metal AM methods is adding a predictable and controlled deposition layer of material. The thickness of the deposition layer is important for tool path planning. Because most AM methods use the planar slice method to build a 3D geometry, variations in slice thickness can be affected. Powder bed methods maintain control of layer thickness by establishing a new layer of unconsolidated powder whose upper surface is planar with a regular prescribed offset distance and whose lower surface follows the surface contour of the previous layer melt

13

surface. The depth of powder as measured from the upper plane may vary, following process features from the previous layer such as dips and peaks from hatch pattern variations. Each layer fusion cycle may produce variations in deposition height locally, but deposition layer thickness variations are compensated on successive layer passes.

Fusion based blown powder methods are vulnerable to cumulative variations in the deposition thickness. Consequently, great care must be taken to ensure that the effect of processing variables on the deposition thickness is characterized. The LENS method makes use of a strategy to minimize cumulative departures from a planned geometry called a deposition zone. Powder flow is directed into the deposition zone such that the mass flow varies with respect to the relative location along the laser beam axis. If too much material is added to the melt pool on a given deposition pass (a condition called overbuilding), then successive layer surfaces will intersect the deposition zone higher along the beam axis and receive less powder mass flow, thereby reducing the material addition rate. If too little material is added to the melt pool (a condition called underbuilding), then successive layer surfaces will intersect the deposition zone lower along the beam axis and receive more powder mass flow, thereby increasing the material addition rate. This form of intrinsic process feedback control provides flexibility to use an open loop prescribed motion tool path. Deposition parameters are chosen to maintain a mass addition rate with an expected deposition thickness that maintains the build within the center of the deposition zone.

In this paper, the LENS method is employed in order to create a Functionally Graded Material (FGM) to provide understanding of the fabrication complexities related to the process-structure relationship. The use of two different

14

materials in a mechanically coherent system can produce a condition of incompatibility at the interface between the two materials thus affecting the deposition rate and in turn the control system causing uncertainties in the following microstructures. The incompatibility can arise during fabrication and manifest different microstructures that reduce the properties of interest and hence the performance. When the selection of each material is constrained by a functional material requirement in a specified region, then the designer must find a means to maintain compatibility between the regions. One approach is to arrange the material in such a way that the aggregate material properties change slowly from one region to the other. This is called an FGM.

Our specific intent was to add borides of titanium into a Ti-6Al-4V alloy in an FGM manner. Borides of titanium have high modulus (4x greater), high hardness (3x greater) and coefficients of thermal expansion compatible with titanium alloys. The high hardness and modulus of titanium monoboride suggest that it would be a good candidate for the hard layer of a composite armor system. Because of the compatible thermal properties, delamination of adjacent layers of titanium and TiB by large temperature range of fabrication processes may be minimized.

There have been different methods by which TiB has been added to a base alloy. Lepakova *et al.* [2000] prepared titanium boride phases by a self-propagating high-temperature synthesis. Wang and Thompson [1999] produced a TiB_2 plate by self-propagating high-temperature synthesis and dynamic compaction (SHS-DC) with high density (99.3%) and large grain size (18 ± 3 μm). TiB has been fabricated by elemental powder spark plasma sintering (SPS) (Feng *et al.,* 2005; Gupta *et al.*, 2012), laser coating

(Galvan *et al.* 2004), LENS pre-alloyed Ti-6Al-4V, and elemental boron (Genc *et al.*, 2006).

The contribution of our work is the complete description of the complicated multilayered LENS process when an FGM, such as Ti-6Al-4V and TiB, are produced. The FGM is made in order to create a microstructurally graded material and then hence a mechanical property graded material as illustrated in the schematic in Figure 2.1 [Seely *et al.,* 2018]. The next section describes the materials processing of the LENS method with the characterization of the multiscale structures. Section 3 describes the microstructural results, and Section 2.4 offers a description of the important process-structure features. Finally, some conclusions are drawn in Section 2.5.
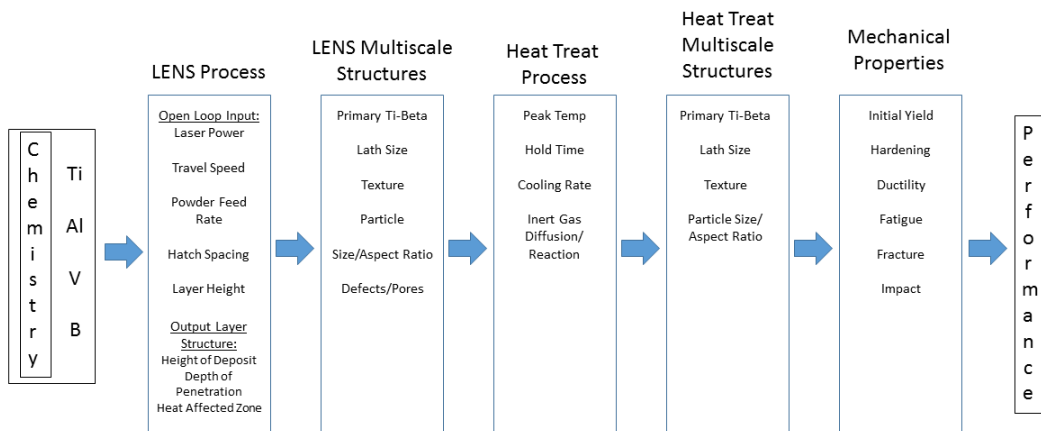
Figure 2.1   Chemistry, Process, Structure, Property, Performance Diagram for the Laser Engineered Net Shaping (LENS) additive manufacturing process.

2.3   Processing Method of LENS for the Titanium-Aluminum-Vanadium-Boron Functionally Graded Materials

Two pre-alloyed spherical powders were used to make specimens with compositions of Ti-6Al-4V and Ti-1B (1 weight percent Boron) on a 1/4-in thick commercially pure titanium base plate with a LENS 750 machine. The hatch spacing was 0.015 inches, and the travel speed was 20 inches/min. The powder flow was coordinated by the mass flows proportioned between the two powder feeders as shown in Figure 2.2. Note from Figure 2 that the deposition height, h_d, is different from the depth of penetration, d_p, and depth of the heat affected zone, d_{HAZ}. A functional grade in composition was prescribed in eight layers. Layer 1 started with 100% Ti-6Al-4V powder from feeder #1. Layer 2 decreased the flow rate of Feeder #1 to 90% Ti-6Al-4V and raised the flow rate to 10% Ti-1B powder from Feeder #2, and so on through Layer 8. By trial-and-error, the operator selected a laser power level that provided satisfactory melting for both individual powder types, then the same laser power and travel speed settings were applied for all eight composition layers.
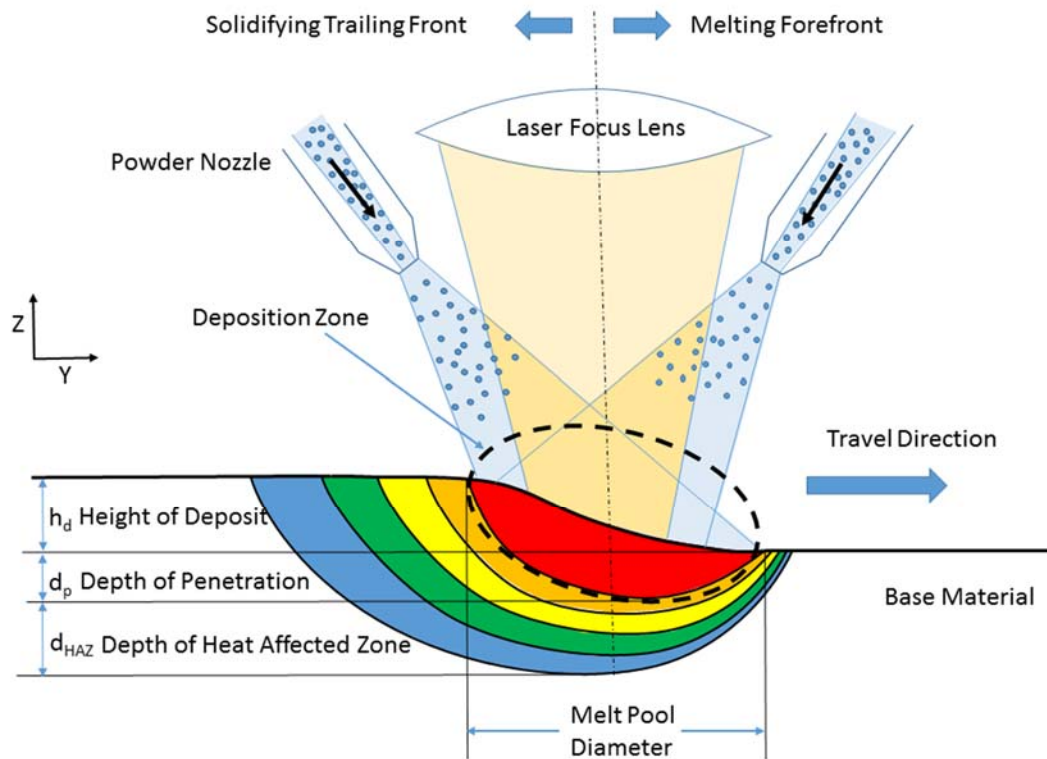
Figure 2.2   The traveling deposition zone of the LENS blown powder method.

Schematic of the traveling deposition zone of the LENS blown powder method. The base material is either a starting material or a previous layer and is fixed. The deposition head travels to the right relative to the base material as in this schematic. The dotted line represents the melt region, where the red color is the hottest region under the laser focal spot. The amount of the powder filler material determines the height of the deposition pass. The melt pool diameter is a function of the laser power and travel speed, which in turn affects the depth of penetration and the heat affected zone. The melting forefront experiences a different thermal history than the solidifying trailing front that generates a different microstructure.

The multiple layer FGM described herein is illustrated schematically in Figure

2.3. Figure 2.3a shows the different layer methodology, while Figure 2.3b shows the

hatch pattern for each layer. There also can be several passes for each layer illustrated in

Figure 2.3. Each of the eight layers had a rotated direction for the hatch patterning as

well as the different amount of TiB added to the Ti-6Al-4V. Note in Figure 2.3c that the

pattern rotated 45 degrees for each layer. Figure 2.3d illustrates the different amounts of

TiB that were included in each layer, which were each approximately 0.062 inches thick.
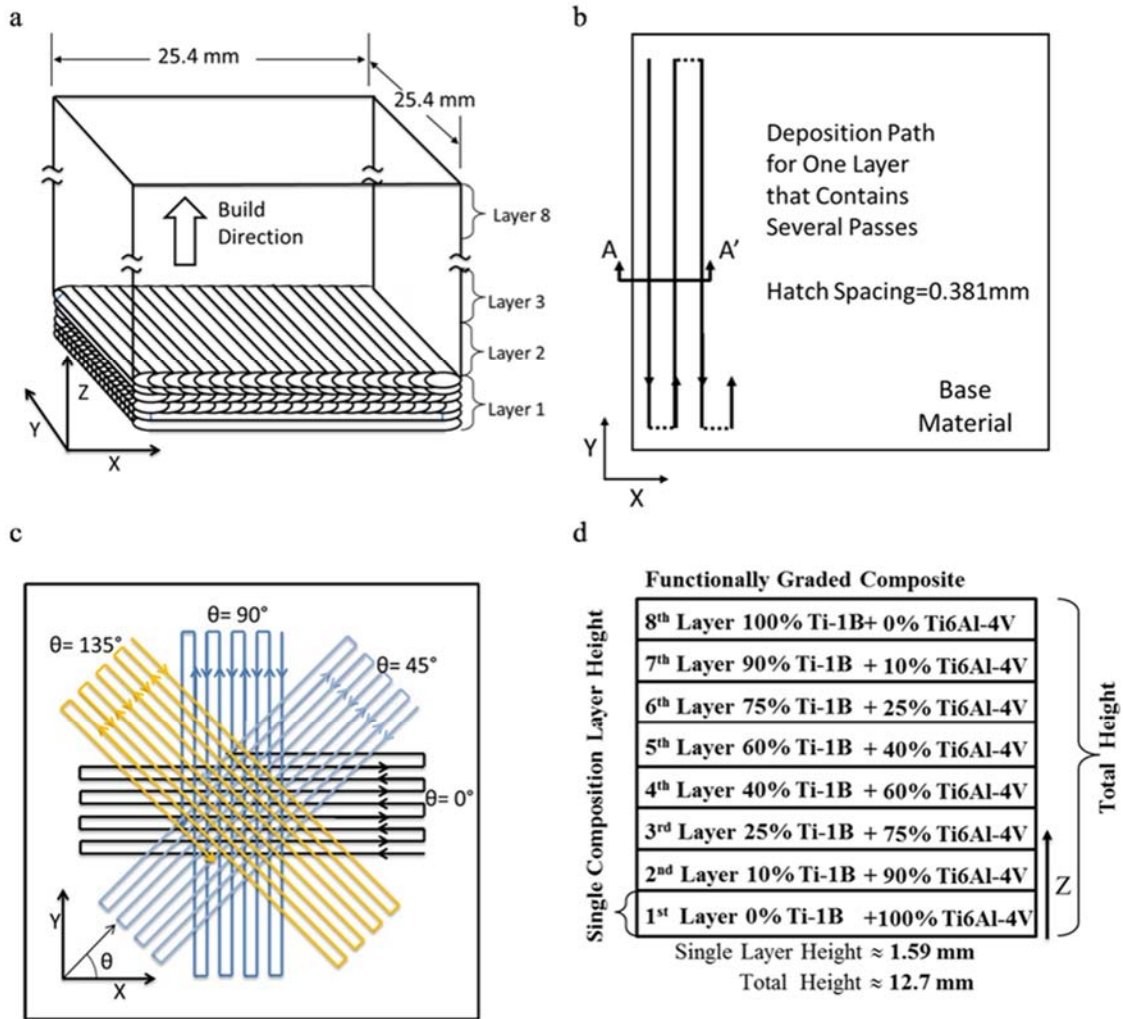
Figure 2.3   The processing steps of the Laser Engineered Net Shaping (LENS) method.

Schematic showing the processing steps of the Laser Engineered Net Shaping (LENS) method: a) Diagram of build tool path, b) the in-plane linear hatch pattern showing hatch spacing, c) the changing layer direction with each layer comprising six passes (all six are not shown in the schematic), and d) the eight layers (0.062-inch thickness per layer).

Changes in the bulk chemical composition of the deposited material affect deposition process features at the macroscale. The dotted line in the schematic in Figure 2.2 divides the deposition zone into the melting forefront (in the direction of the travel) and the solidifying trailing front. Figure 2.4 shows a schematic of the compositional and structural changes that take place in the melting forefront and their associated deposition zone temperature increases. Hence, one material point may experience multiple temperature excursions and thus exhibit different structural changes such as phase changes, recrystallization, grain growth, segregation, creep, and finally stress relief (*c.f.,* El Kadiri *et al.* (2008)).
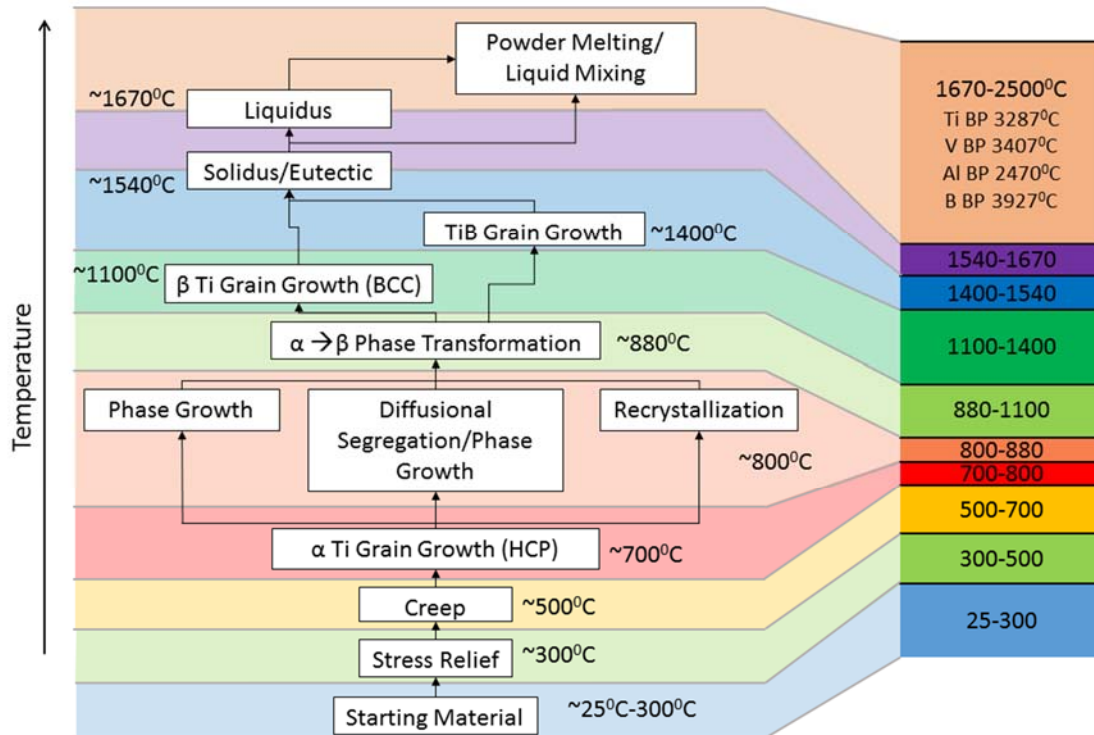
Figure 2.4   The different thermal "events" that change in the titanium functionally graded material as the temperature increases in the direction of the melting forefront.

Note that multiple multiscale structures can arise during the complex temperature history.

Figure 2.5 shows a schematic of the structural changes that take place in the solidifying trailing front as the deposition zone temperature decreases. Different macroscale and microscale structures arise associated with the different temperature levels that a material point will experience during the LENS process. Solid powders are first placed within the laser's heat in order for melting along with the additional heat coming later after more layers stacked upon the point in question, a material point will experience several thermal cycles that first starts with melting. The final product arises from the complex thermal path that is experienced by a material point throughout the total FGM.

21
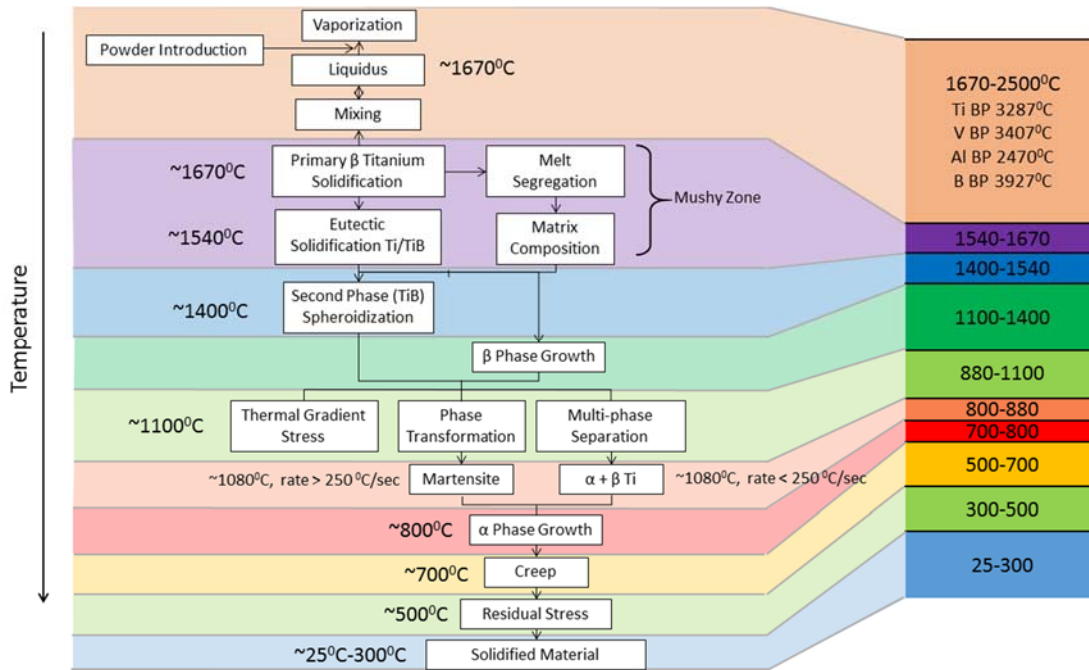
Figure 2.5   The different thermal "events" that change microstructure in the titanium functionally graded material as the temperature decreases in the direction of the solidifying trailing front.

Note that multiple multiscale structures can arise during the complex temperature history.

2.4   Results

2.4.1   Process-Structure Relationships at the Macroscale

The first goal of process control for blown powder methods such as the LENS process is to achieve full consolidation, to maximize density, and to minimize the process related porosity. Porosity, in the LENS process has two major forms: gas bubbles present in the melt pools during solidification typically spherical in shape and deposition related lack of fusion defects that are typically irregular in shape but flattened in the direction of the deposition plane. Gas bubble defects are introduced to the melt from pre-existing pores trapped in the feed powders, process related vaporization, or gas entrained with blown powder injection into the melt pool. In contrast to vacuum environment methods

22

such as the Electron Beam AM method, the LENS process operates in an Argon

atmosphere at standard pressure. Consequently, once formed, gas bubbles can be

maintained in the melt pool during convection and even through solidification.

Deposition related lack of fusion defects can arise from poor spacing between adjacent

hatch fill lines, insufficient laser power available to melt both incoming powder and

substrate, powder overfill where too much powder is added for the selected laser power,

and the mismatch between the laser spot size and melt pool diameter.
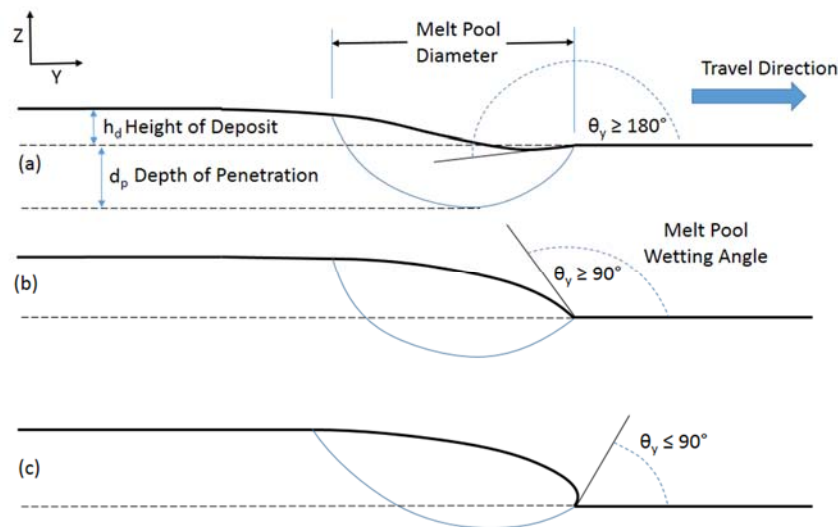
Figure 2.6   A schematic showing three different angles of the leading edge of the
             LENS deposition zone.

Schematic showing three different angles of the leading edge of the LENS deposition
zone: (a) under-filling inducing the greatest depth of penetration, (b) acceptable filling,
and (c) overfilling inducing the least depth of penetration and also admits the lack of
fusion defects.

Figure 2.6 illustrates the three different angles that can arise from the leading edge

of the deposition zone. Critical to porosity here is when the angle is greater than 90

degrees as shown in Figure 2.6. This angle greater than 90 degrees can arise when

overfilling of the powder occurs with respect to the travel speed of the pass as it is laid down. As Figure 2.6 illustrates, what one really desires is to have an under-filling or acceptable filling powder rate combined with the appropriate travel speed in order to garner the greater depth of penetration.

(a)

(b) Pass #1

A — Base Material — A'
h_d Height of Deposit A'
d_p Depth of Penetration

Deposition Path for One Layer that Contains Several Passes

A — A'

(c) Pass #2

A — A'

(d) Base Material

Hatch Spacing   Pass #3

A — A'

Y
X
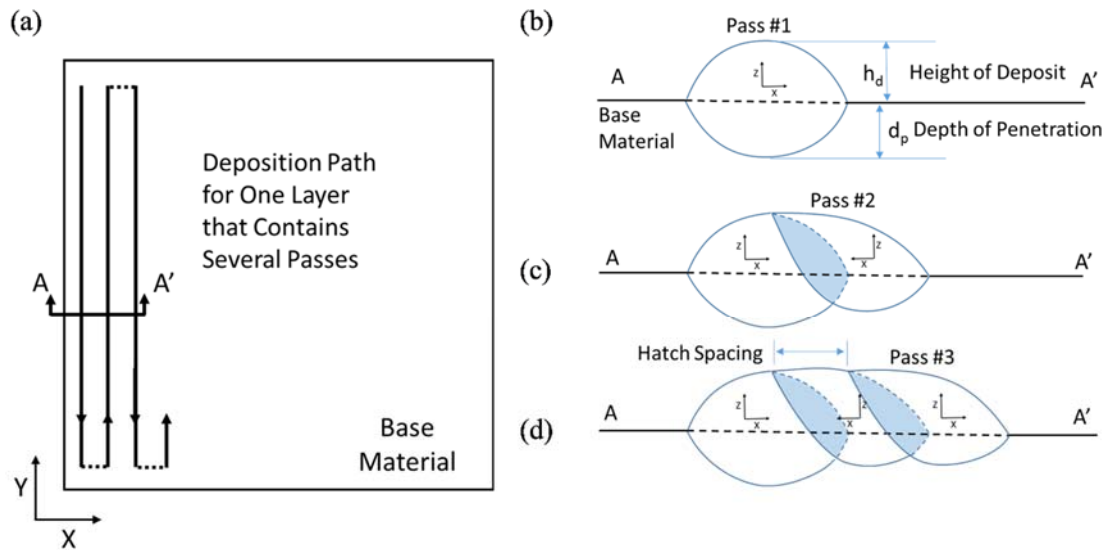
Figure 2.7   Deposition path for a linear hatch fill pattern of the LENS process.

(a) Deposition path for a linear hatch fill pattern of the LENS process. (b) The first pass with acceptable penetration and fill. (c) A second pass showing an acceptable hatch remelted region with an appropriate depth of penetration. (d) A third pass showing an acceptable hatch remelted region with an appropriate penetration and fill.

Figure 2.7 shows in the hatch pattern cross section A-A' that when several deposition passes are laid down appropriately you will achieve a good depth of penetration and when the second pass comes through, there will be no pores. Note also the blue region in Figure 2.7, illustrating the depth of melt penetration into an adjacent pass within the current deposition layer and the overpass of material and thermal history as the material

24

is laid down. Figure 2.8 compares one pass and multiple pass cases when no pores will arise from a good process and when pores will arise from a less effective process. Note the lack of depth of penetration in the cases for the pores, and the greater depth of penetration for the case of no pores. Figure 2.8e,j also show Scanning Electron Microscope (SEM) pictures of the material showing the difference between the two cases when pores are present and when pores are not present.
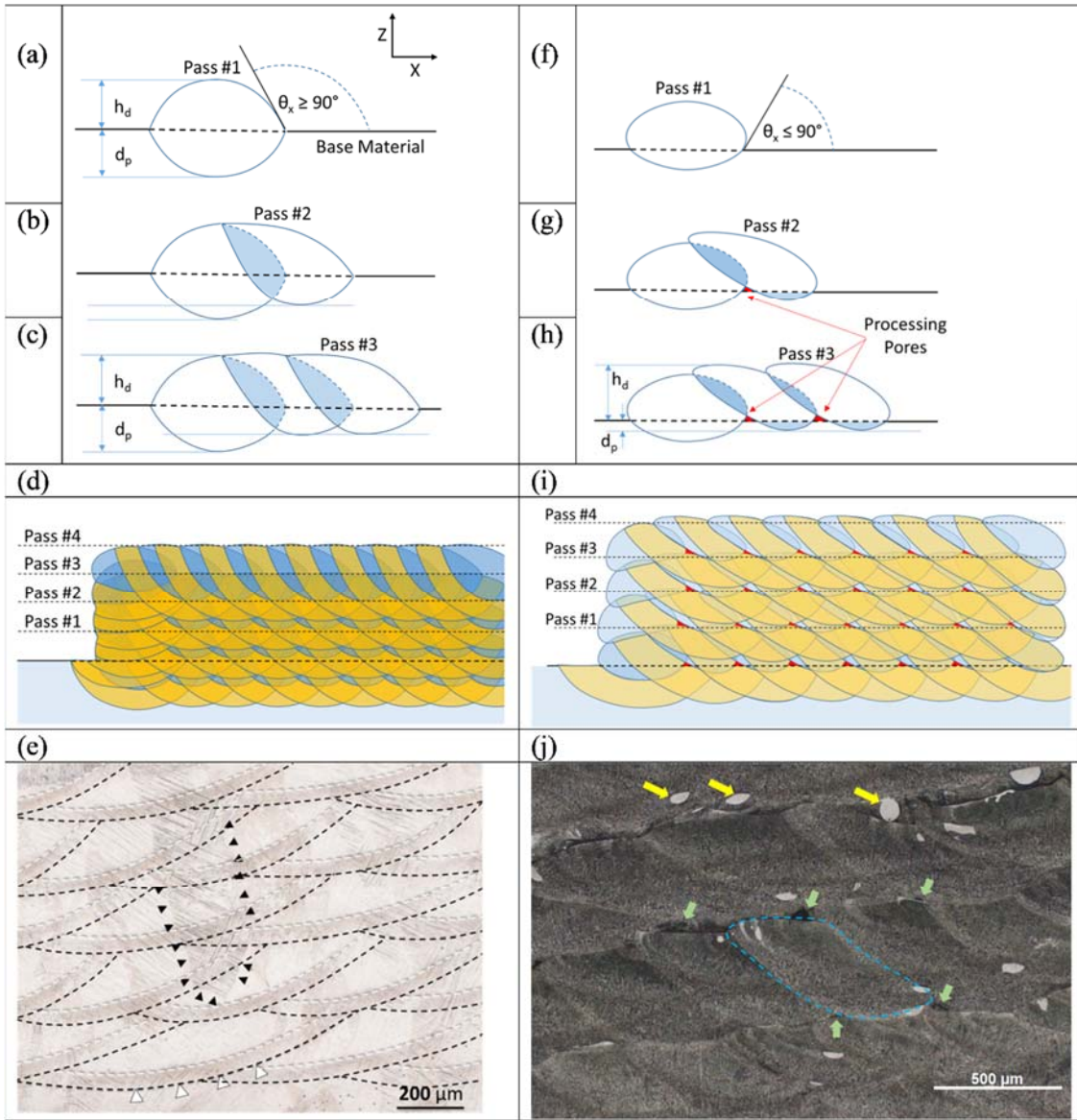
Figure 2.8   Schematic of the single deposition layer sequence of passes for an acceptable LENS process and an unacceptable LENS process.

Schematic of the single deposition layer sequence of passes (a)-(c) an acceptable LENS process and (f)-(h) an unacceptable LENS process. (a) First deposition pass with acceptable penetration and fill where melt pool contact angle ($\theta_x > 90°$). (b) A second pass showing an acceptable hatch remelted region with an appropriate depth of penetration. (c) A third pass showing an acceptable hatch remelted region with an appropriate penetration and fill. (d) Schematic of a successful deposition of four deposition layers with no process porosity. (e) Bright field optical micrograph showing successful deposition. Black arrows indicate a single prior titanium β grain boundary

passing through several deposition layers. White and black dashed lines indicate extent of the heat affected zone. (f) The first pass with unacceptable penetration and fill with melt pool contact angle ($\theta_x < 90°$).   Note that (f) shows a lack of penetration and overfill producing a leading edge overhang. (g) A second pass that allows a pore to nucleate due to lack of penetration, (h) A third pass showing an accumulation of lack of fusion that induces processing pores. (i) A schematic showing the distribution of pores caused by lack of penetration for 4 deposition layers. (j) A Bright field optical micrograph showing 4 layers of actual LENS deposition displaying pore distribution caused by lack of penetration. The yellow arrows point to unmelted Ti-6Al-4V powder; the green arrows point to processing pores; and the blue dashed line represents a single deposition pass.

Since the porosity will arise mainly when the depth of penetration is too shallow, it is worth determining the cause-effect relationships for creating a certain depth of penetration. Bright field optical micrographs after etching the surface with Krolls agent reveal the perimeter of the heat affected zone (indicated by white and black dashed lines in Figure 2.8e) and the boundary of the melt pool (indicated by the blue dashed line in Figure 2.8j). From the spacing between either the melt pool bottom or the HAZ bottom of successive layers, the height of each deposited layer was determined. Figure 2.9 shows the actual deposition process features for each deposition pass in the eight layer FGM. Figure 2.9a shows the deposit height derived from measuring the distance either between successive HAZ patterns or the melt pool boundary. Figure 2.9b shows the depth of the heat affected zone (HAZ) as measured from the melt pool boundary. Recall that in the LENS blown powder AM method, each deposited surface was not truly level and that each deposition pass was a different thickness depending on the *in situ* process conditions as shown in Figure 2.9a. Consequently, the errors in deposition height accumulated during the build as shown in Figure 2.9c. Error here refers to the difference between the actual total build height and the planned build height. The distribution signifies that the control loop is trying to adjust the previous laid powders.
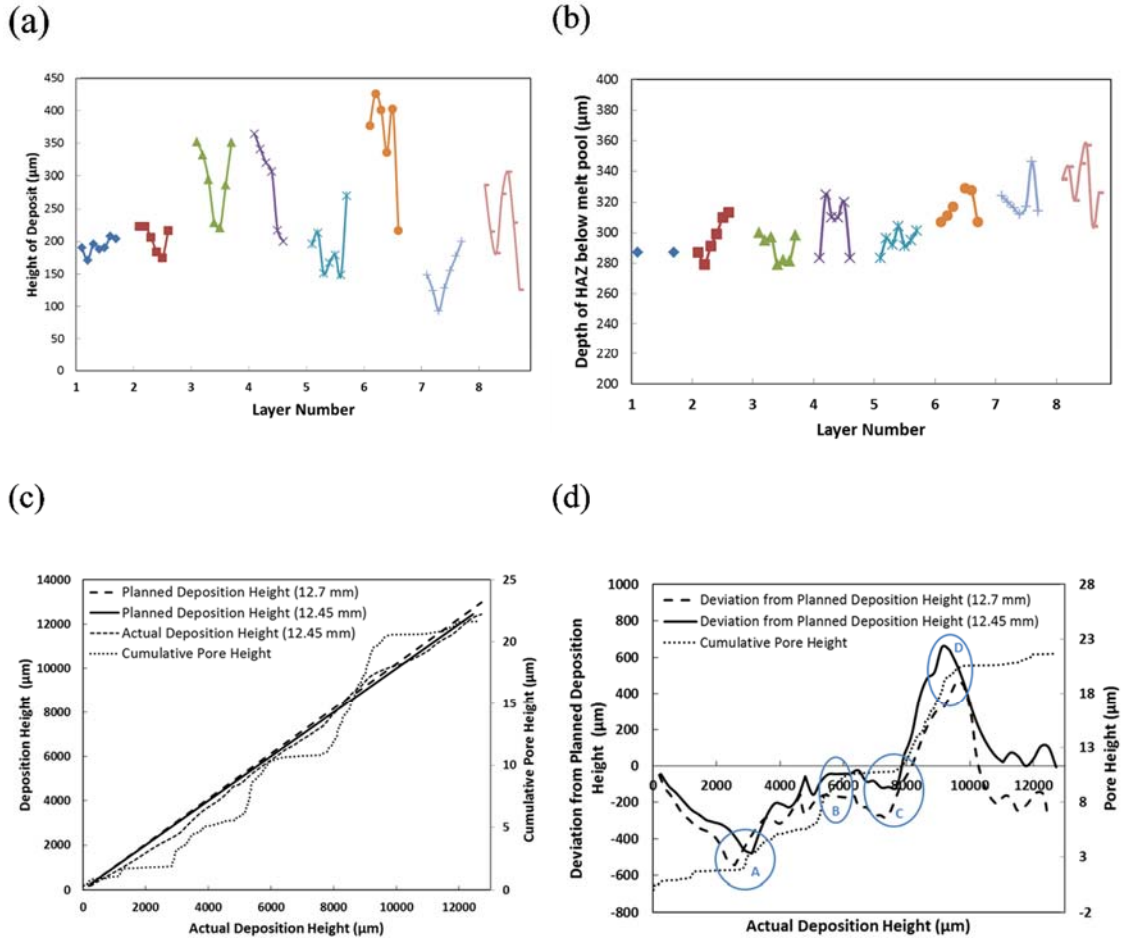
Figure 2.9   Four plots showing height of deposit and depth of heat affected zone for each deposition pass in eight layers and deviation of actual deposition height from planned deposition height.

For each deposition layer pass in the 8 layer FGM, (a) the height of deposition pass as measured by HAZ to HAZ and melt pool bottom to melt pool bottom between successive deposition passes. (b) The depth of the heat affected zone (HAZ) as measured from the bottom of the melt pool. (c) Planned deposition height versus actual deposition height (d) Error accumulates between the planned and actual deposition height.

Note in Figure 2.9a that the deposition height ranged from 100 microns to almost

450 microns. These variations can lead to overfilling and thus lead to the porosity. A

study of process defects collected using x-ray computed tomography (CT) correlated

28

defect location, size, and shape to the deposition process features shown in Figure 2.9. Because the hatch spacing, powder mass flow rate and laser power remain constant, the height of deposit will correlate to the depth of penetration. The depth of penetration (d_p) cannot be measured directly in a multilayer deposit since the original reference surface is remelted so an ambiguity arises for d_p. Therefore the height of deposit (h_d) was chosen to capture the trend for the depth of penetration. Figure 2.9d shows two different plots based on assumptions of what was the planned deposition height, which was not originally given to the processing design. The measured final height was 12.45 mm, but if that was planned, the deviation is shown in Figure 2.9d. Alternatively, the original planned height was 12.7 mm, so the deviation was also plotted with that assumption in Figure 2.9d. As such, we do not really know what was the planned height nor how the control loop made decisions in the LENS processing, but clearly when we compare both data to when the cumulative pore height increased, there were four specific alterations during the build process. Points A, B, C, and D indicate the control loop *in situ* modifications because of the porosity level. Hence, the deposition height affected the porosity and the porosity affected the laying down of the next layer particle volume.

Figure 10 organizes the process defects according to the height of deposit for the layer where the defect occurred. Note in Figure 2.10 that the number density and volume increased with a lot of scatter as the laying continued, but the clear message is the total process pore volume increased as the height of deposit increased. Some parts of the processing identify some variations as denoted in Figure 2.10d. Note the xray tomography data shown in Figure 10c. All of the data reduction shown in Figure 2.10

29

was garnered from correlating the xray data in Figure 2.10c with optical microscopy derived deposition features from Figure 2.9.
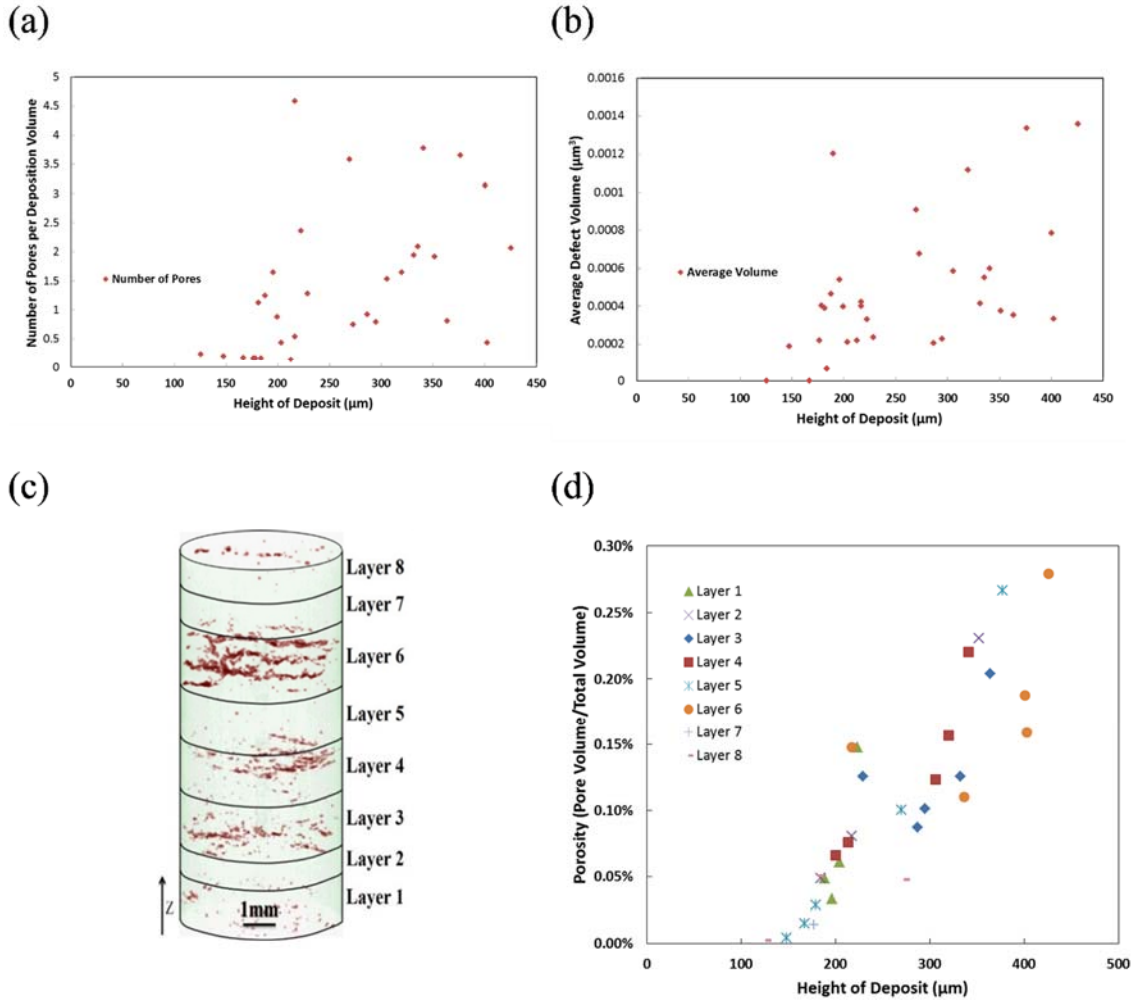
Figure 2.10   Process defects detected through x-ray computed tomography (CT).

At fixed hatch spacing, the effect of height of deposit (hd) is shown versus (a) Number of pores per deposition volume, (b) Average defect volume, (c) total process pore volume per pass for each layer. (e) Porosity per pass for each layer. (c) An x-ray CT volume rendering showing process pore distribution (colored red) through volume of a cylinder spanning all 8 layers.

Figure 2.11 shows a local pore from an optical image illustrating the distribution of porosity near unmelted regions which then in turn incurs a low depth of penetration. Note when comparing the pore in Figure 2.11 that the image matches the geometrical structures shown in the schematics of Figure 2.8. Hence, the pore shown in Figure 2.11 arose from the second pore type mentioned earlier that is deposition related that are irregular from the lack of fusion.
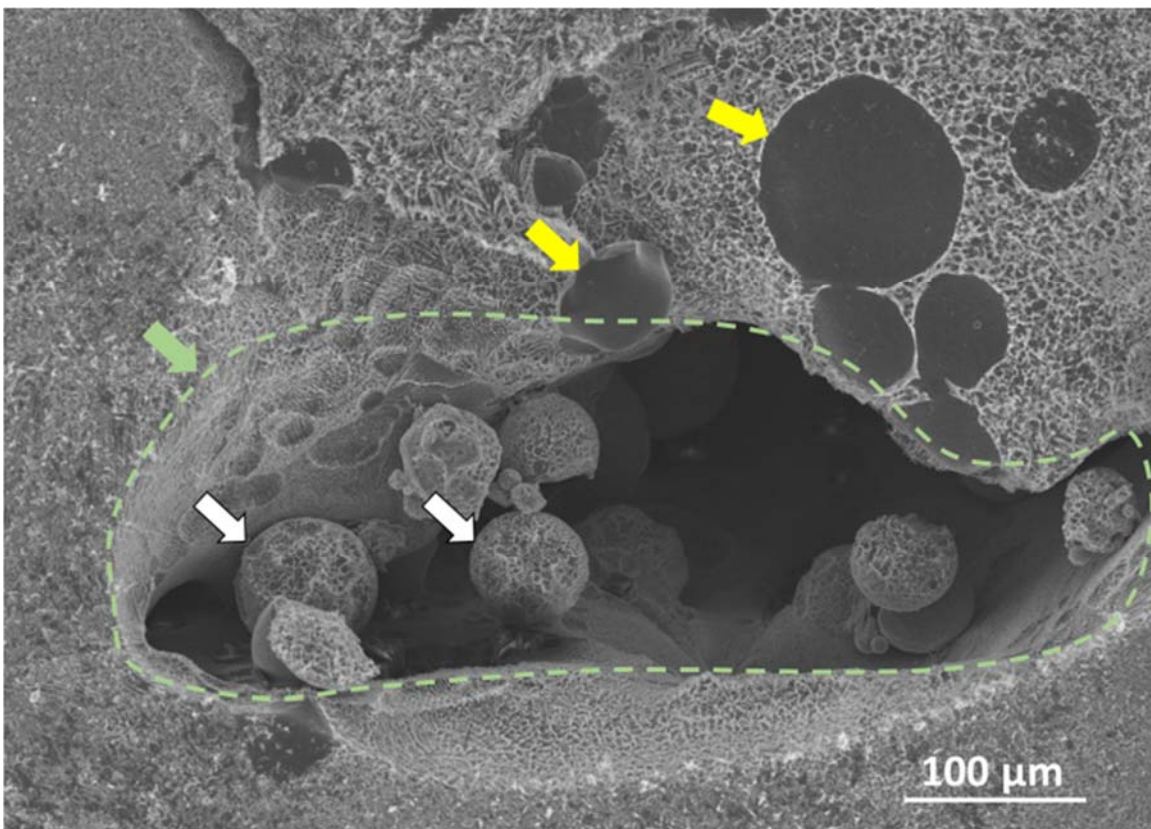
Figure 2.11   A processing defect shown in a Scanning Electron Microscope (SEM) image of a region in Layer 6.

The yellow arrows point to unmelted Ti-6Al-4V powder; the white arrows point to unmelted Ti-1B powders; the green arrow and the green dashed line outlines a single process pore corresponding to green arrows in Figure 8j.

2.4.2   Process-Structure Relationships at the Microscale

Because different material points will experience different thermal histories throughout the LENS building process, it is important to understand the convolution of the complex thermal history with the complicated microstructural morphologies.   For example, Figure 2.12 shows simply one preheat pass in which the base material will incur a melt and HAZ. Once the first deposit is laid down, a powder will melt on top of the base material. When the next pass is laid down and melted, it affects the previous melted powder in a complex manner. Note in Figure 2.12 that there will exist four different microstructures (melt, HAZ, Melt + HAZ, and HAZ +HAZ), because of the four different thermal histories experienced in the case of just two passes.
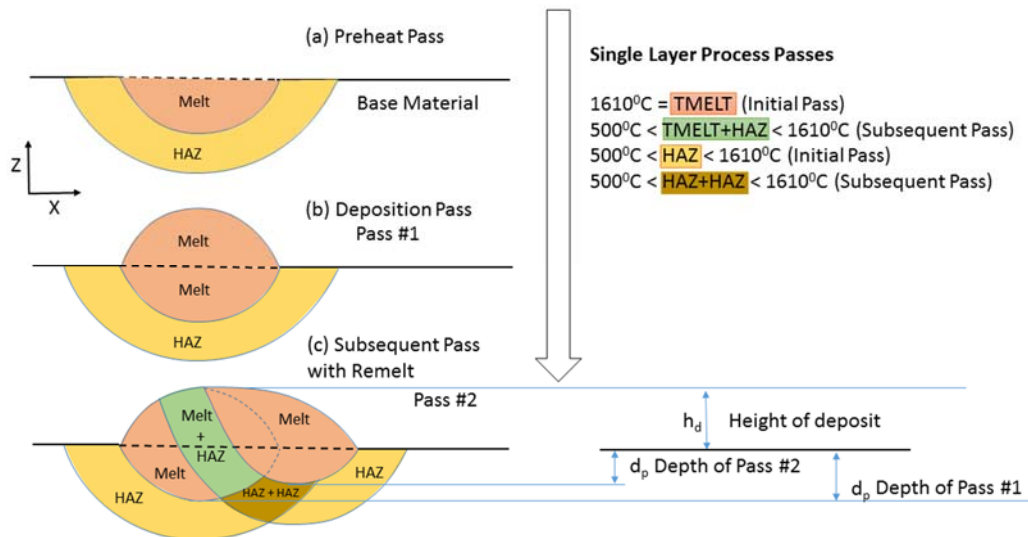
Figure 2.12   A schematic diagram showing a preheating pass, a single deposition pass, and a subsequent deposition pass.

For acceptable passes, this schematic shows (a) a preheating pass, (b) a single deposition pass and (c) a subsequent pass illustrating the melt zone, heat affected zone (HAZ), and base material. Note that the depth of a particular pass can vary. We also show here that in just two passes we have a potential for four unique temperature-history dependent microstructures all with the same original chemistry.

The processing also causes microscale features due to the thermal cycling acting as different heat treatments once the original material was laid down. Figure 2.13a shows Point A, which was laid down in the first pass but experienced heating from four different passes. The temperature excursion that Point A experienced is shown in Figure 2.13b noting that each layer incurred four passes.
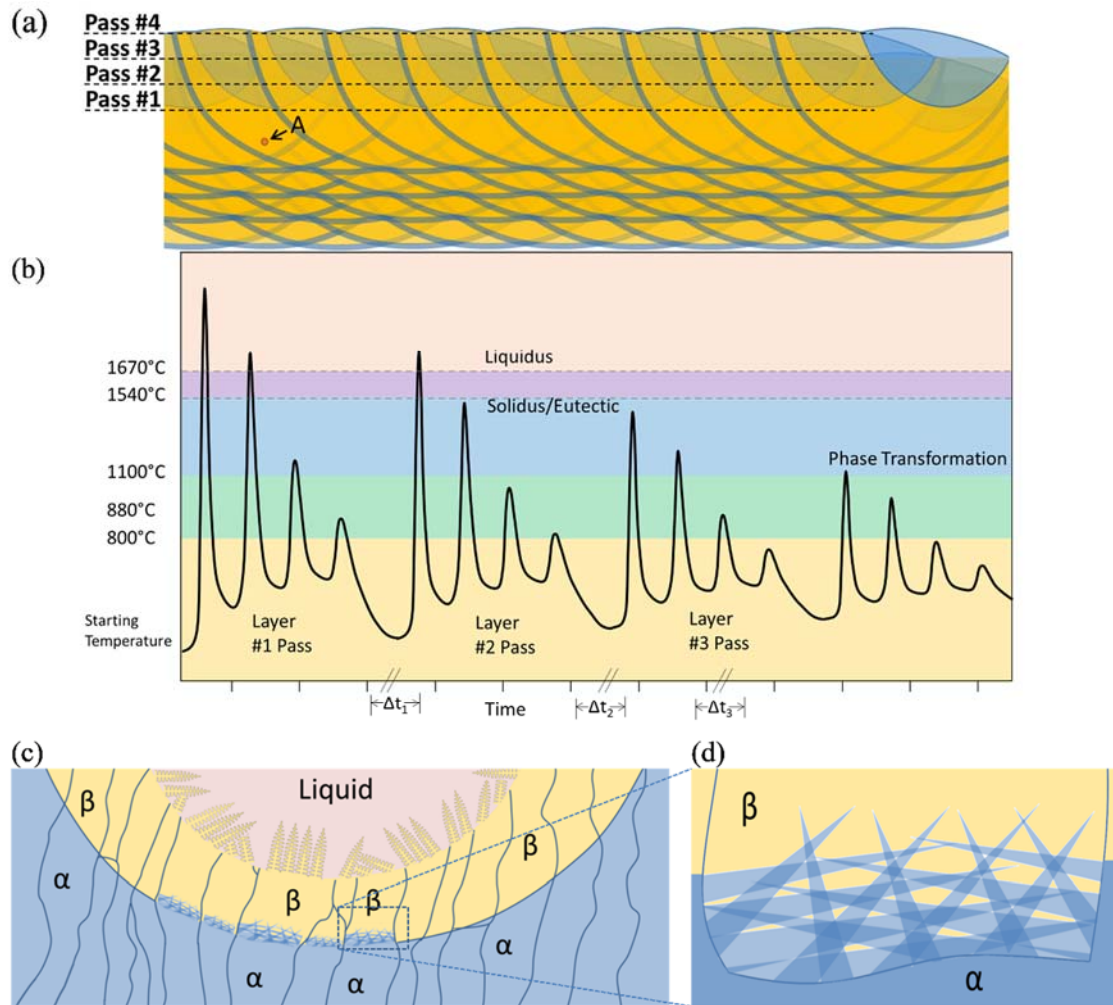
Figure 2.13   Schematic diagrams showing the thermal history and phase changes of a material point undergoing multiple thermal cycles as a result multiple deposition passes in a single layer and multiple deposition layers.

Material point A (a) deposited in layer Pass 1 is exposed to thermal cycling in the LENS process during the deposition of Layers 2 through 4. Material point A undergoes multiple excursions (b) through the phase transformation zone for titanium alloys. (c) A schematic of the events: liquid to solid β, solid β to solid α. (d) A schematic of acicular morphology of α transformed at high cooling rates.

Overall Point A experienced sixteen thermal cycles at different temperatures. The material at Point A experienced melting and solidification three times, was in the mushy zone once, passed eight times from above β transus temperature, passed twelve times through the phase transformation zone, and returned five times to the α + β stability zone. The final microstructure at Point A will retain history dependent features and an associated morphology. The solidification front structure in Figure 13c depends on the cooling rate giving rise to a particular dendrite cell size spacing, grain size, and eutectic morphology. After solidification, the liquid to solid β phase titanium then turned to solid phase α titanium. Figure 2.13d shows the acicular morphology of the α phase titanium that transformed from the β phase titanium. The heating and cooling rates are so high for laser induced heating, this acicular morphology arises for the α phase titanium (Ahmed and Rack 1998). The complexity of microstructure only increases when all of the passes and layers are added.

The microstructure will further be different throughout the different layers, because of the cyclic nature of the solidification and phase transformation events throughout the build height. Figure 2.14 illustrates how the phase area fraction changes during solidification and solid state phase transformation. Recall that as the layering increases from the first to the eighth layer, the boron amount increases from 0% to 1%. For Layer 1 shown in Figure 2.14a where no boron is present, the solidification

34

temperature range is narrow approximately at 1700 °C, and the α + β phase transformation range spans from approximately 1100°C to 850°C. For Layer 4 at 0.4% boron composition, the solidification range covers a wider temperature range from approximately 1700°C to 1540°C, because of the eutectic reaction of boron with titanium forming Borlite.
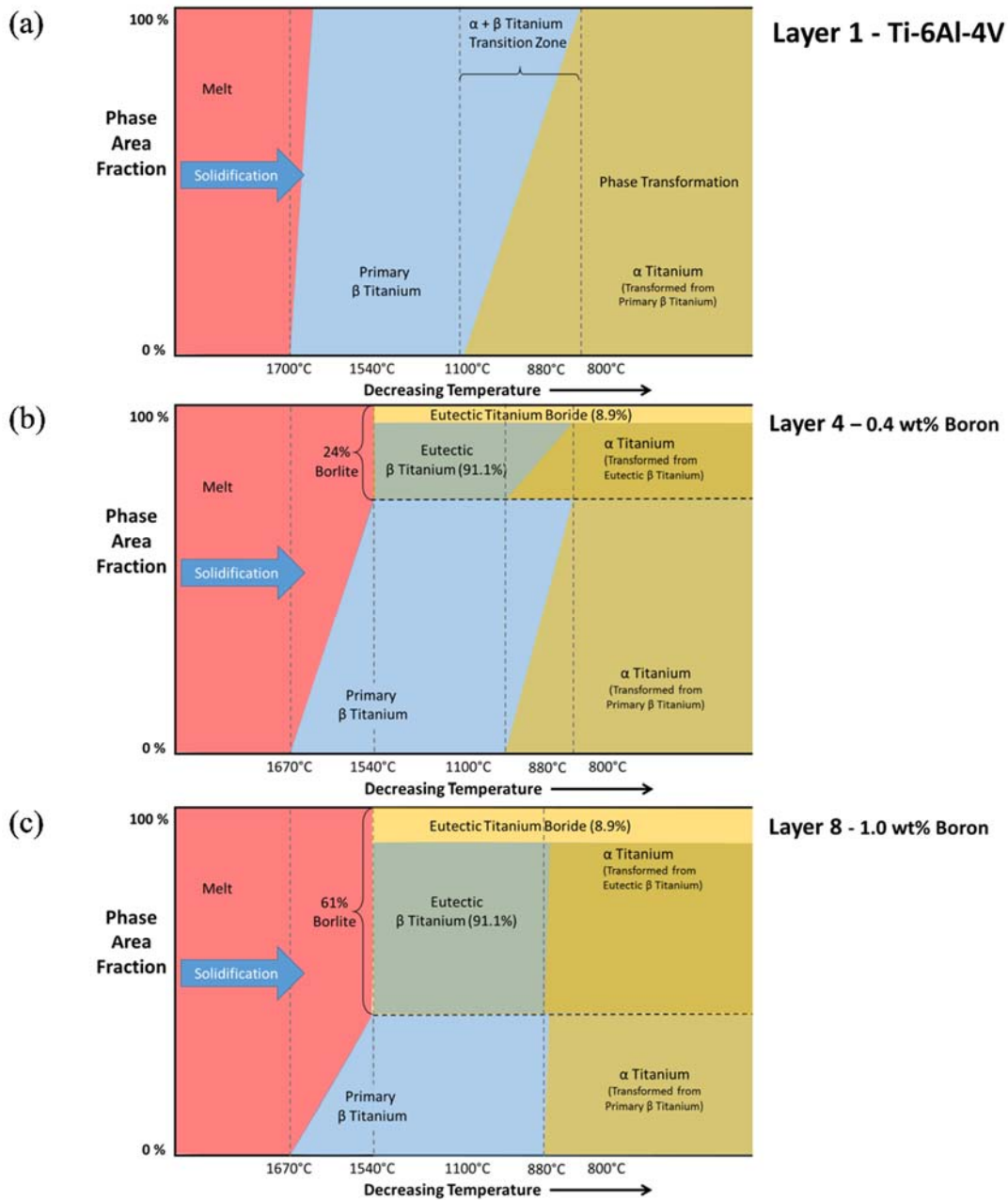
Figure 2.14   A schematic showing phase area fraction expressed as a function of
            decreasing temperature through solidification and phase transformation for
            three different layer compositions.

Phase area fraction expressed as a function of decreasing temperature through
solidification and phase transformation for (a) Layer 1Ti-6Al-4V, (b) Layer 4 - 0.4 wt%
Boron, and (c) Layer 8 - 1.0 wt% Boron.

36
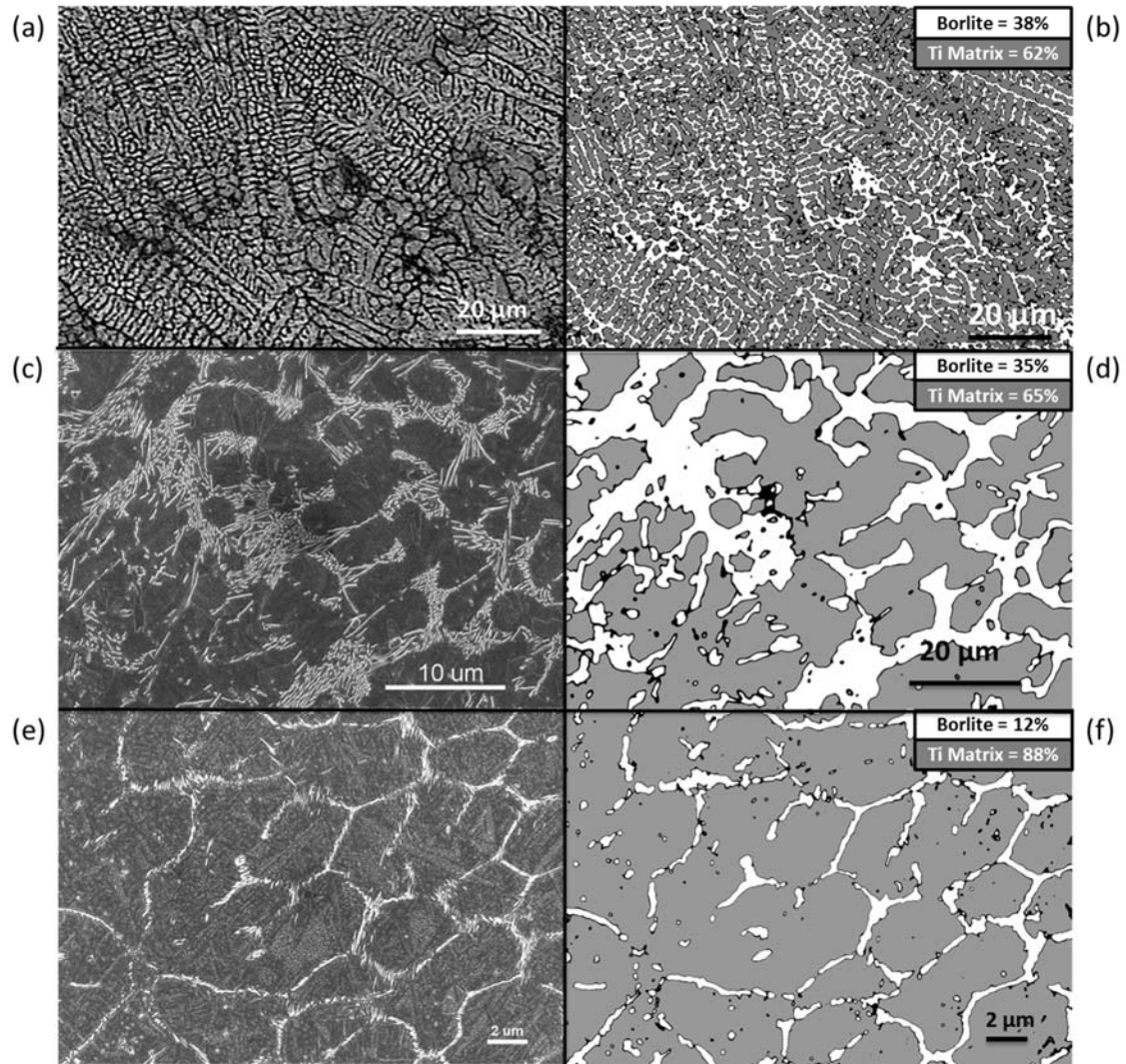
Figure 2.15   Optical and scanning electron micrographs showing three different Borlite morphologies and their associated phase maps.

Optical (a) and scanning electron micrographs (c, e) of regions containing Borlite, the eutectic solidification structure of 1.6 weight percent boron. (b, d, f) Phase maps where gray represents the titanium matrix and white represents the Borlite region. Borlite contains 8.9% titanium boride and 91.1% titanium.

The final area fraction of Borlite is 24% of which 8.9% is eutectic TiB and 91.1% is eutectic titanium. Note the reduction in aluminum and vanadium has narrowed with respect to the $\alpha + \beta$ transition zone for both the primary and eutectic titanium. For Layer 8 with 1.0% boron composition, the solidification temperature range remains wide but the

37

liquidus temperature reduces to 1670°C while the solidus remains at 1540°C. The final

area fraction of Borlite is 61% and the dual solid state phase transition zone has narrowed

to 882°C. In summary, Figure 2.14 illustrates the expected phase area fractions correlated

to the composition, chemistry, and morphology.
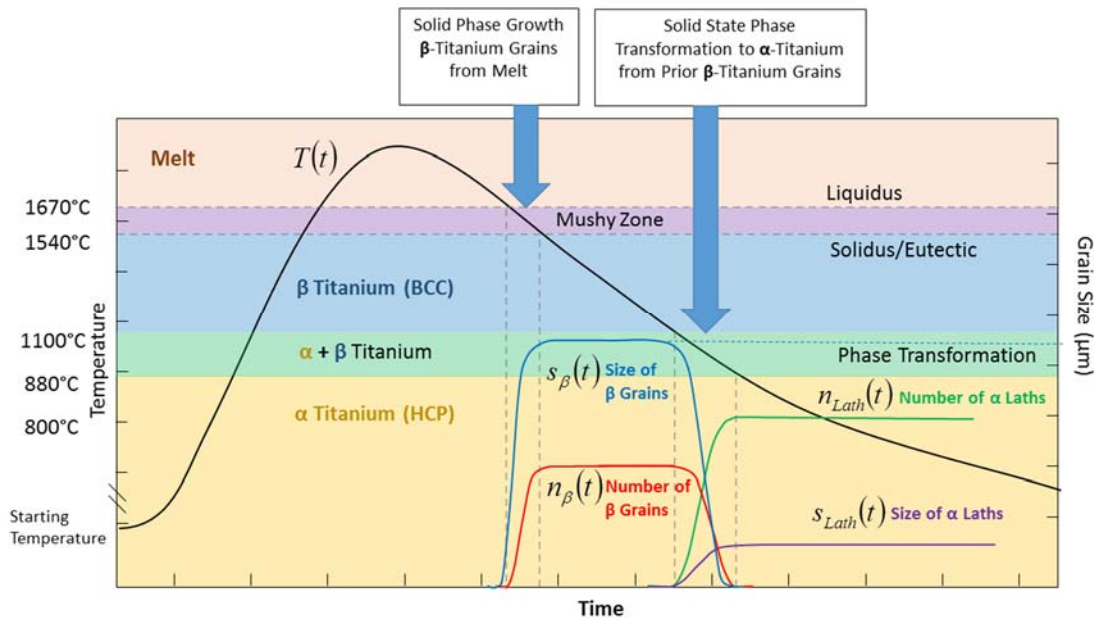
Figure 2.16   Temperature-time history for single pass showing grain size and number
               and alpha lath size and number.

The stereology of the microstructural features generated in a single temperature

passage through the phase transition zones (shown in Figure 2.14) are dependent on the

cooling rate. In Figure 2.16, the black line shows the temperature profile of a point

increasing into the melt zone and then decreasing through solidification and phase

transformation. Figure 2.16 illustrates how the number density (η_β) and size (s_β) of the β

titanium grains increase; later, the η_β and s_β decrease as the number density (η_{Lath}) and

38

size (s_{Lath}) of α laths increase consuming the β grains. For a given volume fraction of β titanium grains, the number and size will be determined by the cooling rate.

2.4.3   Chemistry-Structure Relationship at the Microscale

Sen *et al*. (2007) studied the influence of small additions of boron on the primary solidification of Ti-6Al-4V by casting via the skull melting process. They showed a grain refining effect for boron additions up to 0.1 weight percent composition. Figure 2.16c shows the β titanium (BCC) grain size with respect to boron concentration comparing the casting process of Sen *et al.* (2007) to our work with the LENS. Note that the trends are very similar although the heating and cooling rates are different from a skull melting casting versus a laser based approach like LENS.
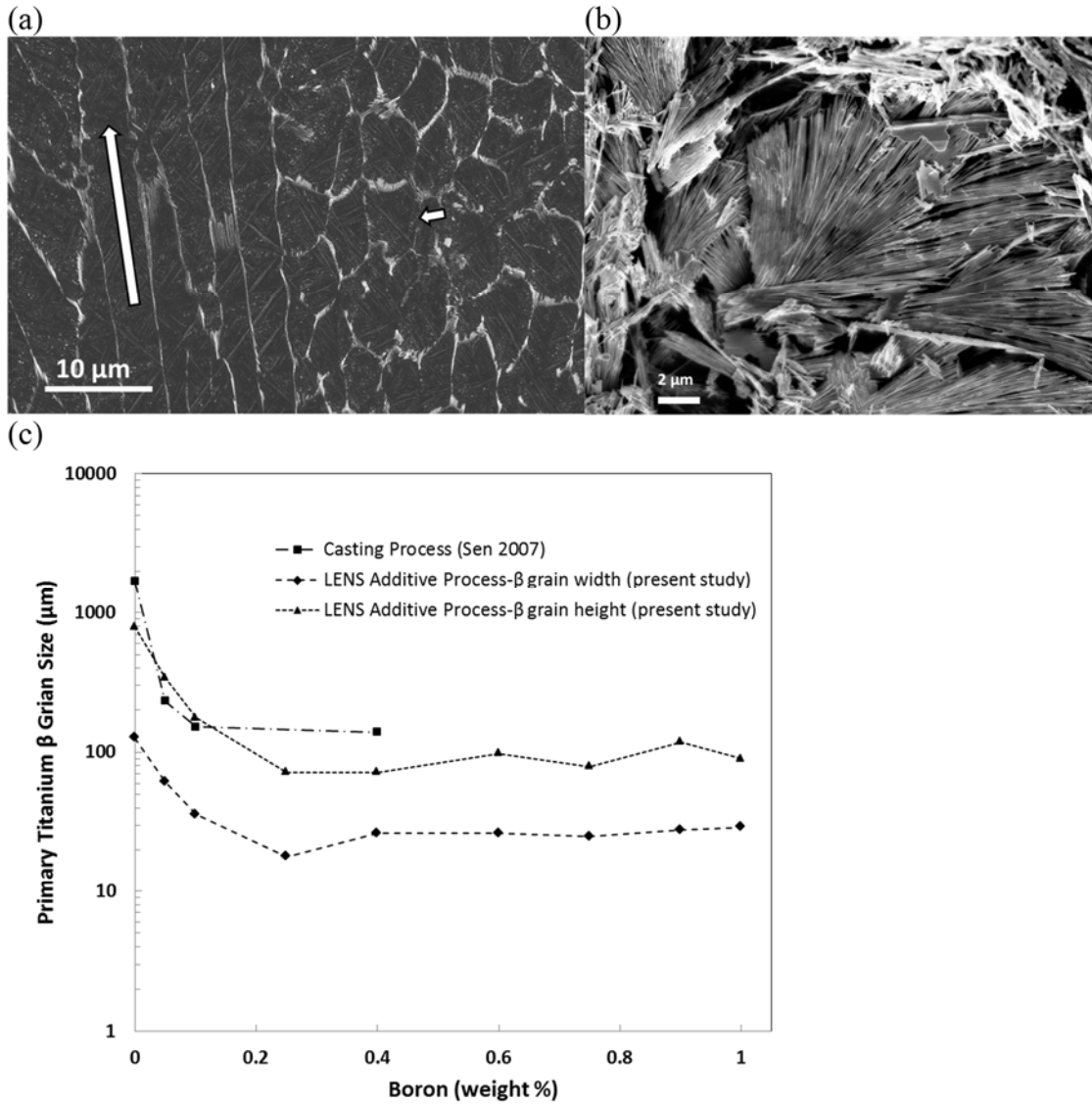
Figure 2.17   Primary titanium β grain size as a function of boron composition
               comparing additive manufacturing (LENS) results from the present study to
               that of casting (skull melt process) (Sen et al. 2007)

Scanning Electron Micrograph (SEM) of titanium boride eutectic regions <0.1% boron.
(a) Long white arrow indicating adjacent primary titanium dendrite arms decorated by
eutectic TiB. Short white arrow show transverse section of adjacent dendrite arms
enlarged in (b) after deeply etch to remove titanium matrix. TiB whiskers are shown
following primary dendrite arm cells. (c) Primary titanium β grain size as a function of
boron composition comparing additive manufacturing (LENS) results from the present
study to that of casting (skull melt process) (Sen et al. 2007).

2.5 Discussion

2.5.1 Initial Titanium Beta Grain Size

The multiscale structure of importance is the β titanium grain size. Figure 2.16 shows SEM pictures of the TiB in the eutectic region of Layer 2 when the boron was less than 0.1%. Solidification of the melt pool in the LENS process is predominantly directional, dendritic, and epitaxial, inheriting the grain orientation of the seed grains at the solid-liquid interface as illustrated in Figure 2.16a. The primary features to emerge during solidification are the β titanium (BCC) grains. These are the first to solidify from the melt. The number of β grains that result when the melt pool solidifies is correlated to the number of seed grains in the solid decorating the solid liquid interface. Figure 2.16b shows the acicular needles that arise because of the rapid cooling rate. For the first layer deposited on a mill annealed commercially pure base plate (average grain size ~46 μm) and a melt pool diameter of 780 μm, there are approximately 40 grains spanning the solid-liquid interface of a two dimensional slice of the melt pool. However, the β grain size increased in the solid material near the melt pool interface due to heating induced grain growth thereby increasing the seed grain size as shown in Figure 2.16c. The dendritic growth is solidification rate dependent. The spacing of the primary dendrite arms is proportional to the solidification rate (Sato 1982) Where the seed grain size is larger than the primary dendrite arm spacing, multiple dendrites nucleate from the same parent grain surface (in the case of a smooth solid/liquid melt interface) or are retained (in the case of re-melting that follows previous dendritic structures). In the absence of chemical content to cause melt segregation, dendritic growth of the solid phase consumes the liquid phase until adjacent dendrites merge, leaving little trace of secondary dendrite

41

arms. The solidification direction follows the temperature gradient in the melt pool. While the solidification direction at the bottom of a stationary LENS melt pool is directed upward, the solidification direction of a translating melt pool is horizontal at the melt pool surface sides and trailing edge, such that total solidification orientation is a mixture of vertical and horizontal directions. However, because the melt pool from the deposition of a new layer penetrates the previously deposited surface, a portion of the horizontal dendrite orientation is lost to re-melting. The degree to which horizontal solidification features are eliminated, depend on the depth of penetration of the new layer melt pool. Consequently, the structure that emerges from the LENS process often resembles columnar grains in casting. In titanium, the primary solidification phase is body centered cubic whose preferred solidification orientation is the [100] direction. Pure titanium is an allotropic metal with a body centered cubic structure stable at temperatures below melting (~1670 °C) and above 882 °C and hexagonal close packed structure stable below the phase transformation temperature of 882 °C. Therefore although a [100] texture is established in the direction of solidification, the resulting texture is dependent on the transient transformation behavior of the specific titanium alloy employed.

It can be assumed that the melt pool has a homogeneous composition when feed powders are of similar composition. However, making use of a dual powder feeder to achieve *in situ* mixing may result in compositional gradients in the melt pool.

2.5.2 Borlite Titanium/TiB Eutectic Region

In this study, all layer compositions are hypoeutectic with respect to boron with the highest concentration being approximately one weight percent. Boron forms a eutectic reaction with titanium at a composition of approximately 1.64 weight percent

and a temperature of 1540° C. Figure 2.14b shows the sequence phase volume change during solidification of Layer 4 with 0.4 weight percent boron. Under near equilibrium conditions, the BCC titanium solid phase grew until it reached 76 percent volume. At that point, solidification followed the eutectic reaction and the remaining 24 percent liquid formed a solid phase that we will call Borlite. Borlite is a eutectic structure containing ~8.9% orthorhombic titanium monoboride (TiB) by volume and ~91.1% Titanium. Figure 2.15 shows the morphology of the Borlite regions with 12% Borlite (Figure 2.15e, f) and 35% Borlite (Figure 2.15c, d) phase volume fraction.   The morphology of the TiB in the Borlite varies from needle-like whiskers at high solidification rates to plate-like sheaves at lower rates. The term Borlite is inspired by the term Pearlite used to describe a eutectoid structure in carbon steels. The phase volume ratio of cementite to ferrite remains constant, but the morphology of the cementite can vary sufficiently to be observed in optical microscopy, causing observers to identify one optically distinct form as Pearlite and another as upper and lower Bainite.

The presence of boron in the melt influences the solidification structure of titanium. At low concentrations (~0.1 weight percent), boron remains in the liquid phase as titanium dendrites grow and thicken. The space between the secondary dendrite arms is filled with primary titanium. By the time that boron has been enriched in solution sufficient to reach the eutectic composition, the primary titanium dendrites reached a columnar form. When the eutectic solidification initiates, it occurs in the liquid volume space between the primary dendrite arms of the primary titanium phase.

As the starting concentration of boron increases, the eutectic solidification initiates earlier in the primary dendrite solidification sequence. The Borlite region

occupies more space between adjacent primary dendrite arms as illustrated in Figure 2.16a. Layer 2 and 3 with concentrations of 0.1 and 0.2 weight percent show this structure.

At some point the starting concentration of boron is sufficient to interrupt the primary titanium dendrite growth at the early stage of secondary dendrite arm formation. The melt concentration of boron reaches the eutectic composition before space between the secondary dendrite arms can be filled with primary titanium. The remaining space is filled with Borlite extending out to the interdendritic space. This is observed in sparse locations starting in Layer 3 with 0.2 weight percent boron, increases in Layer 4 and 5, and becomes dominant in Layers 6, 7 and 8. The variation is attributed to the difference in cooling rate through the melt pool that will in turn have an effect on the primary and secondary dendrite spaces. Figure 17b shows the average primary and secondary dendrite arm spacing with respect to change in boron composition.

Grain refinement is observed with the smallest boron addition occurring in Layer 1 at 0.1 weight percent. The size of the β titanium grain perpendicular to the growth direction decreases. The effect that boron seems to have is to segregate primary dendrite cores at the solid/liquid interface. This segregation seems to permit competition between dendrite cores and prevents domination of larger grains in the melt pool. Without boron additions, the primary β titanium grains propagate through successive deposition layers. With 0.1 weight percent boron, primary β titanium grains can still propagate through successive deposition layers, but the dimension of the β grain in the deposition plane decreases. Where Layer 1 has 7.5 grains across the melt pool, Layer 2 has 26 grains. They are still primarily oriented normal to the deposition surface imparting an initial

44

[110] texture. Figure 16c shows the reduction in primary titanium β grain size with respect to changes in boron concentration for LENS deposited material and casting as reported by Sen *et al.* (2007) who used the skull melting process.
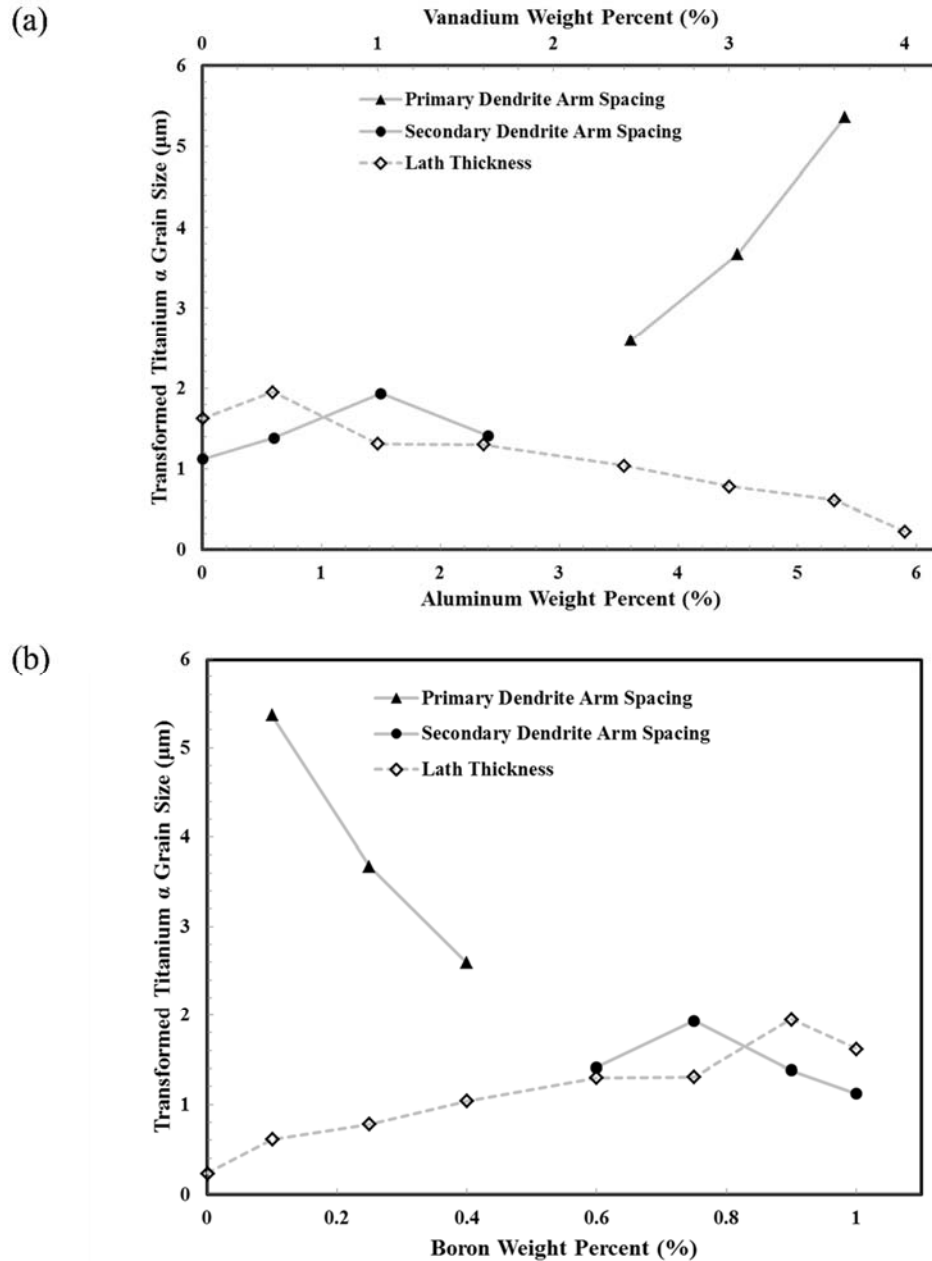
Figure 2.18   A chart showing transformed titanium α lath thickness, average primary and secondary dendrite arm spacing measured with respect to aluminum, vanadium, and boron composition.

Transformed titanium α lath thickness, average primary and secondary dendrite arm spacing measured with respect to (a) aluminum and vanadium composition by weight percent and (b) boron composition weight percent. When both primary and secondary dendrite arm spacing is observed, the smaller of the two are plotted.

46

2.5.3   Phase Transformations

The third microstructural feature of relevance is the phase sizes after transformation. Figure 2.18a shows the change in transformed titanium α lath thickness with respect to the aluminum and vanadium composition. The α lath thickness values plotted in Figure 2.18b were measured from optical and scanning electron micrographs and represent the average values for each of the 8 composition layers listed in Table 3.2. The final lath thickness decreased from 2 μm to 0.2 μm as vanadium and aluminum concentration increased. The alloy chosen to blend with the boron was Ti-6Al-4V with six percent weight aluminum and four percent weight vanadium. Both elements form in solid solution with titanium. As a binary alloy, aluminum additions to titanium stabilize the HCP phase and increase the phase transformation temperature.   Vanadium naturally forms a BCC structure; consequently as a binary alloy with titanium, vanadium stabilizes the BCC phase and reduces the transformation temperature. When used in combination, aluminum and vanadium produce a heat treatable titanium alloy capable of producing a host of multiple phase microstructures.

Most heat treatments involve soaking the material at a temperature where alloying elements can segregate from the starting β titanium grain size into α and β titanium phases by diffusion, then controlled cooling refines the remaining β titanium phase through transformation to α titanium.   When the Ti-6Al-4V alloy is used in AM processes, the final microstructure is determined by the time and temperature history of cooling through the transformation temperature range. The material can be modified by subsequent heat treatment, but the initial β titanium grain size and texture is locked in by the solidification structure.   In Layer 1, the average β titanium grain diameter was 110

47

μm. For comparison, Ti-6Al-4V mill annealed rolled plate had a grain size of approximately 2-4 μm. Ti-6Al-4V descending through the transformation zone at a high rate (>250 °C/s) undergoes martensitic transformations (so called because it is considered diffusionless). The crystallographic structure is an α HCP titanium. The β titanium grain transforms into a nearly plate-like lath structure of the α HCP titanium in 12 hexagonal variants {110} $_\beta$ // (0002) $_\alpha$,<111> $_\beta$ //<11$\underline{2}$0> $_\alpha$. The thickness of these plates is consistent and can be traced from one prior β grain boundary edge to the other.

Interpreting the distribution and morphology of α titanium plate-like laths from polished optical micrographs is challenging. For bright field imaging, etching is required to provide sufficient contrast to distinguish between α laths; however, only the boundaries are highlighted. Due to the HCP structure of α titanium, polarized light provides a color contrast associated with the crystallographic orientation angle of the individual grain with the surface, highlighting not only grain boundaries, but also grains with similar orientation. Using polarized light, etching is not required. The boundaries between α laths are visible. Parallel laths have similar color which indicates a similar crystallographic orientation (confirmed by EBSD). Adjacent β grains are distinguished by two features: parallel α laths change direction at prior β grain boundaries, and α lath cross section and color varies. A deep etching of the Ti-6Al-4V layers with nitric acid reveals the morphologies of families of α laths. Each lath appears to follow a wedge shaped pattern (shown in Figure 2.19) where similar wedge edges are parallel and grow with a leading edge piercing angle of ~21° (minimum 16° max 30.5°).

48
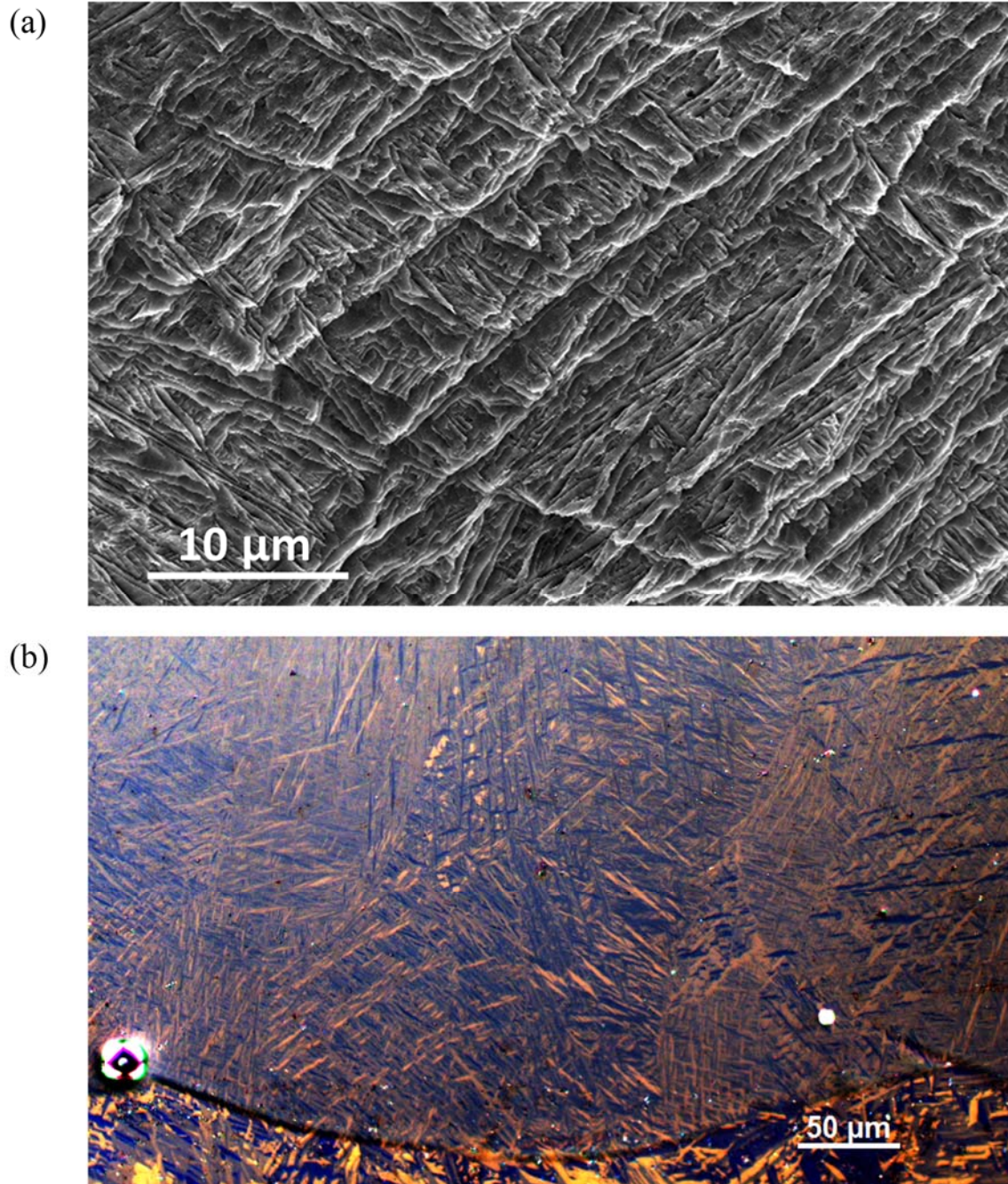
Figure 2.19   A scanning electron microscope image and optical micrograph of LENS
deposited Ti-6Al-4V region showing Transformed titanium α laths forming
of wedge shaped pattern.

A scanning electron microscope image (a) of LENS deposited Ti-6Al-4V region from
Layer 1 after deep etching with nitric acid. Transformed titanium α laths forming of
wedge shaped pattern. (b) A polarized light optical micrograph of Ti-6Al-4V Layer of
similar region.

2.5.4 The Impact of Successive LENS Thermal Cycles Through α + β Titanium Region

Ahmed and Rack (1998) has shown from Jominy quench experiments on Ti-6Al-4V that aluminum and vanadium segregate during the β to α titanium transformation. Although Ahmed and Rack (1998) argued for a rapid massive diffusionless transformation where solute segregation was limited, they did find by qualitative EDX analysis that aluminum in transformed α titanium enriched to 7.6 to 8.3 weight percent and vanadium depleted to 2.7 to 3.2 weight percent at cooling rates of 20 to 275 °C/s. The significance here is that elemental segregation occurs during a single cooling path through the transformation zone. Banerjee *et al.* (2003) used the LENS process to deposit a compositionally graded titanium-vanadium alloy where the vanadium composition varied from 0 to 25 weight percent. Using Transmission Electron Microscopy (TEM) based Energy Dispersive Spectroscopy (EDS) at locations in the deposit with overall vanadium composition of two atomic percent, Banerjee *et al.* (2003) observed a segregated depletion of 0.5 atomic percent aluminum in transformed α titanium laths and 5 atomic percent vanadium enrichment in the inter-lath spaces. The magnitude of vanadium segregation observed by Banerjee *et al.* (2003) was much greater than that observed by Ahmed and Rack (1998). However, the LENS process employed by Banerjee *et al.* (2003) involved multiple thermal cycles passing through the transformation zone whereas the Jominy quench technique employed by Ahmed and Rack (1998) involved a single cooling transit through the transformation zone.

What is unique about the additive processes? Similar to multi-pass welding processes, both the base material and weld deposit material undergo multiple thermal cycles. For materials that undergo phase transformations, deposited materials can pass

through the phase transformation multiple times. For Ti-6Al-4V, the passage of the β to

α transformation front results in acicular needles when viewed in cross section as shown

in Figure 2.16b. As the temperature decreases, we propose that at the β to α

transformation front, acicular needles transform to the c-axis of the resulting HCP α

plate-like lath. These needles may nucleate along β to β interfaces or at existing α/β

interfaces. The tapered needle growth consumes the β grain as adjacent needles grow

laterally in the plane of the transformation front. Furthermore, we hypothesize that

elemental segregation by diffusion occurs at the interface of the growing α needle,

favoring α stabilizing elements in the needle side of the interface and thus favoring

enrichment of β stabilizing elements in the residual β grain. As α needles converge, the

space in between is enriched by β stabilizing elements. When the temperature increases,

and the direction of motion of the transformation front reverses, then all previously

transformed α grains revert to the BCC β structure. While there is a driving force for

elemental segregation in the β to α transformation, there is no segregating driving force

from α to β, because aluminum and vanadium are both stable in solid solution with

titanium in the BCC crystal lattice above the β transus temperature.   Consequently, any

elemental segregation resulting from a β to α transformation will remain in place, unless

the temperature increase reaches the homogenization temperature.

2.6   Conclusions

Several conclusions can be made when fabricating a functionally graded Ti-6Al-

4V alloy with boron through a LENS process:

1. The chemistry composition influences the proper depth of penetration to alleviate process pores during deposition. In this case the chemistry gradients of titanium, aluminum, vanadium, and boron throughout the multilayered LENS build process induces a changing depth of penetration causing complexities in the control loop of the LENS process and hence uncertainties in the multiscale heterogeneous structures. The heterogeneous structures include process related porosity which increased when depth of penetration decreased and height of deposit increased.

2. The boron affected the solidification characteristics, which in turn determined the primary β titanium grain size. When the boron weight percent is 0.25%, the primary β titanium grain size saturated at a minimum level for the process variables in this study. A new term is "Borlite" is proposed as the TiB/Ti matrix material related to the liquid-solid transformation at the eutectic composition.

3. The aluminum and vanadium affected the characteristics of the β to α titanium transformation. The transformed titanium α lath size decreased from 2 μm to 0.2 μm as the aluminum and vanadium content increased from 0 to 6 percent and 0 to 4 percent, respectively.

CHAPTER III

A FUNCTIONALLY GRADED TITANIUM BASED ALLOY FOR HIGH

THROUGHPUT STRUCTURE-PROPERTY EXPERIMENTS

3.1   Abstract

In this study, we quantified the Structure-Property (SP) relations of a Ti-6Al-4V/TiB functionally graded material to assess its ability to withstand large strain deformation in a high throughput manner. The functionally graded Ti-6Al-4V/TiB alloy was created by using a Laser Engineered Net Shaping (LENS) process. A complex thermal history arose during the LENS process and thus induced a multiscale hierarchy of structures that in turn affected the mechanical properties. Here, we quantified the functionally graded chemical composition; functionally graded TiB particle size, number density, nearest neighbor distance, and particle fraction; grain size gradient; and porosity gradient. In concert with these multiscale structures, we quantified the associated functionally graded elastic moduli and overall stress-strain behavior of eight materials with differing amounts of titanium, vanadium, aluminum, and boron with just one experiment under compression using digital image correlation techniques. We then corroborated our experimental stress behavior with independent hardening experiments.

3.2   Introduction

In the context of evaluating new material systems, functionally graded materials can play an important role in quickly assessing the Process-Structure-Property (PSP)

53

relations. Originally motivated to evaluate metallic composite materials, Niino *et al.* (1987) introduced a Functionally Graded Material (FGM). FGMs are innovative materials that belong to a class of advanced materials with varying properties over a changing dimension (Atai *et al.* 2012; Shanmugavel *et al.* 2012). By comprising a spatial gradation in structure and/or composition, FGMs are typically tailored to serve a specific function. As such, FGMs present an engineering approach to modify the structural and/or chemical arrangement of materials/elements rather than a technically separate class of materials. This approach is more beneficial when a component has diverse and seemingly contradictory property requirements, thus reflecting the necessity for FGMs that are used in engineering for different reasons.

FGMs can eliminate the sharp interfaces of composite materials that cause the failure to be initiated (Wang 1983). FGMs can also substitute a sharp interface with a gradient interface, which produces a smooth transition from one material to the next (Niino *et al.,* 1987). One main characteristic of FGMs is the capability to tailor a material for a specific application (Shanmugavel *et al.* 2012). FGMs established themselves as the material of choice for many applications in the aerospace (Marin, 2005), medicine (Matsuo *et al.*, 2001; Pompe *et al.*, 2003; Watari *et al*., 2004), defense (Lu *et al.,* 2011), optoelectronics (Kawasaki and Watanabe, 2002; Malinina *et al*., 2005; Woodward and Kashtalyan, 2012; Xing *et al.*, 1998), and energy (Müller *et al.*, 2003; Niino *et al.*, 2005) industries. The literature is very rich on this subject because of the broad areas of applications. A comprehensive review on the performance of FGMs was published by Birman and Byrd (2007). Regarding mechanical loadings, Malinina *et al.* (2005) investigated the performance of FGMs under localized transverse loading, and Liu *et al.*

54

(2011) conducted a property estimation study. Cherradi *et al.* (1994) and Tilbrook *et al.* (2005) reviewed the crack propagation in FGMs. Shanmugavel *et al.* (2012) published an overview on the fracture behavior of an FGM. Other researchers (Kou *et al.*, 2012; Olatunji-Ojo *et al.*, 2012; and Ruocco and Minutolo 2012) have also conducted analysis and modeling of FGMs. Due to the complexity and diversity of FGM systems, designing guidelines for the appropriate use of FGMs is difficult, so more research is still required to quantify the current qualitative information and provide comprehensive guidelines.

Several different fabrication techniques can produce FGMs with spatially heterogeneous multiscale structures. However, some limitations exist concerning the types of gradients that can be fabricated in the area of powder metallurgy. Different consolidation processes can be selected to avoid destroying or altering the gradient achieved by selective powder placement. Special attention to uneven shrinkage of FGMs during free sintering is a key focus area. With regard to porosity, particle size, shape, and composition of the powder mixture related to the sintering behavior, different material combinations and gradient types give a wide variety of sintering mechanisms (Schatt, 1992). Watanabe *et al.* (2009) validated that the grain size gradient and the composition gradient are controlled by thermal sintering rates. To overcome these problems, the superposition of the internal driving forces for sintering with an external pressure by hot pressing (Kimura and Toda, 1997) or hot isostatic pressing (Miyamoto, 2000) were performed , Although many of these methods for fabricating FGMs were investigated in the early 1990s, there are still limitations such as material combinations, specimen geometry, and cost. There are other fabrication methods for functionally graded materials

that offer comprehensive processing techniques of FGMs by Gasik (2010) and Kieback *et al.* (2003).

One of the established methods for creating an FGM is Additive Manufacturing (AM), which provides particular features such as higher fabrication rates, maximum material usages, less intensive energy demands, and the capability to manufacture complex shapes (Lin and Yue, 2005). Several AM technologies exist related to laser based heating for FGMs (Hutmacher *et al.*, 2004) that can be categorized in the following groups: laser cladding based method (Pei *et al.*, 2003; Yue and Li, 2008), Selective Laser Sintering (SLS) (Mumtaz and Hopkinson, 2007), 3-D Printing (3-DP) (Beal et al., 2007; D. Dimitrov *et al.*, 2006; Jackson *et al.*, 1999; Li *et al.*, 2000), Selective Laser Melting (SLM) (Beal *et al.*, 2007; D. Dimitrov et al., 2006; Jackson et al., 1999; Mumtaz and Hopkinson, 2007), and Laser Engineered Net Shaping (LENS) (Keicher and Miller, 1998).

Maybe one of the most widely used AM technologies is LENS (Keicher and Miller, 1998;Brooks *et al.,* 1999). In the LENS process a powder feedstock is used, which provides the flexibility to deposit blends of elemental and pre-alloyed powders to create components. Due to the wide ranging applications of Titanium (Ti) based alloys in the aerospace industry and the ability of LENS technology to manufacture components with complex geometry, recent investigations have been conducted using Ti powder as the primary powder and LENS as the fabrication technique (Griffith *et al.* 2000; Banerjee *et al.*, 2002; Schwendner *et al.*, 2001). One study using LENS for a functionally graded material employed TiC and Ti (Liu and Dupont, 2003). However, noticeable research has been dedicated to developing novel processing routes for Ti alloy and TiB composites.

These composites provide remarkable properties such as increased stiffness, elevated temperature strength, good creep performance, fatigue resistance, and wear resistance as a result of combining the high strength and stiffness of the borides with the toughness and damage tolerance of a Ti-alloy matrix. Because of the low solubility of boron in both α and β Ti and rapid particle growth during subsequent thermo-mechanical processing, achieving a uniform distribution of boride particles in conventional ingot metallurgy is very difficult. Genç *et al.* (2006) and Banerjee *et al.* (2005, 2003) have discussed in detail the structure of the TiB precipitates formed in laser deposited (Ti-6Al-4V)–TiB composites. The mechanical properties of (Ti-6Al-4V)–TiB fabricated using powder metallurgy techniques, which contained either randomly oriented or aligned TiB reinforcements (Gorsse and Miracle, 2003). Ocelik *et al.* (2005) prepared by laser cladding to have an excellent wear resistance, have been studied.

The present study experimentally quantifies the Process-Structure-Property (PSP) relationships of a Ti–6Al–4V/TiB material using a pre-alloyed Ti–6Al–4V and Ti-1B powder via the LENS process. Mechanical properties of different chemistries are efficiently quantified for this particular FGM using the LENS processing methodology. We also analyzed the change in mechanical properties that arise from a heat treatment following the LENS processing. We would like to propose to the reader that a particular "material" does not arise just from the chemistry as this particular chemistry will give rise to different multiscale structures depending upon the temperature histories in the processing (from both LENS and heat treatment) and as such different mechanical properties.

3.3   Materials and Experimental Methods

The metal alloy explored in this study was a composite incorporating the titanium alloy (Ti-6Al-4V) and titanium boride (Ti-1B) arranged as an FGM in composition between the two. An OPTOMEC LENS® 750 machine with a dual powder feeder was used to fabricate the AM-FGM specimens. The first powder feeder contained the Ti-6Al-4V powder, and the second feeder contained Ti-1B powder. Both powders were spherical in shape with sizes between 20 μm and 140 μm. The variation in composition was achieved by adjusting the flow rate of the powder according to Table 3.1.

Table 3.1   The amount of powder initially laid down for each layer in the functionally graded titanium alloy.

Layer #	Layer Thickness		Ti-6Al-4V powder (vol.%)	TiB powder (vol.%)
	(inches)	(mm)		
1	0.0625	1.588	100	0
2	0.0625	1.588	90	10
3	0.0625	1.588	75	25
4	0.0625	1.588	60	40
5	0.0625	1.588	40	60
6	0.0625	1.588	25	75
7	0.0625	1.588	10	90
8	0.0625	1.588	0	100

Figure 3.1 shows how the eight compositionally graded layers were deposited on a substrate of commercially pure titanium plate (thickness=6.35 mm).
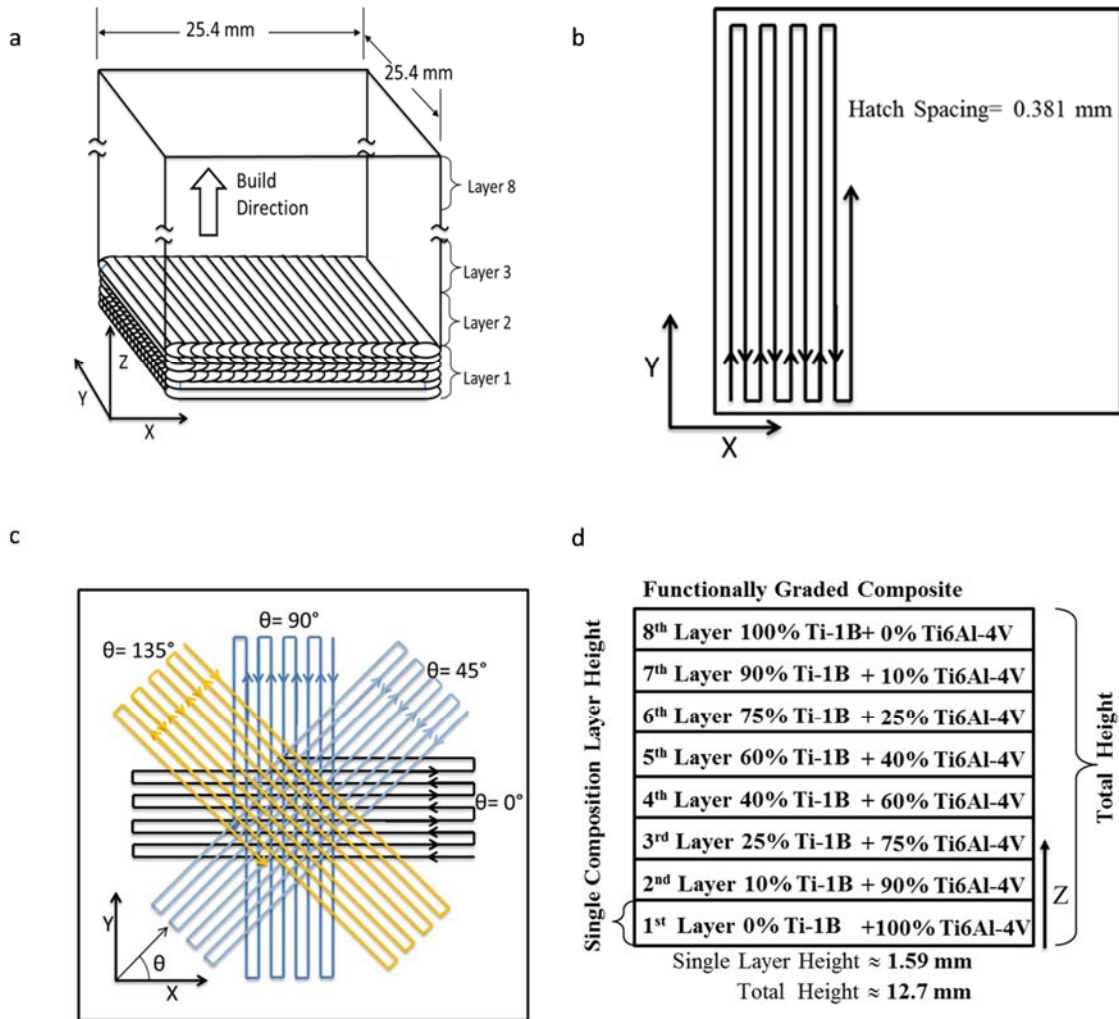
Figure 3.1   Schematics showing the processing steps of the Laser Engineered Net Shaping (LENS) method

Schematics showing the processing steps of the Laser Engineered Net Shaping (LENS) method: (a) Diagram of build tool path, (b) the in-plane single pass path, (c) the changing layer direction with each layer comprising six passes, and (d) the volumetric compositions of eight layers (0.062-inch thickness per layer).

A layer is defined as a sequence of deposition passes with the same specified composition. An open loop tool path was specified for each deposition layer (or slice) consisting of an initial perimeter contour pass and a linear parallel-hatch fill pattern with a hatch spacing of 0.381 mm (Figure 3.1b). The orientation angle of the linear hatch fill

59

was randomly selected from the set (0°, 45°, 90°, and 135°) as shown in Figure 3.1c. The planned slice thickness was ~9 mils (0.229 mm), requiring 7 passes to reach the planned compositional layer thickness of ~63 mils (1.60 mm) Five specimens fabricated in the geometry shown in Figure 3.1 were manufactured one at a time (multiple-build) vertically on a pure titanium (Grade 5) substrate. The AM processing chamber was purged with argon to control and maintain the oxygen concentration below 10 ppm.

Figure 3.2 shows the LENS deposition pattern related to the complex sequencing of the material processing. Figure 3.2a shows the build direction of the eight layers. Each single deposition pass added 0.229 mm of thickness as illustrated in Figure 3.1b. There are many passes to create a layer, and each pass is linear and parallel with pass spacing (sometimes called a "hatch") of 0.559 mm. Multiple passes occurred to create each layer and each pass orientation alternated between 0°, 45°, 90°, and 135° within each layer (see Figure 3.1c). As shown in Figure 3.1d, a sequence of eight layers were deposited as each layer was 1.59 mm thick with a total length of 12.7 mm.
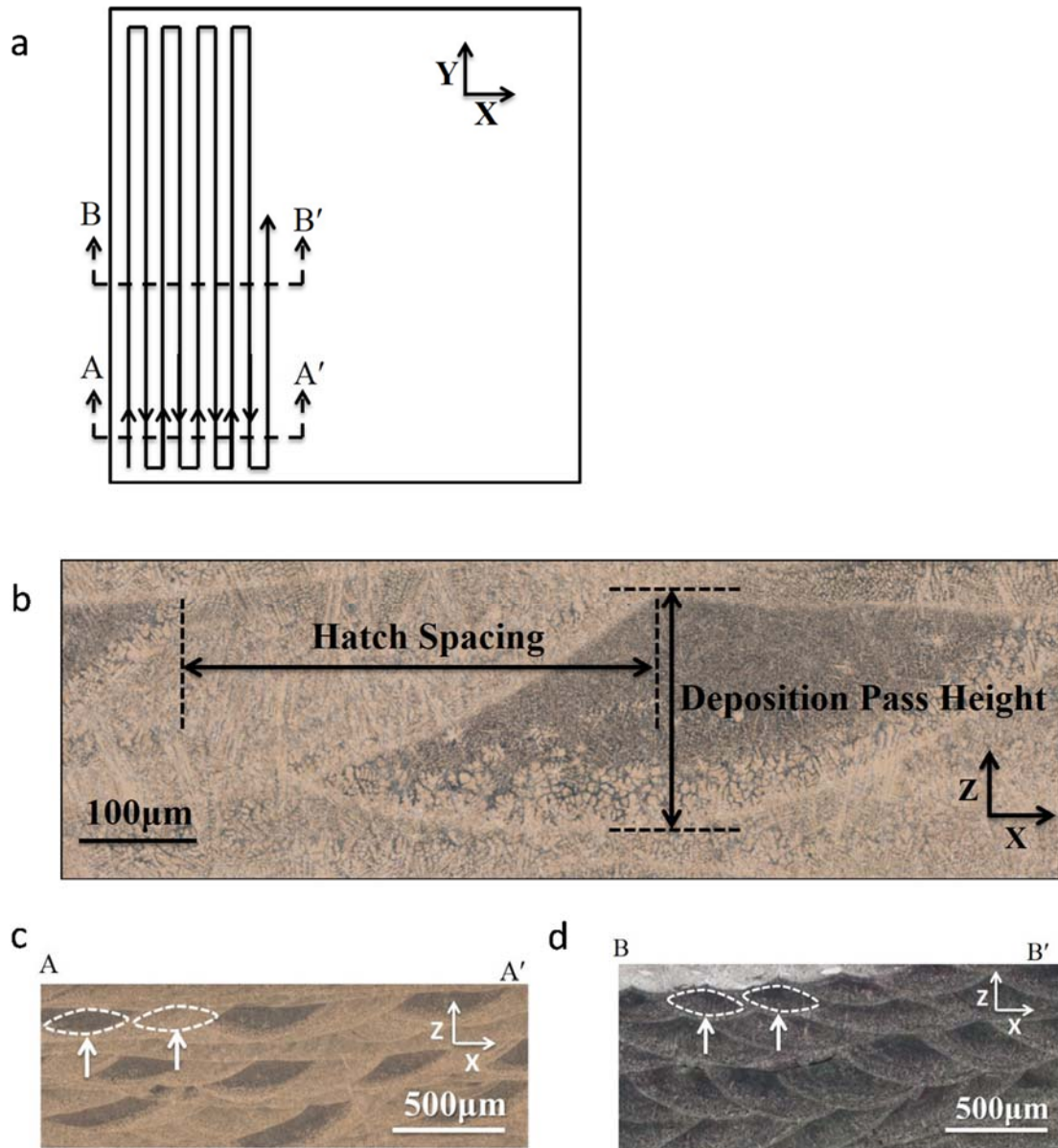
Figure 3.2   A schematic of the single pass within a layer and optical micrographs
              showing features of multiple LENS deposition passes from two locations.

 (a) A schematic of the single pass within a layer, (b) a cut of the specimen edge of the
single pass within a layer, (c) a cut of the middle of the specimen of a single pass within a
layer, and (d) an optical image of a single pass within a layer.

One of the square FGM builds was sectioned for destructive microstructural analysis. The material's multiscale heterogeneous structures were characterized by Optical Microscopy (OM), Scanning Electron Microscopy (SEM), Energy Dispersive Spectroscopy (EDS), Electron BackScatter Diffraction (EBSD), and x-ray Computed Tomography (CT), and the stereological quantities of number density, size, volume, nearest neighbor distance, and volume fraction were quantified using Image-J ("ImageJ," 1997) software. One square FGM build was heat treated at 1400°C for one hour in a tube furnace under flowing argon, then furnace cooled as shown in Figure 3.3.
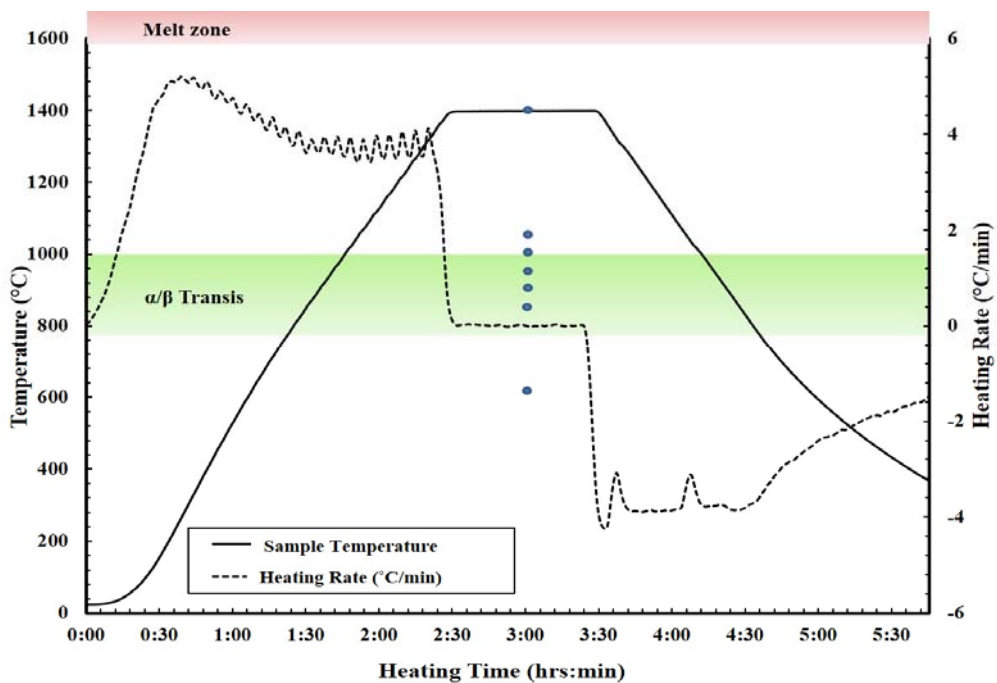
Figure 3.3   Temperature-time history of the heat treatment process.

The heat treatments for the AM specimens were selected to produce specimens with two sets of distinct microstructures (*i.e.*, pre- and post-heat treated) and to study their influence on mechanical properties. The 1400°C temperature reported in this study is higher than typically used for titanium heat treatments but was selected to modify the

morphology of the titanium boride particle phase. Cylindrical compression specimens (6.85 mm nominal diameter) were machined from the square FGM (both pre- and post-heat treated samples) by wire EDM. An Instron 5882 electromechanical testing system was used to perform all compression tests under a strain-controlled condition up to fracture. A constant strain rate was specified based on the initial specimens dimension, however because of anticipated gradation in yield point along the specimen axis, non-uniform deformation was expected thus producing strain rate gradients within the specimen. Consequently, sub-press with linear bearings was installed within the load frame to enforce uniaxial compression loading during the anticipated non-uniform deformation and to mitigate off axis loads. Digital Image Correlation (DIC) was used to determine full-field displacements during the compression tests. The local strains were derived from the displacement field during the whole loading process and true stress-strain curves were then calculated from the data.

3.4   Results

3.4.1   Microstructural Characterization

El Kadiri *et al.* (2008) discusses the complex thermal history of a low alloy steel and the associated complex microstructures demonstrating that for single wall builds, eight layers below the currently building LENS layer can still be affected by the high temperature (*i.e.*, heat input) at the laser surface. In the current study looking at the as-deposited microstructure of the FGM titanium alloy, we performed a post deposition heat treatment with the objective to homogenize the highest temperature feature (the boride whiskers).
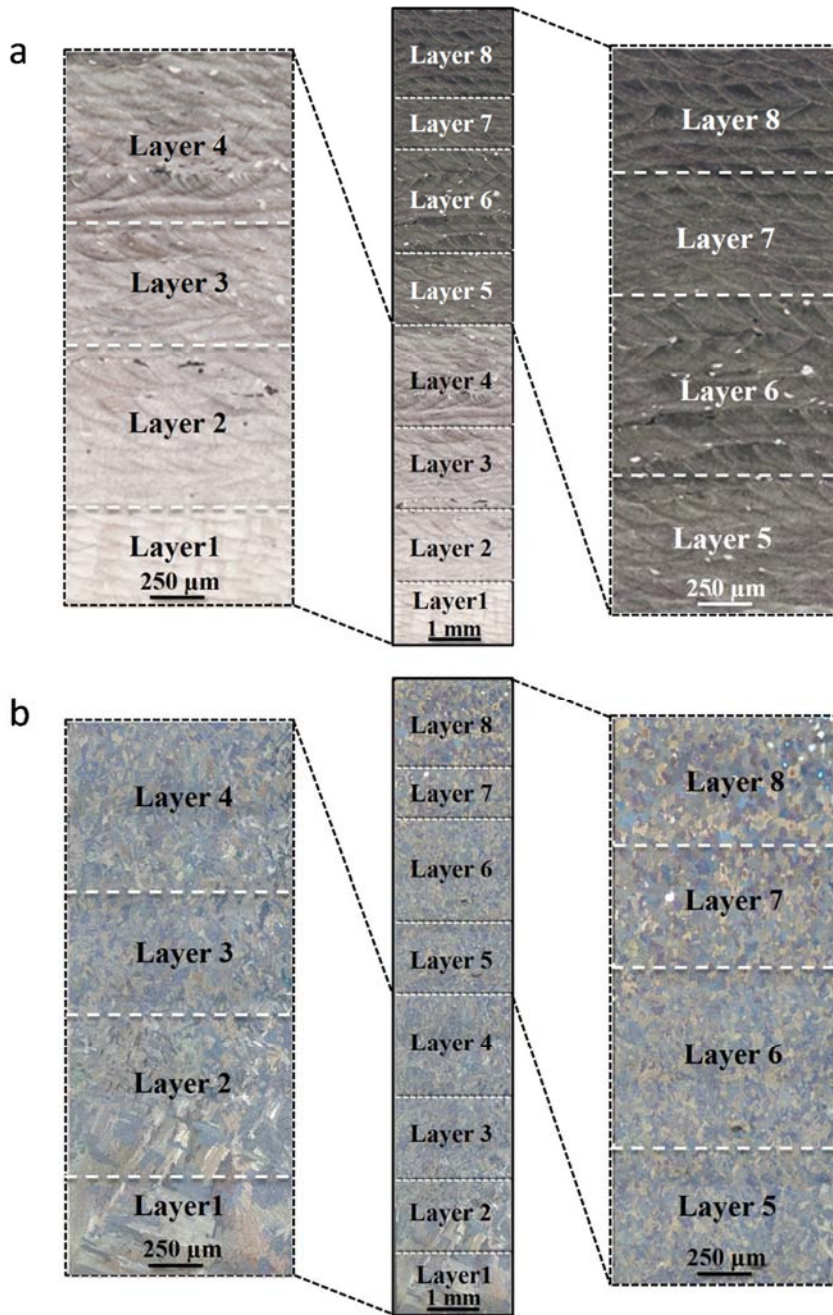
Figure 3.4   Optical micrographs of Ti-6Al-4V/Ti-1B Functionally Graded Material
              (FGM) fabricated by Laser Engineered Net Shaping (LENS) process.

Optical micrographs of Ti-6Al-4V/Ti-1B Functionally Graded Material (FGM) fabricated
by Laser Engineered Net Shaping (LENS) process showing a variation in microstructure
in and through the layers: (a) pre-heat treatment FGM (bright field image etched with
Krolls reagent) and (b) FGM post-heat treatment (polarized light polished with no etch).

64

Figure 3.3 shows the measured temperature history of the homogenizing heat treatment, and Figure 3.4b shows the corresponding microstructure. Note that the applied maximum temperature of 1400 $^{\circ}$C shown in Figure 3.3 was just below the melt zone (1600 $^{\circ}$C) but well above the alpha (α) to beta (β) phase transition zone (~800-1000 $^{\circ}$C).

Figure 3.4a shows bright field optical micrographs of the eight layers of material after LENS processing. The polished surface was etched with Kroll's reagent revealing many microstructural features. In Figure 3.4a, the presence of boride whiskers contributes to the darker shade; increased shading is visible from Layer 1 to Layer 8. Process heterogeneities such as pores due to lack of substrate penetration and partially melted powder particles entrained in the melt pool are visible in Layer 6. Non-homogeneous mixing is exhibited in Layer 4. Figure 3.4b shows a polarized light optical micrograph of a post-heat treated specimen that was polished without etching. Figure 3.4b shows that polarized light revealed the alpha (α) grain contrast, where the change in grain size is visible from Layer 1 to Layer 8. The planned elemental composition change from Layer 1 to Layer 8 in weight percent and atomic percent are shown in Figure 3.5a and 5b, respectively.
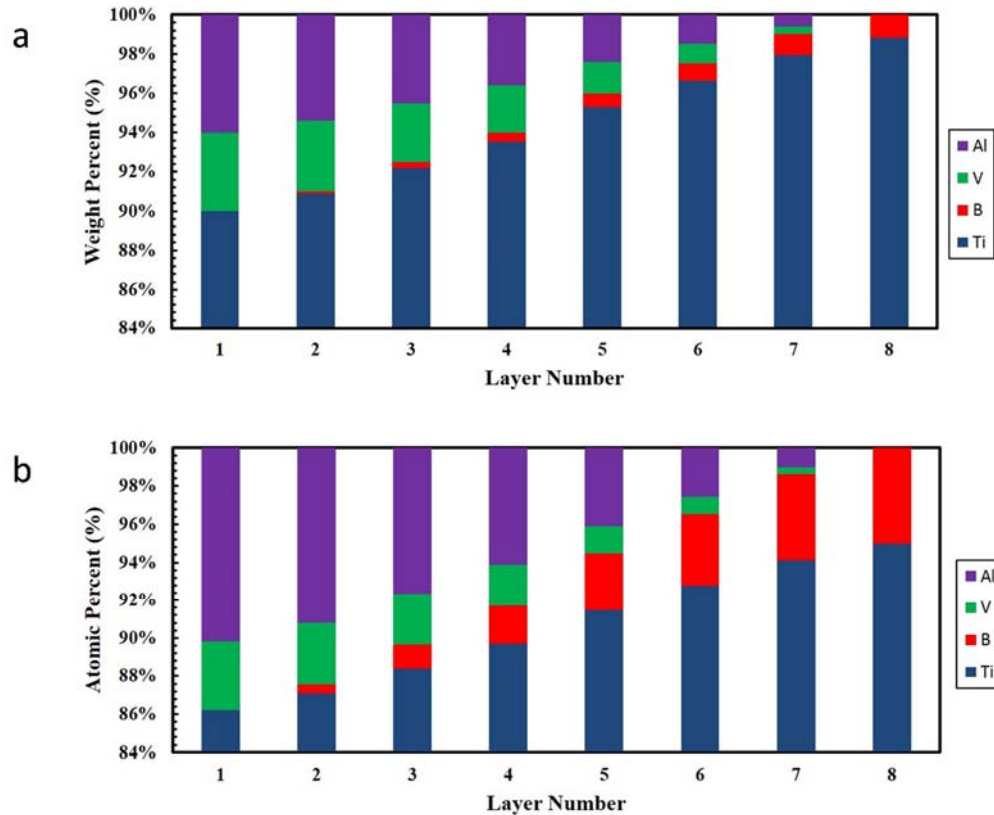
Figure 3.5   Mass distribution of aluminum, vanadium, titanium, and boron as a
               function of the vertical layering within the sample.

Mass distribution of aluminum (Al), vanadium (V), titanium (Ti), and boron (B) as a
function of the vertical layering within the sample. The composition shows from the
following perspective: (a) weight percent and (b) atomic percent.

To quantify structure-property relations through the FGM, the microstructural

features for each layer were measured. Table 3.2 summarizes the quantified values for the

different multiscale structures found within the FGM titanium alloy described herein

related to Figures 5, 9, 10, 11, 12, and 14. EDS chemistry measurements were conducted

on scanned rectangular regions (200 μm x 400 μm) spaced 256 μm apart.

Table 3.2   Elemental and microstructural quantification of the functionally graded titanium alloy (pre-heat treatment).

Layer	Ti (wt.%)	Al (wt.%)	V (wt.%)	B (wt.%)	Prior β Ti		α Ti Lath			Porosity (vol %)
					Grain Size (µm)	Grain Aspect Ratio	Grain Size (µm)			
							Alpha Lath Thickness	Primary Dendrite Arm Spacing	Secondary Dendrite Arm Spacing	
1	90	6	4	0	225.054	3.754	0.23	--	--	0.5
2	90.9	5.4	3.6	0.1	341.618	5.725	0.61	5.36	--	0.2
3	92.2	4.5	3	0.25	71.576	4.197	0.78	3.67	--	0.1
4	93.5	3.6	2.4	0.4	71.798	2.847	1.04	2.59	--	1
5	95.3	2.4	1.6	0.6	98.086	3.871	1.3	--	1.41	0.6
6	96.6	1.5	1	0.75	78.981	3.596	1.31	--	1.93	0.05
7	98.1	0.6	0.4	0.9	11.259	4.681	1.95	--	1.38	3.5
8	99	0	0	1	89.529	3.351	1.62	--	1.12	0.3

Table 3.3   Elemental and microstructural quantification of the functionally graded titanium alloy (post-heat treatment).

Layer	Ti (wt.%)	Al (wt.%)	V (wt.%)	B (wt.%)	TiB				Prior β Ti		α Ti Lath		Porosity (vol %)
					Number Density (#/μm^2)	Particle Size (μm)	Nearest Neighbor Distance (μm)	Volume Fraction	Grain Size (μm)	Grain Aspect Ratio	Transformed α Lath Size (μm)	α Lath Aspect Ratio	
1	90	6	4	0	1.29×10^{-5}	37.3	65.6852	0.048	1814.2	1.173	219.385	2.663	0.5
2	90.9	5.4	3.6	0.1	3.90×10^{-3}	22.3	3.7941	0.87	486.1	1.399	87.128	3.354	0.2
3	92.2	4.5	3	0.25	1.20×10^{-3}	32.8	0.887	3.93	570.2	2.063	72.984	3.347	0.1
4	93.5	3.6	2.4	0.4	1.18×10^{-3}	29.49	0.737	3.48	549.0	1.793	75.651	4.139	1
5	95.3	2.4	1.6	0.6	1.98×10^{-3}	34.2	0.7341	6.78	280.2	1.093	52.723	2.859	0.6
6	96.6	1.5	1	0.75	2.10×10^{-3}	37.7	0.3794	7.92	275.3	1.580	34.717	3.03	0.05
7	98.1	0.6	0.4	0.9	2.01×10^{-3}	47.49	0.4469	9.56	82.3	1.883	65.772	2.74	3.5
8	99	0	0	1	2.23×10^{-3}	39.8	0.4626	8.88	83.1	1.537	96.272	2.351	0.3

68
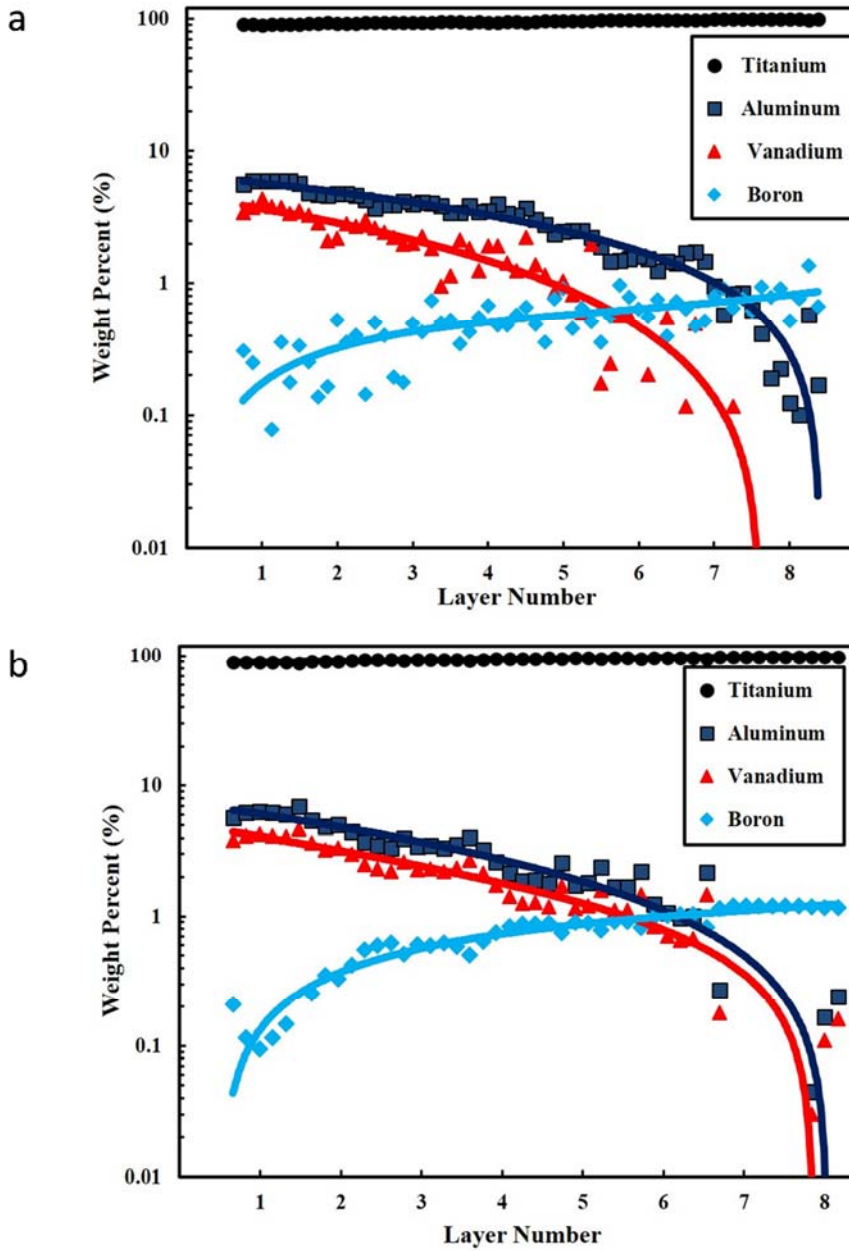
Figure 3.6   Weight percentage of the different materials through the eight layers of the functionally graded material for pre-heat treatment and post-heat treatment conditions.

Weight percentage of the different materials through the eight layers of the functionally graded material for (a) pre-heat treatment and (b) post-heat treatment conditions.

Figure 3.6 illustrates the weight percentage of titanium, aluminum, and vanadium calculated from EDS measurements in a semi-log plot with a third order polynomial fit with R-value of 0.91. The boron R-value was approximately 0.6 due to uncertainty in the measurement, because the x-ray energy value for boron is close to the lower detection limit and instrumental noise increases near the lower limit. Figures 5 and 6 show that the weight percentage of Ti increased from Layer 1 to Layer 8 by 90% to 98%, and the weight percentage of B increased from Layer 1 to Layer 8 by 0.1% to 1.1%, respectively. Note also in Figure 3.6a that the amount of aluminum and vanadium decreased from Layer 1 to Layer 8 from 6% to 0.1% and 4% to 0.1%, respectively.

When comparing Figure 3.6a (pre-heat treatment) versus Figure 3.6b (post-heat treatment) in terms of material content, a main observation can be made: the heat treatment did not affect the titanium nor the aluminum volume fraction although the high temperature of the heat treatment enhanced the material diffusion through the titanium base. The objective of selectively prescribing the placement of the chemical composition was achieved (comparing Figures 3.5a with 3.6a) and maintained as illustrated within the EDS detection window of the pre- and post-heated specimens.

In order to capture the structure-property relationships, quantification of the stereological features of the TiB whiskers is needed. Figure 3.7 shows pre-heat treatment SEM micrographs of the second phase TiB whiskers (particles) at three different length scales: Figure 3.7a shows the layer scale (Layer 8) of the functionally graded material; Figure 3.7b shows the grain scale; and Figure 3.7c shows the whiskers. Note the heterogeneities at each length scale, particularly the directionality of the whiskers that would induce local anisotropic material behavior.

70
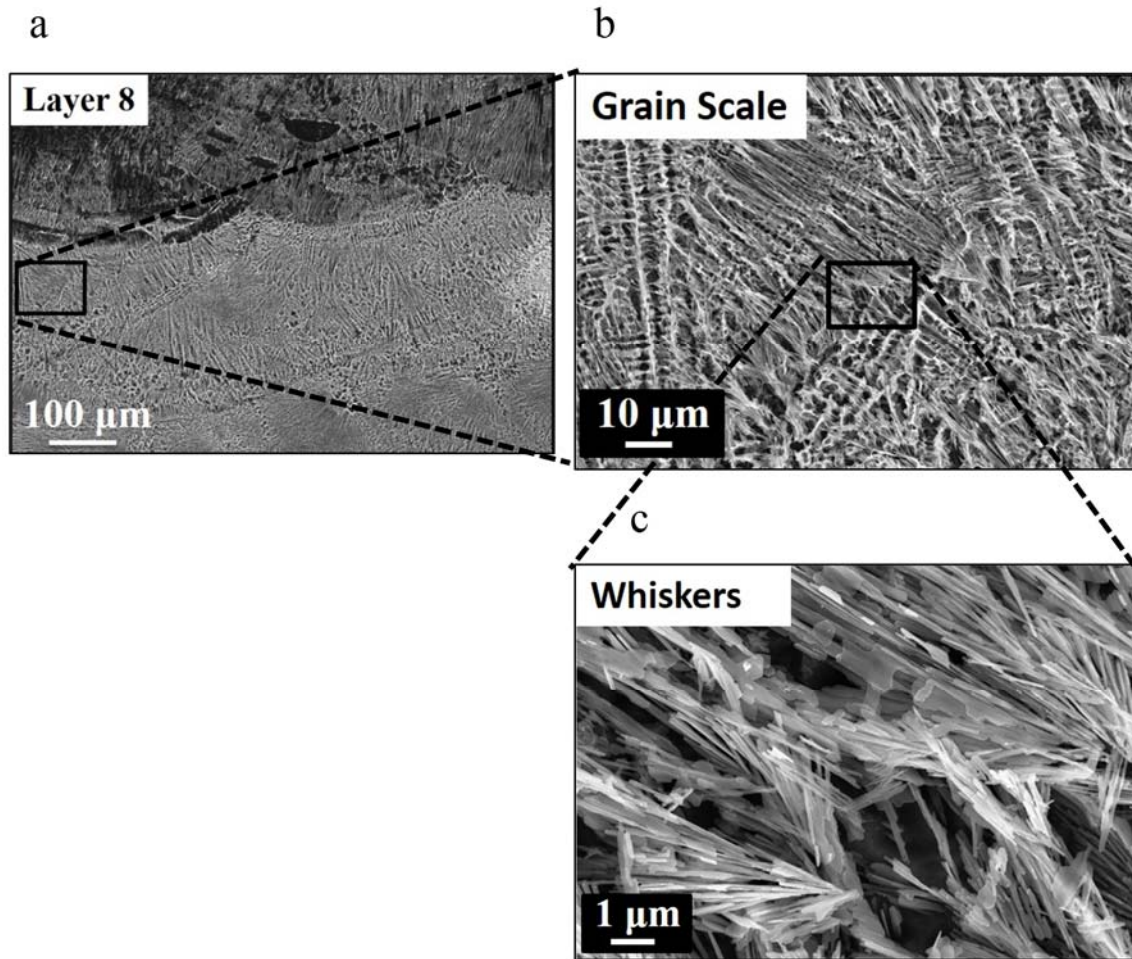
Figure 3.7   Pre-heat treatment scanning electron microscope micrographs with deep
etch to reveal the second phase TiB whiskers (particles) at three different
length scales.

Pre-heat treatment Scanning Electron Microscope (SEM) micrographs with deep etch to
reveal the second phase TiB whiskers (particles) at three different length scales: (a) Layer
8 of the functionally graded material, (b) grain scale, and (c) the whiskers.

Because of the clustering of the TiB whiskers, the whiskers were difficult to count

in the pre-heat treated specimens; however, we were able quantify the TiB particles after

heat treatment, because the heat treatment spheroidized the whiskers as shown in Figure

3.8.

71
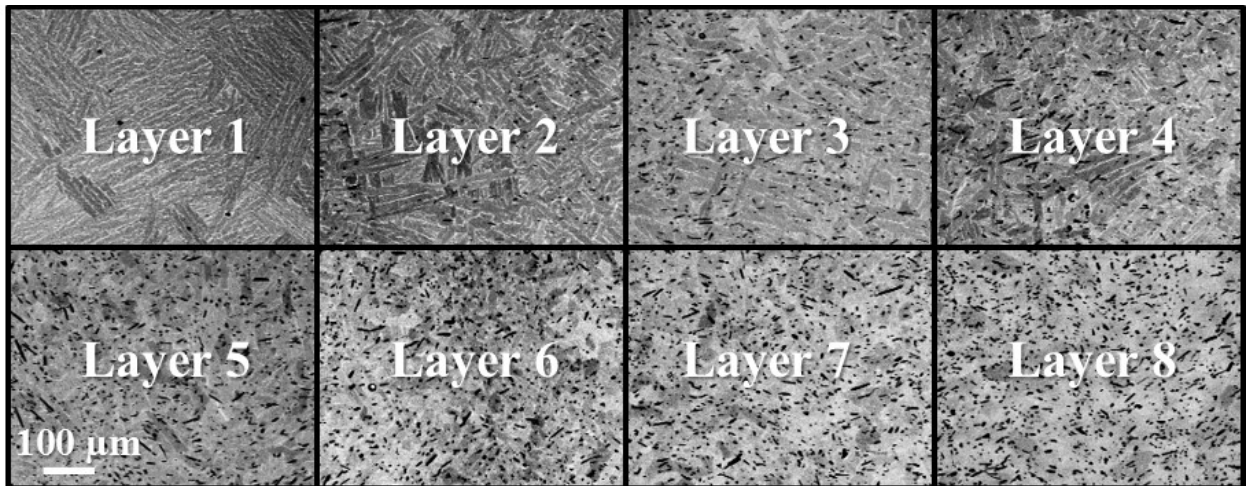
Figure 3.8   Post-heat treatment Backscattered Scanning Electron Microscope (SEM) images of eight layers showing second phase TiB particles.   Backscatter contrast highlights the TiB phase as black particles.

Figure 3.9 shows the number density of TiB particles after heat treatment increased from zero (Layer 1) to 0.0022 #/μm^2 (Layer 8) and the nearest neighbor distance correspondingly decreased from approximately 100 μm to 0.5 μm. In addition to the number density and nearest neighbor distance, we are also interested in the size and volume fraction throughout the functionally graded material. Figure 3.10 shows the post-heat treatment particle size and particle volume fraction in each layer. As the bulk composition of boron increased from Layers 1 through 8 (see Figures 5 and 6), the second phase TiB increased and similarly the particle size and volume fraction increased. Note that the TiB particle volume fraction increased from zero in Layer 1 to almost 9% in Layer 8.
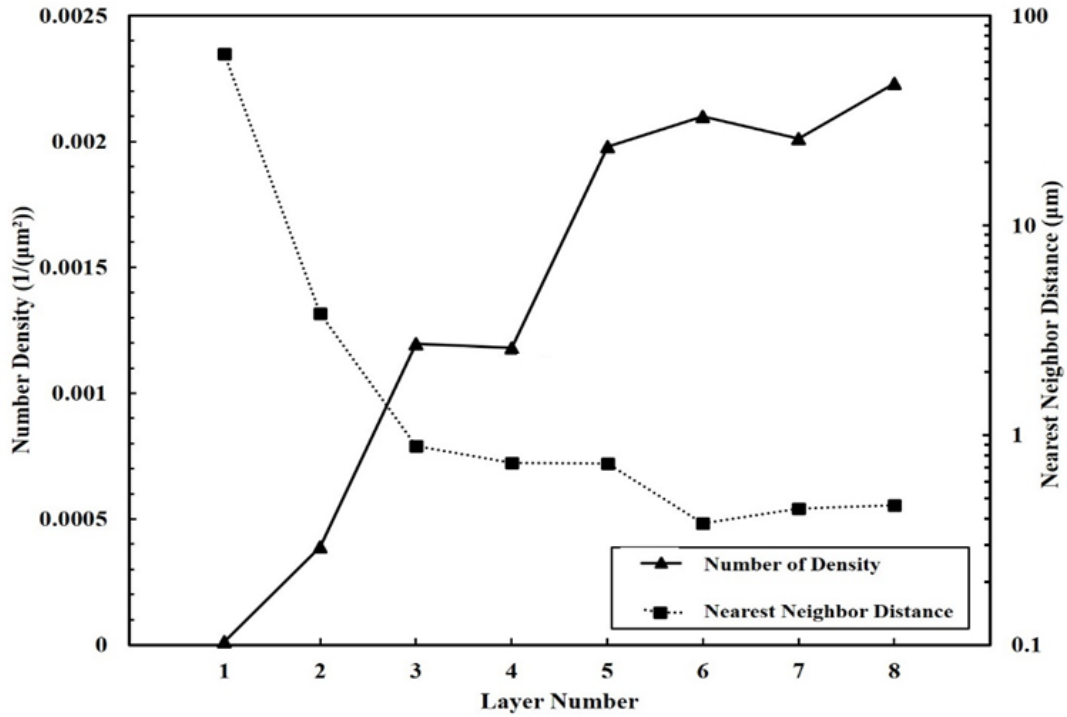
Figure 3.9   The change in number density and nearest neighbor distance of second phase TiB particles with respect to different FGM layers after heat treatment.

The change in number density and nearest neighbor distance of second phase TiB particles with respect to different FGM layers after heat treatment. As the weight percentage of the boron increases from Layers 1 through 8, the number density increases and the nearest neighbor distance correspondingly decreases.
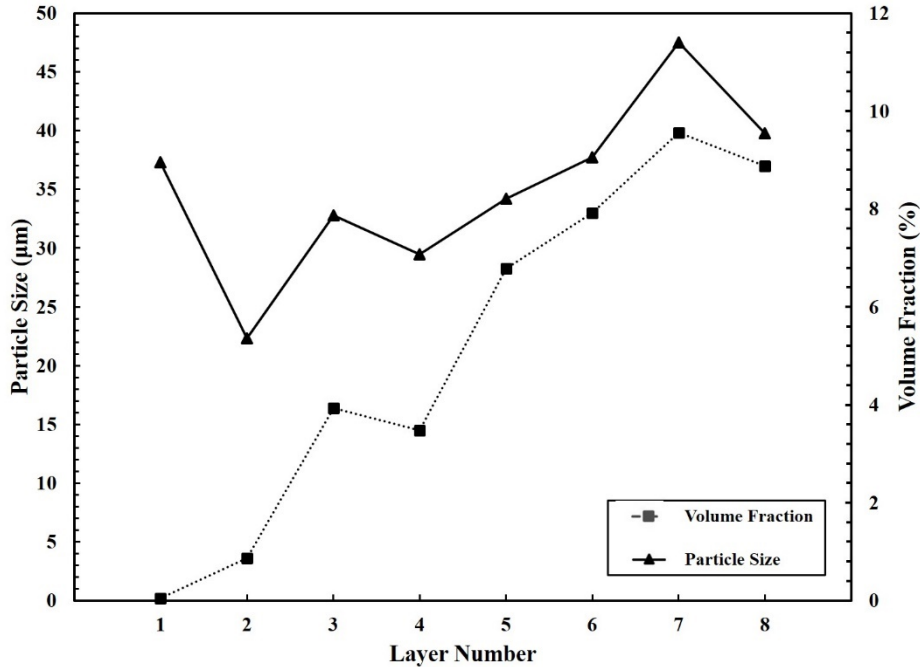
Figure 3.10   The change in particle size and volume fraction of second phase TiB
                particles with respect to different FGM layers after heat treatment.

The change in particle size (left y-axis) and volume fraction (right y-axis) of second
phase TiB particles with respect to different FGM layers after heat treatment. As the
weight percent of boron increases from Layers 1 through 8 the particle size and volume
fraction increases.

In addition to the particles, the phase and grain size measurements are important,

because they directly affect work hardening since dislocations and twins are prevalent in

this FGM titanium alloy, and the phases and grain boundaries limit the dislocation and

twin activity. Figure 3.11 shows that the size of the prior β phase of titanium decreased

dramatically from Layer 1 (800 μm) to Layer 8 (100 μm). Also in Figure 3.11, one can

observe that the aspect ratio of the β phase grains moved from approximately 7:1 down

to 3:1 indicating a change from a more anisotropic morphology to a lesser anisotropic

morphology. Although the β phase became more equiaxed, clearly there was still

anisotropy present.

74
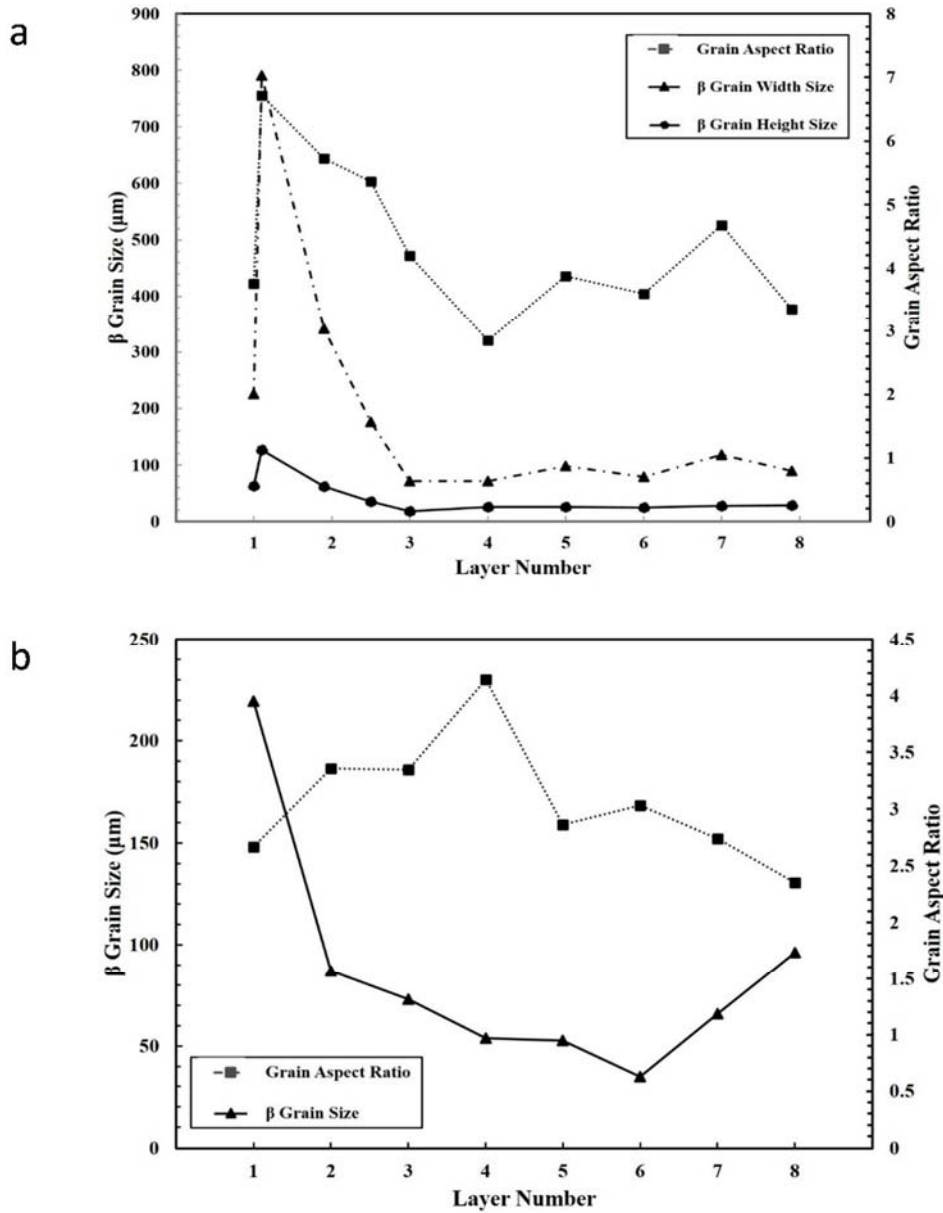
Figure 3.11   A comparison of effects of pre-heat treatment and post-heat treatment on
grain size of the titanium matrix (beta) phase as a function of the vertical
layering within the sample.

Comparison of effects of (a) pre-heat treatment and (b) post-heat treatment on grain size
of the titanium matrix (beta) phase as a function of the vertical layering within the
sample.

After heat treatment, the β phase changed the character of the FGM through Layers 1 through 8. Also, note from Figure 3.11 that the β phase size decreased in Layers 1-3 but Layers 4-8 were approximately equivalent to the pre-heat treatment values. This implies that the heat treatment had more influence on Layers 1-3 with respect to the β phase than Layers 4-8. When the FGM titanium alloy was heat treated, the typical spheroidization occurred as illustrated in Figure 3.11, which shows that the β phase particles had a closer aspect ratio to unity.

The porosity is another microstructural feature that affects the mechanical properties of a functionally graded material. The smallest pore defects observed in optical micrographs of polished sections show spherical shaped pores, most likely due to gas bubbles, as small as 9 microns. The more common porosity defects are much larger and have a flattened irregular shape occurring at deposition layer interfaces and are associated with lack of penetration defects. The detection threshold for the x-ray CT in this study is 1.0×10^{-4} mm^3, which is equivalent to a spherical pore with diameter ~60 microns. Figure 3.12a shows the porosity distribution that arose from the layering process and the quantified 3D porosity (pore volume fraction) data as a function of the layering. Figure 3.12b pictorially shows an x-ray computed tomography analysis result in which a 2D mapping of 3D information illustrates the periodicity of the porosity. Clearly, the porosity magnitude increased from Layer 1 to Layer 8. Hence, the increase in porosity increased as the boron and titanium increased. Two observations can be made from examining Figure 3.12: (i) an oscillation of porosity arose from zero to a certain value about every other layer and (ii) the total porosity increased per layer from Layer 1 to Layer 8.
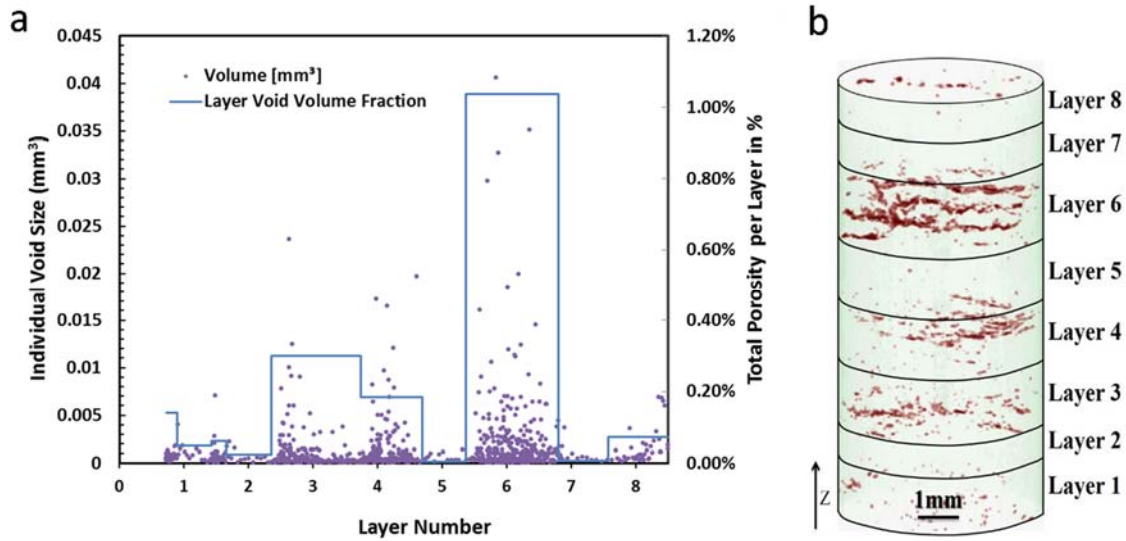
Figure 3.12   The porosity distribution of the functionally graded material in the pre-heat
treatment condition by computed tomography.

Computed tomography analysis result showing (a) the porosity distribution of the
functionally graded material and (b) the associated porosity values as a function of the
vertical layering within the sample obtained from pre-heat treatment condition.

The oscillation that occurred between the layers could arise because the control

system laying down the metal powder was planned for a certain height and when porosity

existed below the layer, the control system would try to adjust; hence, heterogeneities and

porosity distributions arose as evidenced here. The total increase in porosity occurred as

each layer was added because the melt pool determined the porosity characteristics; as

such, the melt pool would have been greater as the layer number increased in parallel

with a decreased thermal conduction.

3.4.2   Mechanical Response

Compression tests were conducted on the LENS processed specimens (pre-heat treated) and those that were heat treated after the LENS processing (post-heat treated). A Digital Image Correlation (DIC) technique was used to capture the stress-strain behavior in each layer of the FGM. Figure 3.13 shows the different strain levels that were ascertained during the test.
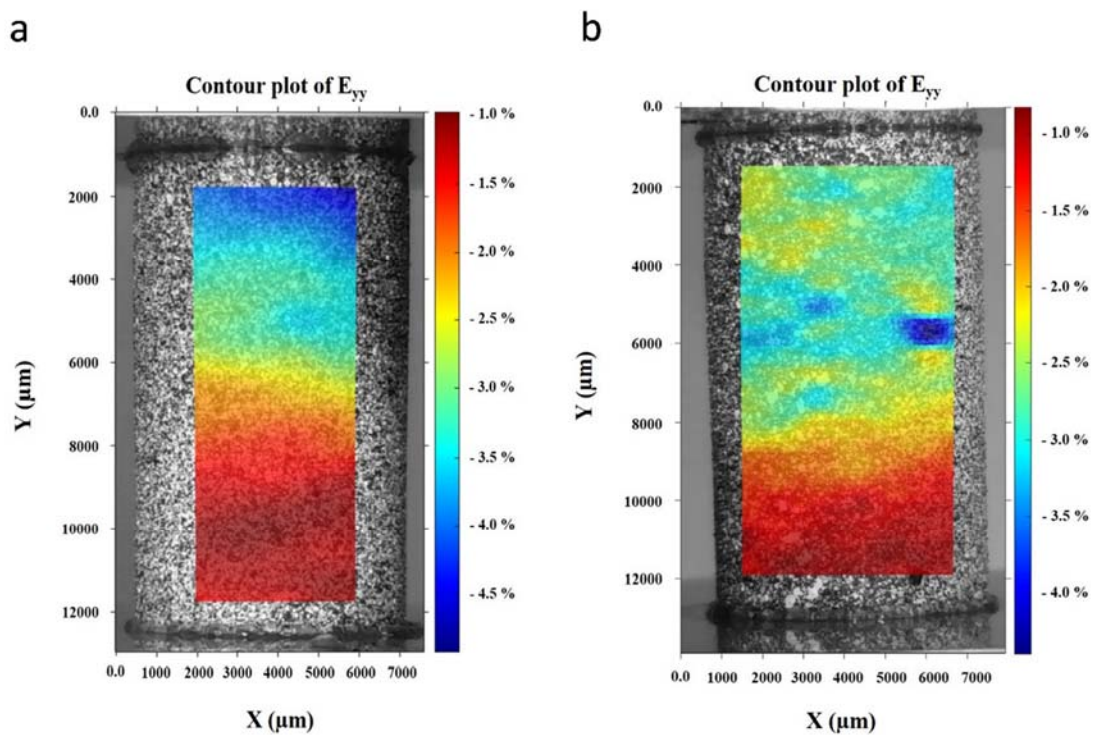
Figure 3.13   Strain contour maps from digital image correlation obtained during compression tests on the pre-heat treated and post-heat treated functionally graded titanium alloy.

Strain contour maps obtained during compression tests on the (a) pre-heat treated and (b) post-heat treated functionally graded titanium alloy using a Digital Image Correlation (DIC) methodology so that multiple stress-strain curves could be garnered with just one compression test.
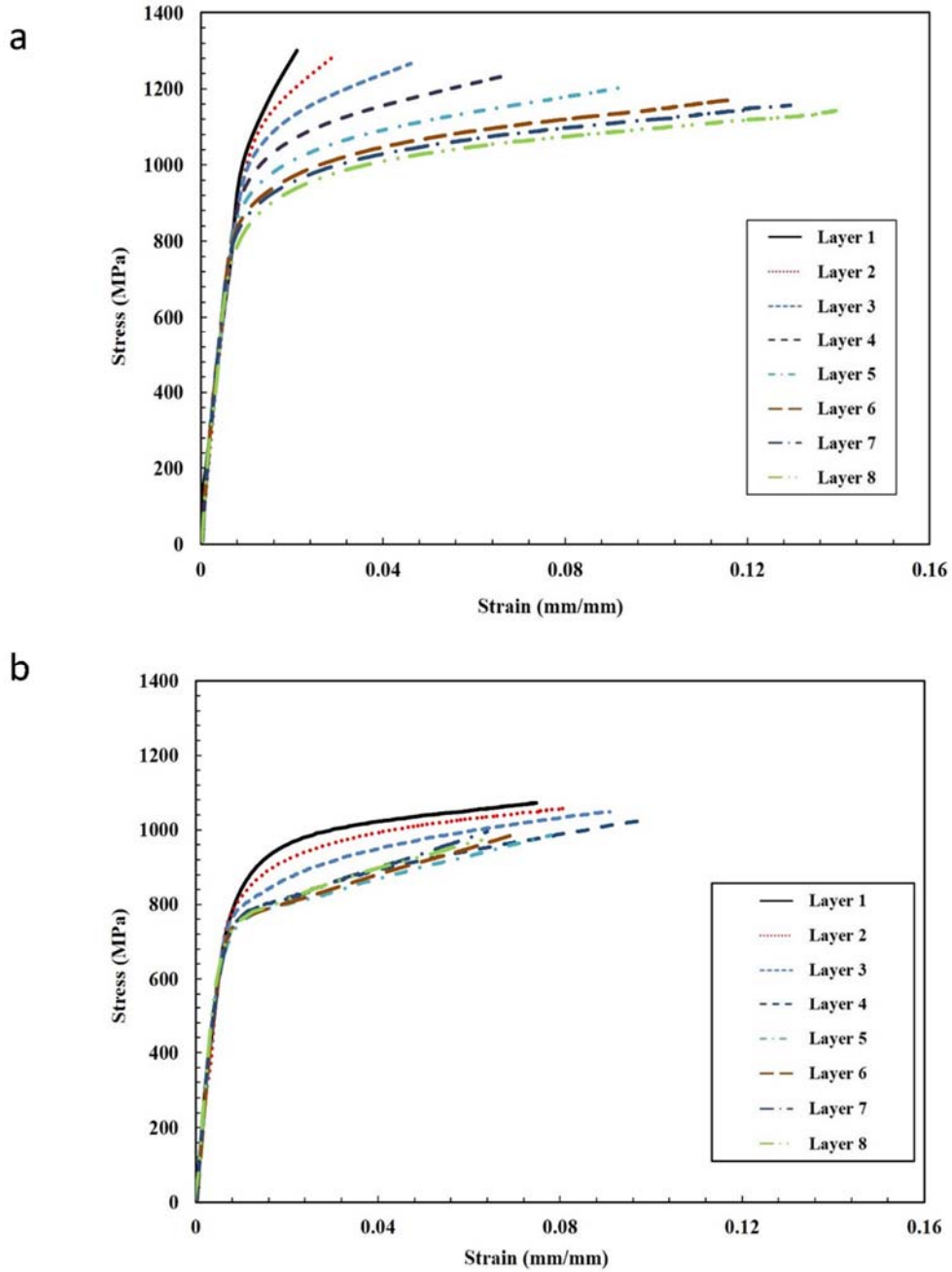
Figure 3.14   The Stress-strain behavior extracted by DIC method for each layer of the
functionally graded titanium alloy for the pre-heat treated and post-heat
treated.

The Stress-strain behavior illustrating the different strain levels extracted from each layer
of the material by DIC method for the (a) pre-heat treated and (b) post-heat treated
conditions.
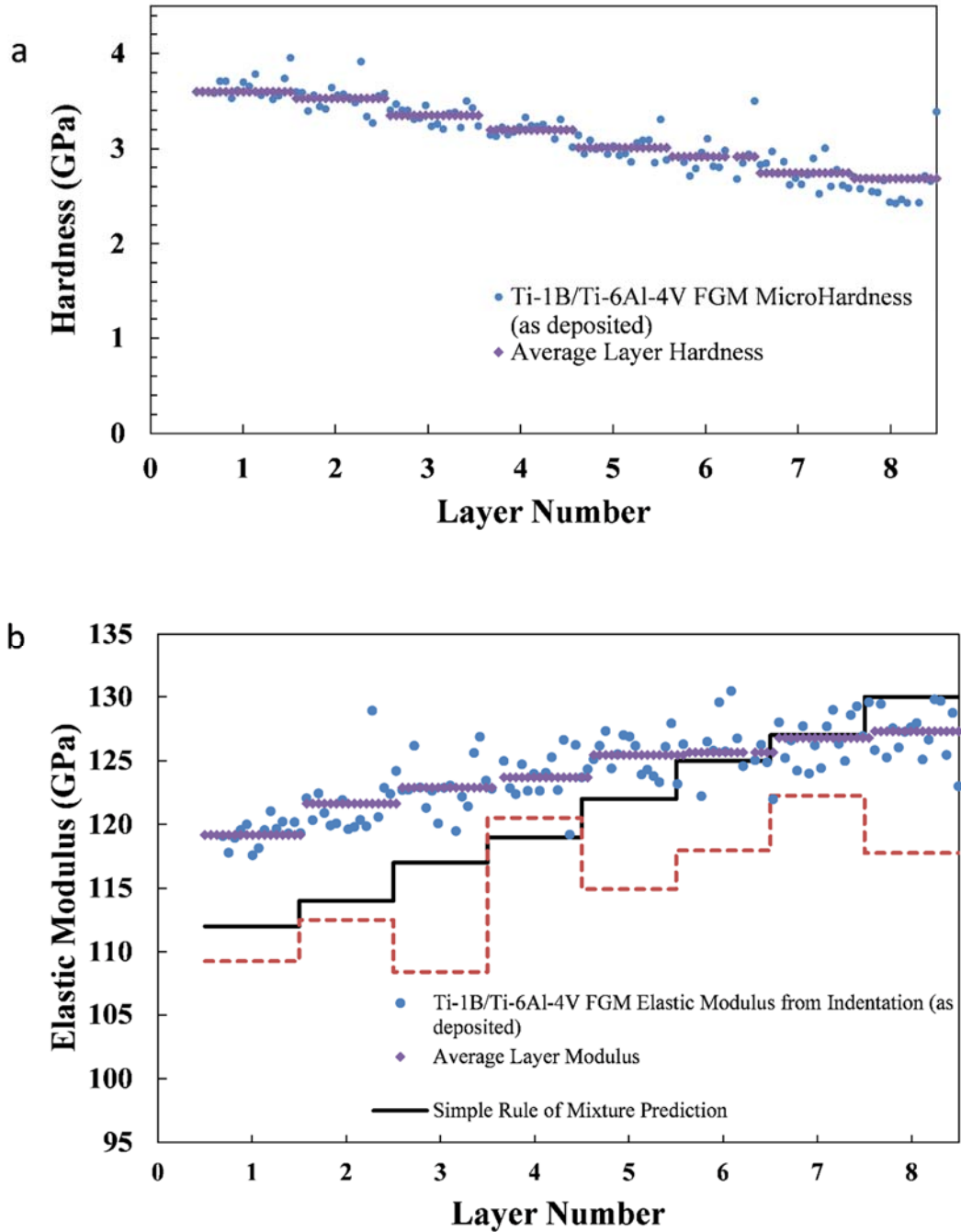
Figure 3.15   Microhardness and reduced elastic moduli as a function of the vertical
layering within the sample obtained from the pre-heat treatment condition.

The (a) microhardness and (b) reduced elastic moduli as a function of the vertical
layering within the sample obtained from the pre-heat treatment condition.

Note that the heterogeneous straining during this particular displacement level ranged from approximately 4% at the top to 1% at the bottom of the specimen. Alternatively, the load (and thus the stress) was the same throughout the specimen; as such, different stress-strain behaviors were captured with just one test! Figure 3.14 shows the pre-heat treated and post-heat treated stress-strain behaviors garnered from one compression test for each material type. Because this technique allows the retrieval of eight stress-strain curves from one test, it can be designated as a "high throughput" experiment. Note that the work hardening rate decreased in Figure 3.14a for the pre-heat treated FGM from Layers 1 through 8, but the decrease in work hardening rate for the heat treated FGM was much smaller, as illustrated in Figure 3.14b.

Instrumented indentation tests were conducted in a linear array at a spacing of 100 microns along a profile line of the specimen sectioned in the direction of functional grade for both pre-heat treated (Figure 3.15) and post-heat treated (Figure 3.16) LENS specimens in order to garner the hardness and elastic modulus values. Figures 3.15a and 16a show the hardness as a function of each layer while Figures 3.15b and 3.16b shows the reduced elastic modulus as a function of each layer. Table 3.4 summarizes the results for the elastic modulus and hardness values from different tests for each layer of the functionally graded composite. Table 3.5 illustrates the comparison of the predicted Young's modulus based on the role of mixture from elemental moduli with Young's modulus extracted from stress-strain curves. These results are consistent with the elastic modulus of cast material with similar composition (Sen, Tamirisakandala et al. 2007).

81
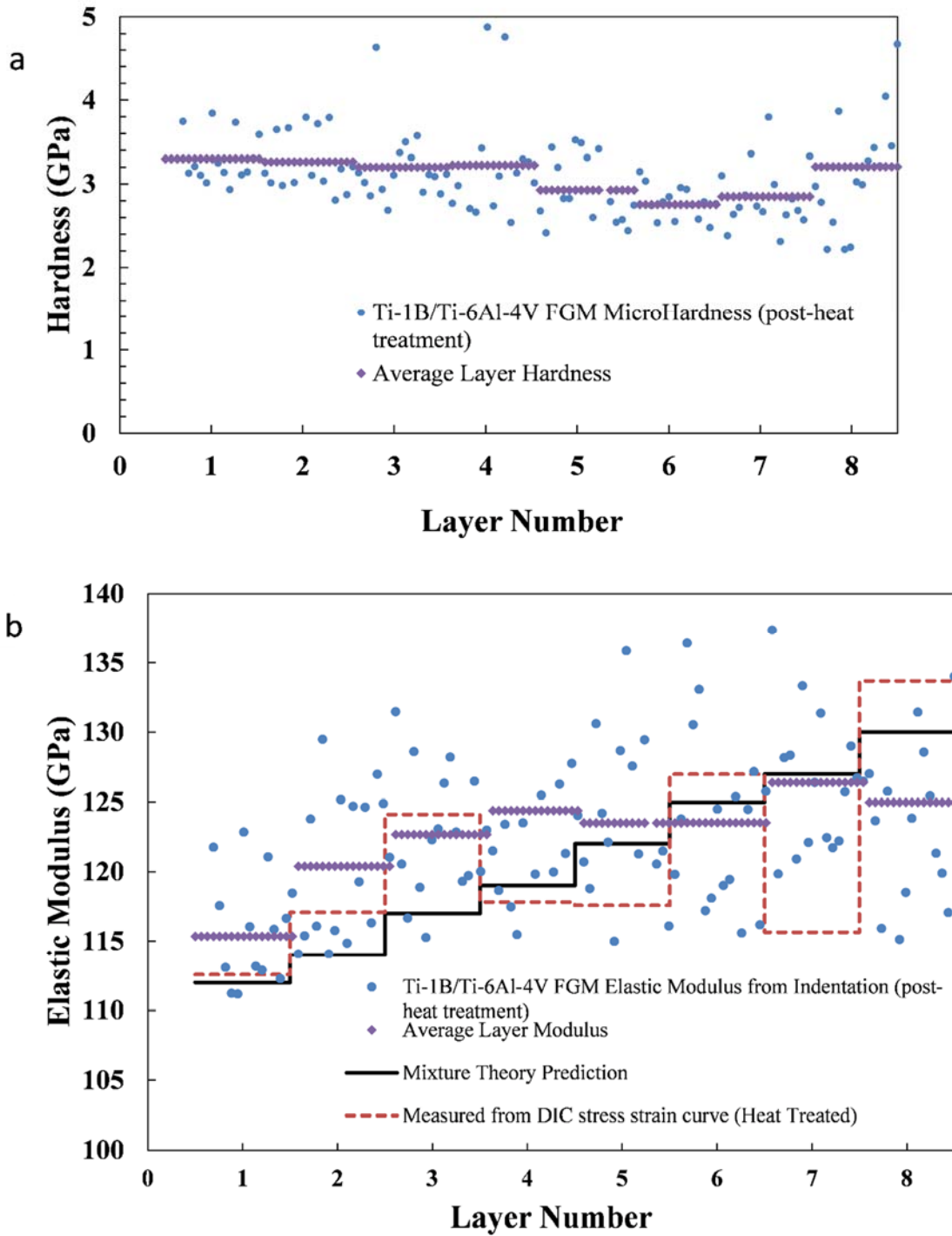
Figure 3.16   Microhardness and reduced elastic moduli as a function of the vertical layering within the sample obtained from the post-heat treatment condition.

The (a) microhardness and (b) reduced elastic moduli as a function of the vertical layering within the sample obtained from the post-heat treatment condition.

Table 3.4   Mechanical properties of the functionally graded titanium alloy.

| Layer	Yield Stress, σ_y (MPa)	Ultimate Stress, σ_{ult} at 8% Strain (MPa)	Tabor Hardness from σ_y (GPa)	Tabor Hardness from σ_{ult} (GPa)	Tabor Hardness Weighted Average σ_y and σ_{ult} (GPa)	Microhardness obtained from Indentation Test (GPa)	Percent Difference between Indentation and Weighted Tabor Average Hardness
1	1070	1430	3.21	4.29	3.58	3.60	0.6
2	1031	1380	3.09	4.14	3.45	3.53	2.3
3	1002	1320	3.01	3.96	3.33	3.35	0.5
4	951	1260	2.85	3.78	3.17	3.20	1.0
5	902	1178	2.71	3.53	2.99	3.01	0.7
6	865	1120	2.60	3.36	2.86	2.94	2.8
7	850	1096	2.55	3.29	2.80	2.74	2.2
8	810	1074	2.43	3.22	2.69	2.68	0.7

Table 3.5   Comparison of the Young's modulus between rule of mixtures prediction and Young's modulus extracted from stress-strain curve for as deposited material.

Layer	Volume Fraction (%)				Mixture Theory E_{Total} (GPa)	Elastic Modulus (GPa) σ-ε curve	Elastic Modulus (GPa) indenter
	Ti	Al	V	B			
1	0.855	0.102	0.036	0.007	108	109	119.2
2	0.862	0.092	0.032	0.014	111	112	121.6
3	0.876	0.077	0.027	0.021	113	108	122.9
4	0.890	0.061	0.022	0.027	116	121	124.0
5	0.910	0.041	0.014	0.034	118	115	125.4
6	0.924	0.026	0.009	0.041	120	118	125.6
7	0.938	0.010	0.004	0.048	124	124	126.8
8	0.945	0.000	0.000	0.055	126	118	127.3

Comparison of the predicted Young's modulus based on the rule of mixture from elemental moduli with Young's modulus extracted from stress-strain curve for as deposited material. Elastic Moduli used for rule of mixtures for titanium, aluminum, vanadium, and boron are 110, 68.9, 128, 400 GPa, respectively.

3.5   Discussion

The PSP relationships quantified herein for a functionally graded titanium alloy

have been garnered from the LENS processing method in which the thermal history plays

an important role. The various structures at different length scales are summarized in

Table 3.2, and the associated mechanical properties are summarized in Table 3.3. The stereological quantities for the multiscale hierarchical heterogeneous structures included the number density, size, nearest neighbor distance, and volume (sometimes area) fraction of the particles and also the different grain sizes, dendrite cell sizes, and lath sizes. The two different processing methods included the LENS process (pre-heat treated) and LENS plus heat treatment (post-heat treated), which in turn give different multiscale structures and mechanical properties. For the post-heat treated material, the α' laths increased in size so much that the β grain size had more of an effect on the flow stress such that the lath essentially went away. In our study, the heat treatment did indeed change the morphology of the hierarchical structures; hence, we would expect differences in the mechanical properties.

When examining different microstructures, Layer 1 exhibited three trends: (1) had the least amount of titanium and boron but the greatest amount of aluminum and vanadium; (2) had the lowest number density but greatest nearest neighbor distance, size, and aspect ratio for the β phase of titanium; and (3) had the least amount of porosity. Associated with these microstructures that arose from the as-cast LENS processing were the following: (1) the greater yield stress, (2) greater work hardening rate, and (3) greater hardness. Martensitic transformations occur at a lower cooling rates for Ti-6Al-4V than for pure titanium. Because of the high cooling rate associated with the LENS process, the β grains transformed by martensitic transformation into an α' lath structure. The α' lath size, shown in each layer in Table 3.2, is inversely proportional to the cooling rate and also acts as an effective grain size for Hall-Petch based hardening. The martensitic transformation also holds the aluminum and vanadium atoms into supersaturated α' laths.

84

This contributes to solution hardening. Because of the low volume fraction of TiB in this layer, there is little contribution to hardening from a particle mechanism.

The Layer 8 microstructures, which contained the least amount of aluminum and vanadium but the greatest amount of titanium and boron, had the greatest number density but lowest nearest neighbor distance, size, and aspect ratio for the β phase of titanium and had the greatest amount of porosity. Associated with these microstructures that arose from the as-cast LENS processing were: the lowest yield stress, work hardening rate, and hardness. These trends are, of course, the opposite of Layer 1. The absence of aluminum and vanadium in this layer reduces the contribution to solid solution hardening but also increased the cooling rate required to induce martensitic transformation in the pure titanium matrix. Consequently, the α' lath size of the transformed β matrix was greater for the same cooling rate compared to Ti-6Al-4V, reducing the hardening contribution due to the Hall-Petch mechanism. The volume fraction of TiB whiskers is the highest in this layer providing the largest contribution to hardening from the particle mechanism.

Table 3.4 summarizes the results for the elastic modulus for the functionally graded titanium alloy. Three different methods were used to corroborate the elastic modulus results: simple rule of mixtures theory, experimental stress-strain data, and experimental indenter data. The Young's modulus used for rule of mixtures for titanium, aluminum, vanadium, and boron are 110, 68.9, 128, 400 GPa respectively. Some minimal variation in the experimental data for Young's modulus for Ti-6Al-4V in the literature (Gorsse and Miracle, 2003) ranges from 114 to 116 GPa. When comparing the three methods, the trend of having the lowest Young's modulus in Layer 1 increasing to the largest Young's modulus in Layer 8 was consistent. In fact, there was less than a 5%

difference between the mixture theory and the stress-strain data and less than 9% between the mixture theory and indenter data. Clearly as more boron was present, the elastic modulus proportionally increased.

The hardness values from the indenter and Tabor (2000) calculations show a very close comparison when examining the data from Table 3.3. Sometimes the yield and sometimes the ultimate stress are used to determine the hardness, so we employed a weighted average (66% for yield and 33% for the ultimate stress) to compare to the indenter data. The results show that the hardness values corroborate each other as they are less than 3% different throughout the length of the eight layer specimen.

The heat treatment modified several structural features: lath thickness, supersaturation of aluminum and vanadium, size of the TiB particles, and matrix grain size. A heat treatment temperature of 1400°C was chosen to be high enough to modify all of the constituent structures. This temperature is above the β-transus temperature, which means that all metal matrix grains (from Layer 1-Ti-6Al-4V to layer 8-Titanium) transformed to the β phase and grew. The chosen temperature was also above the homogenizing temperature such that any solute segregation in the transformed β grains should have been eliminated. At the cooling rate of 4°C per minute, the larger β grains in Layer 8 appear to have transformed completely to α retaining the larger β grain boundaries. Layer 1 (100% Ti-6Al-4V), however, shows basket weave features of colony transformation The TiB whiskers consolidated into larger grains thus increasing the particle size, decreasing the particle number density, and decreasing the nearest neighbor distance. Because the as-deposited β grain size in the Layer 1 matrix was greater than the as-deposited size in Layer 8, the final grain size was greater for Layer 1 than for Layer 8.

However, because of the greater amount of aluminum and vanadium in Layer 1, an α-β basket weave lath formed when the temperature decreased below the β-transus. Because the cooling rate after the heat treatment was lower than the LENS cooling rate, β grains with low aluminum and vanadium transformed to α titanium by a massive transformation resulting in a final grain size close to the β grain size that was reached at the peak of grain growth during the heat treatment. Figure 3.14b shows that for Layers 4-8, the initial yield stress was similar with a sharper knee than Layers 1-3, and the hardening was nearly linear with a slope that slightly varies. Layers 1-3 retained a difference in initial yield and an exponential hardening with a difference in hardening rates.

The strength within each layer of the functionally graded titanium alloy was a function of the α' lath structure that induced a Hall-Petch relationship, the amount of vanadium as substitutional atoms, and the local lattice strength of the titanium. Within Table 3.3 we see the difference in the yield strength and ultimate stress as a function of the material gradation. The yield and ultimate strength of crystalline boron is approximately 3 MPa (Matweb, 2017). For vanadium, the yield strength is 454 MPa, and the ultimate strength is 536 MPa for a vacuum annealed sheet (Matweb, 2017). For titanium, the yield strength is 140 MPa, and the ultimate strength is 220 MPa (Matweb, 2017). For aluminum, the yield strength is 10 MPa, and the ultimate strength is 40 MPa (Nicholas 1980). Clearly, the vanadium was the only element added to the titanium that increased the yield and ultimate stresses; however, the small α lath size also played a role in strengthening the material.

Figure 3.17 shows a schematic for the cradle-to-grave CPSP simulation based design, illustrating the different LENS stages for the material such as powders, anneal,

87

grain/particle size, heat treat, and compression that corresponded to the chemical, process, structure, and properties, respectively. Each of these stages have their own residual stress and structure during the fabrication or post-fabrication process. In order to capture the history effects, robust models must be able to capture process induced changes to the structures. In this study, we did not employ a multiscale modeling analysis as that is planned for a separate work.
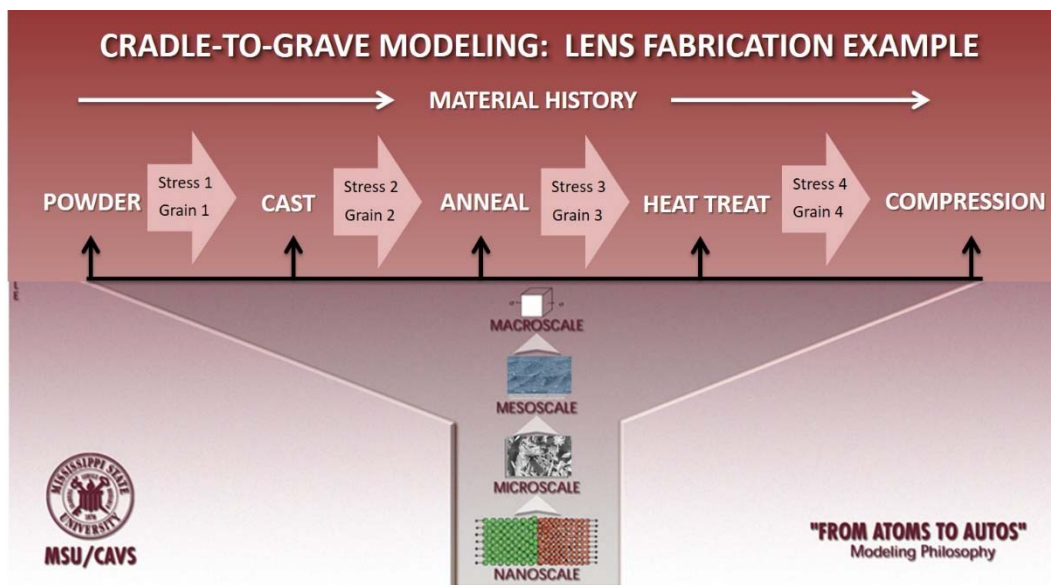
Figure 3.17   A schematic of cradle-to-grave sequence of Chemical-Process-Structure-Properties (CPSP) simulation based design.

 A schematic modified from Horstemeyer (2012). To capture the history effects, robust models must be able to capture process induced changes to the structures.

CHAPTER IV

CONCLUSIONS

4.1   Successful production of Functionally Graded Material

The following conclusions are garnered based on the observations made in this study:

1.   The Chemistry-Process-Structure-Property (CPSP) relationships were quantified for a functionally graded titanium alloy with alloying elements of aluminum, vanadium, and boron using the additive manufacturing method LENS. Two different material processing histories were considered: as-fabricated LENS and as-fabricated LENS followed by a heat treatment. The two different material histories gave rise to different hierarchical multiscale structures in terms of porosity, particles, and grain size. The different element compositions and multiscale structures gave rise to different constitutive behaviors as demonstrated by the mechanical stress-strain behaviors.

2.   Indentation measurements independently corroborated the hardness and elastic moduli gradient throughout the functionally graded titanium alloy that arose from the stress-strain experiment.

3.   High throughput stress-strain behavior based upon different element compositions that were functionally graded throughout the specimen can be efficiently garnered from one test if Digital Image Correlation (DIC) is used. This methodology can

be used for a quicker calibration of a constitutive model and hence can, in turn, be used

for design optimization of materials for the materials genome.

CHAPTER V

FUTURE WORK-COMPOSITE LAMINATES AND SIMULATIONS

5.1   Composite Laminates

This study has focused on a functionally graded material where properties are graded from a one single material to another single material. Future studies will focus on layered materials with alternating material properties fabricated with the LENS blown powder additive manufacturing system. Figure 5.1 shows a preliminary Hopkinson bar compression test for a laminated Ti-6Al-4V/Ti-1B composite. More detailed experiments are required to garner the mechanical stress-strain behavior.
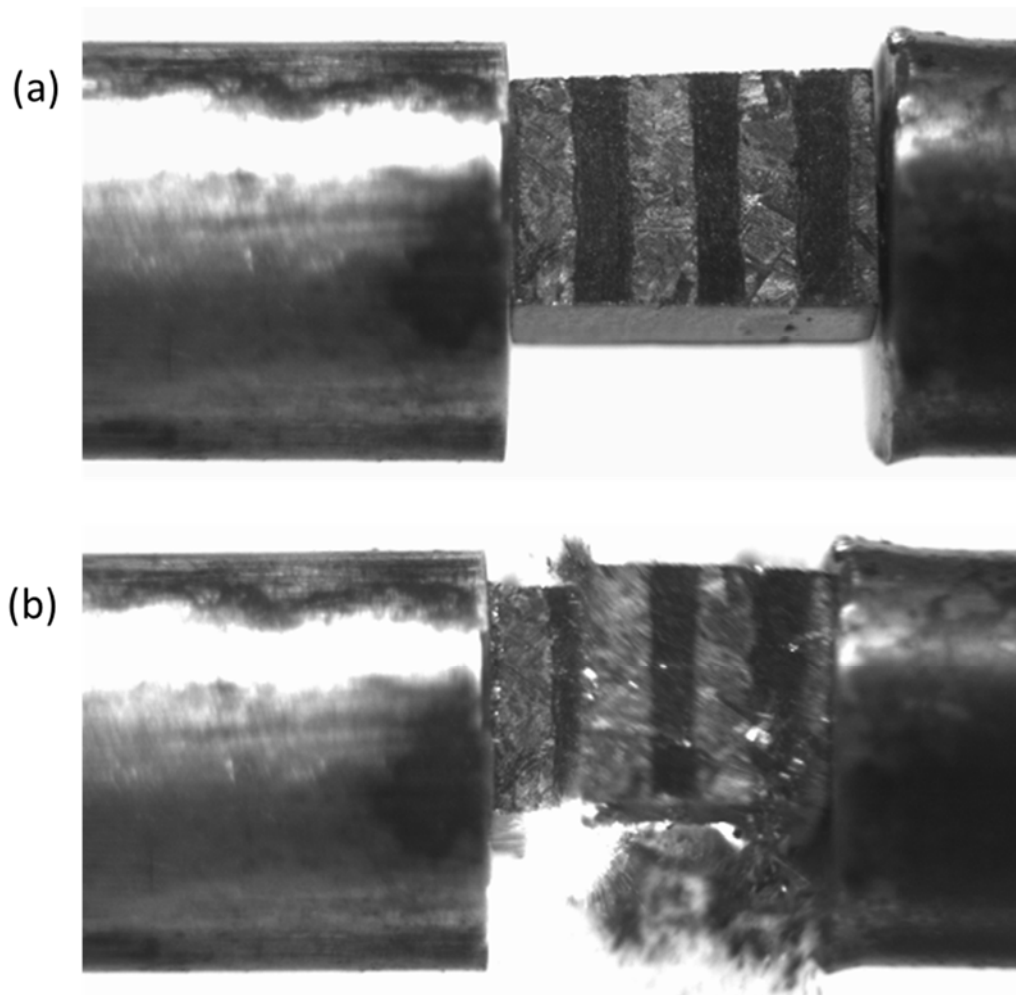
Figure 5.1   High strain rate (~1000/s) Hopkinson bar compression test on a LENS
             produced Ti-6Al-4V/Ti-1B laminate specimen.

The specimen is etched to distinguish layers (a) at the beginning of the test and (b) during
the test.

5.2   Simulating Functionally Graded Materials

The long term objective of this study is to predictively model the behavior of an

assembly of dissimilar materials using the additive manufacturing process. The

experiments conducted herein have been exploratory in nature, while keeping the

modeling and simulation of the material in mind.   The capture of chemical-process-

structure-property relationships from experimental work has paralleled an endeavor to the

model the behavior of the assembly achieved. We are addressing the following question: Can existing material models and simulation tools adequately describe the structures achieved with the additive manufacturing process? Can a single material model be used, or should multiple models be used?

5.2.1   Material Model

Within the titanium-boron system obtained within the processing window in this study, there are a variety of microstructures that were observed including the following: Single phase material (base, substrate) with spatial variation in grain size, spatial variation in particle volume fraction, spatial variation in alloy chemistry affecting modulus. Material models chosen for simulation should implement a microstructural dependence.

Material model possibilities:

- Multi-phase material model

- Single phase with particles as second phase

- Separate material models calibrated for fixed stereology ranges

The region of material described in this study as Borlite represents a eutectic solidification structure formed by TiB, accounting for approximately 10% of the volume fraction, and a titanium matrix, comprising the remainder of the volume fraction. The size and distribution of the TiB volume fraction has been shown in this study to depend on solidification and subsequent thermal processing history. An analogy can be made to hypo-eutectoid steels where the morphology of the eutectoid regions is determined by the cooling rate from the austenitic temperature region through the eutectoid temperature. The morphology difference historically observed by metallographic inspection gave rise

to the terms upper Bainite, lower Bainite, and Pearlite. These three terms are now understood to be associated with size and spacing difference between the ferrite and cementite phases although the total volume fraction is determined by the bulk carbon content of the steel. The mechanical properties of these three eutectoid domains are different, and have been treated computationally with multiphase internal state variable material models {Bammann, 1996 #1142}.

5.3   Material Model Calibration Strategy

Once candidate material models have been populated with stereology quantities from the exploratory experiments, a strategy for model calibration can be developed making use of the DIC method developed in Chapter 3.

5.4   High Strain Rate Experiments

This thesis serves to lay down a first study for understanding the CPSP relationships for a functionally graded titanium armor. What needs to happen next is to study this material under higher applied strain rates than what has been accomplished in this study. To date, we have run lower strain rate tests, but Hopkinson bar experiments will need to be run in order to fully realize the effect of the functionally graded titanium armor.

A preliminary Hopkinson bar test was conducted on a LENS produced Ti-6Al-4V specimen as illustrated in Figure 5.2, which shows a snapshot of the specimen under compression at a strain rate of ~1000/s. Note the white flash was produced by small hot fragments of titanium oxidizing in air. Figure 5.3 shows the compression stress-strain behavior of LENS produced Ti-6Al-4V under two different strain rates (0.01/s and

1500/s) illustrating that as the strain rate increases, the flow stress increases. Figure 5.3

high rate data is associated with the snapshot in Figure 5.2.

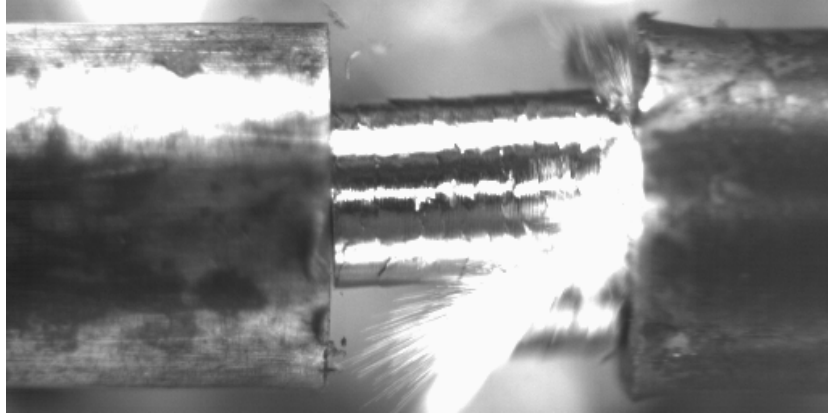Figure 5.2   High strain rate (~1000/s) Hopkinson bar test on a LENS produced Ti-6Al-
4V specimen in compression.

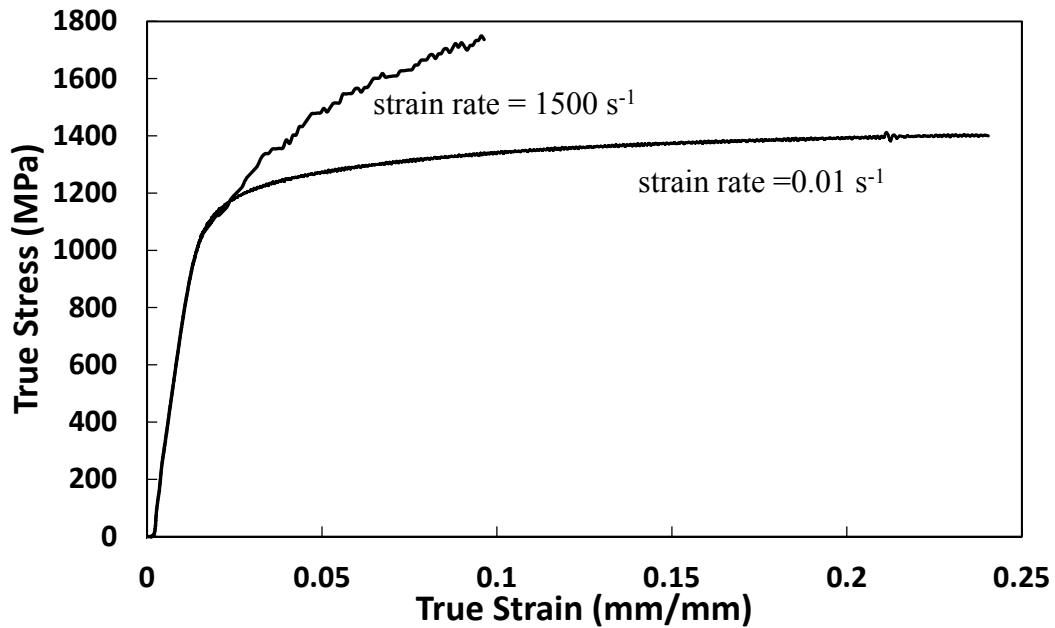Note the white flash was produced by small hot fragments of titanium oxidizing in air.

Figure 5.3   Compression stress-strain behavior of LENS produced Ti-6Al-4V under
two different strain rates (0.01/s and 1500/s)

Note that the flow stress increases as the strain rate increases.

REFERENCES

Ahmed, T. and Rack, H.J., Phase transformations during cooling in α+β titanium alloys, Materials Science and Engineering: A 243(1–2) (1998) 206-211.

Atai, A.A., Nikranjbar, A., Kasiri, R., 2012. Buckling and post-buckling behaviour of semicircular functionally graded material arches: a theoretical study. Proc. Inst. Mech. Eng. Part C J. Mech. Eng. Sci. 226, 607–614. doi:10.1177/0954406211416179

Banerjee, R., Collins, P.C., Fraser, H.L., 2002. Phase evolution in laser-deposited titanium-chromium alloys. Metall. Mater. Trans. A 33, 2129–2138. doi:10.1007/s11661-002-0044-2

Banerjee, R., Collins, P.C., Genç, A., Fraser, H.L., 2003. Direct laser deposition of in situ Ti–6Al–4V–TiB composites. Mater. Sci. Eng. A 358, 343–349. doi:10.1016/S0921-5093(03)00299-5

Banerjee, R., Collins, P.C., Bhattacharyya, D., Banerjee, S., and Fraser, H.L., Microstructural evolution in laser deposited compositionally graded [alpha]/[beta] titanium-vanadium alloys, Acta Materialia 51(11) (2003) 3277-3292.

Banerjee, R., Genç, A., Hill, D., Collins, P.C., Fraser, H.L., 2005. Nanoscale TiB precipitates in laser deposited Ti-matrix composites. Scr. Mater. 53, 1433–1437. doi:10.1016/j.scriptamat.2005.08.014

Beal, V.E., Erasenthiran, P., Ahrens, C.H., Dickens, P., 2007. Evaluating the use of functionally graded materials inserts produced by selective laser melting on the injection moulding of plastics parts. Proc. Inst. Mech. Eng. Part B J. Eng. Manuf. 221, 945–954. doi:10.1243/09544054JEM764

Ben-Dor, G., A. Dubinsky and T. Elperin (1999). "On the order of plates providing the maximum ballistic limit velocity of a layered armor." International Journal of Impact Engineering **22**(8): 741-755.

Birman, V., Byrd, L.W., 2007. Modeling and analysis of functionally graded materials and structures. Appl. Mech. Rev. 60, 195–216.

Brooks, J., Robino, C., Headley, T., Goods, S., Griffith, M., 1999. Microstructure and property optimization of LENS deposited H13 tool steel, in: Proceedings of the Solid Freeform Fabrication Symposium. pp. 375–382.

Cherradi, N., Kawasaki, A., Gasik, M., 1994. Worldwide trends in functional gradient materials research and development. Compos. Eng. 4, 883–894. doi:10.1016/S0961-9526(09)80012-9

Chin, E. S. C. (1999). "Army focused research team on functionally graded armor composites." Materials Science and Engineering A **A259**(2): 155-161.

Corbett, G. G., S. R. Reid and W. Johnson (1996). "Impact loading of plates and shells by free-flying projectiles: A review." International Journal of Impact Engineering 18(2): 141-230.

Crouch, I. G. (1988). "Metallic armour - from cast aluminium alloys to high-strength steels." Materials Forum 12: 31-37.

D. Dimitrov, K. Schreve, N. de Beer, 2006. Advances in three dimensional printing – state of the art and future perspectives. Rapid Prototyp. J. 12, 136–147. doi:10.1108/13552540610670717

El Kadiri, H., Wang, L., Horstemeyer M.F., Yassar, R., Shahbazian, Y., Felicelli, S., Wang, P.T., "Phase Transformations in Low Alloy Steel Laser Deposits," *Materials Science and Engineering A*, Vol. 494, pp. 10-20, 2008.

Feng, H., Meng, Q., Zhou, Y., and Jia, D., Spark plasma sintering of functionally graded material in the Ti-TiB2-B system, Materials Science and Engineering A 397(1-2) (2005) 92-97.

Galvan, D., Ocelík, V., Pei, Y., Kooi, B.J., De Hosson, J.T.M., and Ramous, E., Microstructure and properties of TiB/Ti-6Al-4V coatings produced with laser treatments, Journal of Materials Engineering and Performance 13(4) (2004) 406-412.

Gasik, M.M., 2010. Functionally Graded Materials: bulk processing techniques. Int. J. Mater. Prod. Technol. 39, 20–29. doi:10.1504/IJMPT.2010.034257

Genç, A., Banerjee, R., Hill, D., Fraser, H.L., 2006. Structure of TiB precipitates in laser deposited in situ, Ti-6Al-4V–TiB composites. Mater. Lett. 60, 859–863. doi:10.1016/j.matlet.2005.10.033

Gill, D. (2002). Laser Engineered Net Shaping, Sandia National Labs.

Gorsse, S., Miracle, D.B., 2003. Mechanical properties of Ti-6Al-4V/TiB composites with randomly oriented and aligned TiB reinforcements. Acta Mater. 51, 2427–2442. doi:10.1016/S1359-6454(02)00510-4

Griffith, M.L., Keicher, D.L., Romero, J.A., Atwood, C.L., Harwell, L.D., Greene, D.L., Smugeresky, J.E., 1996. Laser engineered net shaping (LENS) for the fabrication of metallic components (No. SAND--96-1293C; CONF-9605172--1). Sandia National Labs., Albuquerque, NM (United States).

Griffith, M.F., Ensz, M.T., Puskar, J.D., and Robino, C.V., "Understanding the Microstructure and Properties of Components Fabricated by Laser Engineered Net Shaping (LENS)," MRS Online, Vol. 625, 9, 2000

Griffith, M.L., Schliengeral, M.E., Harwell, D., Olivera, M.S., Baldwin, M.D., Ensza, T.E., Essiena, M., Brooks, J., Robinoa, V.R., Smugeresky, J.E., Hofmeister, W.H., Wert, M.J., and Nelson, D.V., "Understanding Thermal Behavior in the LENS Process," *Materials and Design,* Vol. 20, Issues 2-3, pp. 107-113, 1999.

Grujicic, M., Hu, Y., Fadel, G.M., Keicher, D.M., "Optimization of the LENS Rapid Fabrication Process for In-Flight Melting of Feed Powder" *Journal of Materials Synthesis and Processing,* 9: 223, 2001.

Gu, D.D., Meiners,W., Wissenbach, K., Poprawe, R., "Laser additive manufacturing of metallic components: materials, processes and mechanisms," J. Int. Materials Reviews, Vol. 57, Issue 3, 2012.

Gupta, N., Basu, B., Bhanu Prasad, V.V., and Vemuri, M., Ballistic Studies on TiB2-Ti Functionally Graded Armor Ceramics, 2012.

Hammer, J. T., R. S. Yatnalkar, J. D. Seidt and A. Gilat (2013). Plastic deformation of Ti-6Al-4V plate over a wide range of loading conditions, Costa Mesa, CA.

Horstemeyer, M.F., *Integrated Computational Materials Engineering (ICME) for Metals: Reinvigorating Engineering Design with Science*, Chapter 10, Wiley Press, 2012.

Hutmacher, D.W., Sittinger, M., Risbud, M.V., 2004. Scaffold-based tissue engineering: rationale for computer-aided design and solid free-form fabrication systems. Trends Biotechnol. 22, 354–362. doi:10.1016/j.tibtech.2004.05.005

ImageJ [WWW Document], 1997. URL https://imagej.nih.gov/ij/

Jackson, T.R., Liu, H., Patrikalakis, N.M., Sachs, E.M., Cima, M.J., 1999. Modeling and designing functionally graded material components for fabrication with local composition control. Mater. Des. 20, 63–75. doi:10.1016/S0261-3069(99)00011-4

Jha, D. K., T. Kant and R. K. Singh (2013). "A critical review of recent research on functionally graded plates." Composite Structures **96**: 833-849.

Kawasaki, A., Watanabe, R., 2002. Thermal fracture behavior of metal/ceramic functionally graded materials. Eng. Fract. Mech. 69, 1713–1728. doi:10.1016/S0013-7944(02)00054-1

Keicher, D.M., Miller, W.D., 1998. LENSTM moves beyond RP to direct fabrication. Met. Powder Rep. 12, 26–28.

Kieback, B., Neubrand, A., Riedel, H., 2003. Processing techniques for functionally graded materials. Mater. Sci. Eng. A, Papers from the German Priority Programme (Functionally Graded Materials) 362, 81–106. doi:10.1016/S0921-5093(03)00578-1

Kimura, H., Toda, K., 1997. Design and development of graded materials by pulse discharge resistance consolidation. Met. Powder Rep. 51, 34.

Kleponis, D. S. M., Audrey L; Filbey, Gordon L (2000). Material Design Paradigms for Optimal Functional Gradient Armors. 14th Engineering Mechanics Conference, Austin, Tx.

Kobryn, P. A., and S. L. Semiatin. "The laser additive manufacture of Ti-6Al-4V." *Jom* 53, no. 9 (2001): 40-42.

Kou, X.Y., Parks, G.T., Tan, S.T., 2012. Optimal design of functionally graded materials using a procedural model and particle swarm optimization. Comput.-Aided Des. 44, 300–310. doi:10.1016/j.cad.2011.10.007

Lepakova, O. K., L. G. Raskolenko, *et al*., "Titanium borides prepared by self-propagating high-temperature synthesis." *Inorganic Materials* **36**(6): 568-575, 2000.

Li, T., E. A. Olevsky and M. A. Meyers (2008). "The development of residual stresses in Ti6Al4V-Al3Ti metal-intermetallic laminate (MIL) composites." Materials Science and Engineering: A **473**(1–2): 49-57.

Li, X.C., Stampfl, J., Prinz, F.B., 2000. Mechanical and thermal expansion behavior of laser deposited metal matrix composites of Invar and TiC. Mater. Sci. Eng. A 282, 86–90. doi:10.1016/S0921-5093(99)00781-9

Lin, X., Yue, T.M., 2005. Phase formation and microstructure evolution in laser rapid forming of graded SS316L/Rene88DT alloy. Mater. Sci. Eng. A 402, 294–306. doi:10.1016/j.msea.2005.05.024

Liu, W. and DuPont, J.N., "Fabrication of functionally graded TiC/Ti composites by laser engineered net shaping," Scripta Materialia, 48, No. 9, pp. 1337-1342, 2003.

Liu, W. K., L. Siad, R. Tian, S. Lee, D. Lee, X. Yin, W. Chen, S. Chan, G. B. Olson, L. E. Lindgen, M. F. Horstemeyer, Y. S. Chang, J. B. Choi and Y. J. Kim (2009). "Complexity science of multiscale materials via stochastic computations." International Journal for Numerical Methods in Engineering **80**(6-7): 932-978.

Liu, X., C. Tan, J. Zhang, Y. Hu, H. Ma, F. Wang and H. Cai (2009). "Influence of microstructure and strain rate on adiabatic shearing behavior in Ti–6Al–4V alloys." Materials Science and Engineering: A **501**(1–2): 30-36.

99

Lu, L., Chekroun, M., Abraham, O., Maupin, V., Villain, G., 2011. Mechanical properties estimation of functionally graded materials using surface waves recorded with a laser interferometer. NDT E Int. 44, 169–177. doi:10.1016/j.ndteint.2010.11.007

Malinina, M., Sammi, T., Gasik, M.M., 2005. Corrosion Resistance of Homogeneous and FGM Coatings. Mater. Sci. Forum 492–493, 305–310. doi:10.4028/www.scientific.net/MSF.492-493.305

Marin, L., 2005. Numerical solution of the Cauchy problem for steady-state heat transfer in two-dimensional functionally graded materials. Int. J. Solids Struct. 42, 4338–4351. doi:10.1016/j.ijsolstr.2005.01.005

Matsuo, S., Watari, F., Ohata, N., 2001. Fabrication of a Functionally Graded Dental Composite Resin Post and Core by Laser Lithography and Finite Element Analysis of its Stress Relaxation Effect on Tooth Root. Dent. Mater. J. 20, 257–274. doi:10.4012/dmj.20.257

www.matweb.com/search/DataSheet.aspx?MatGUID=7bfbc80cc75449cebd59078ee2a40&ckck=1, Boron, 2017

Miyamoto, Y., 2000. Development of Functionally Graded Materials by HIP. J. Soc. Mater. Sci. Jpn. 49, 3–8. doi:10.2472/jsms.49.3Appendix_3

Müller, E., Drašar, Č., Schilz, J., Kaysser, W.A., 2003. Functionally graded materials for sensor and energy applications. Mater. Sci. Eng. A, Papers from the German Priority Programme (Functionally Graded Materials) 362, 17–39. doi:10.1016/S0921-5093(03)00581-1

Mumtaz, K.A., Hopkinson, N., 2007. Laser melting functionally graded composition of Waspaloy®. J. Mater. Sci. 42, 7647–7656. doi:10.1007/s10853-007-1661-3

Nemat-Nasser, S., W.-G. Guo, V. F. Nesterenko, S. S. Indrakanti and Y.-B. Gu (2001). "Dynamic response of conventional and hot isostatically pressed Ti–6Al–4V alloys: experiments and modeling." Mechanics of Materials **33**(8): 425-439.

Nicholas, T., Material behavior at high strain rates, Report AFWAL-TR-80-4053, USAF Wright Aeronautical Laboratories, Wright-Patterson Air Force Base, OH, USA, 1980.

Niino, M., Hirai, T., Watanabe, R., 1987. The functionally gradient materials. J Jap Soc Comp Mater 13, 257.

Niino, M., Kisara, K., Mori, M., 2005. Feasibility Study of FGM Technology in Space Solar Power Systems (SSPS). Mater. Sci. Forum 492–493, 163–170. doi:10.4028/www.scientific.net/MSF.492-493.163

Ocelík, V., Matthews, D., De Hosson, J.T.M., 2005. Sliding wear resistance of metal matrix composite layers prepared by high power laser. Surf. Coat. Technol. 197, 303–315. doi:10.1016/j.surfcoat.2004.09.003

Olatunji-Ojo, A.O., Boetcher, S.K.S., Cundari, T.R., 2012. Thermal conduction analysis of layered functionally graded materials. Comput. Mater. Sci. 54, 329–335. doi:10.1016/j.commatsci.2011.10.006

Pei, Y.T., Ocelík, V., De Hosson, J.T.M., 2003. Interfacial adhesion of laser clad functionally graded materials. Mater. Sci. Eng. A 342, 192–200. doi:10.1016/S0921-5093(02)00249-6

Peirs, J., P. Verleysen, W. Van Paepegem and J. Degrieck (2011). "Determining the stress-strain behaviour at large strains from high strain rate tensile and shear experiments." International Journal of Impact Engineering **38**(5): 406-415.

Pompe, W., Worch, H., Epple, M., Friess, W., Gelinsky, M., Greil, P., Hempel, U., Scharnweber, D., Schulte, K., 2003. Functionally graded materials for biomedical applications. Mater. Sci. Eng. A, Papers from the German Priority Programme (Functionally Graded Materials) 362, 40–60. doi:10.1016/S0921-5093(03)00580-X

Ruocco, E., Minutolo, V., 2012. Two-dimensional stress analysis of multiregion functionally graded materials using a field boundary element model. Compos. Part B Eng. 43, 663–672. doi:10.1016/j.compositesb.2011.08.013

Sato, Tomotoshi, Effect of Solidification Conditions upon the Primary Dendrite Arm Spacing, Nippon Kinzoku Gakkai-si. 46. 232-236. 10.2320/jinstmet1952.46.2_232. 1982.

Seely, D.W., Bagheri, M.A., Rhee, H., Wang, P.T., Dickel, D.E., Garrett, M., and Horstemeyer, M.F., "A Functionally Graded Titanium Based Alloy for High Throughput Structure-Property Experiments," submitted to Materials Science A, 2018.

Sen, I., S. Tamirisakandala, D. B. Miracle and U. Ramamurty (2007). "Microstructural effects on the mechanical behavior of B-modified Ti–6Al–4V alloys." Acta Materialia 55(15): 4983-4993.

Schatt, W., 1992. Sintervorgänge: Grundlagen. VDI-Verlag.

Schwendner, K.I., Banerjee, R., Collins, P.C., Brice, C.A., Fraser, H.L., 2001. Direct laser deposition of alloys from elemental powder blends. Scr. Mater. 45, 1123–1129. doi:10.1016/S1359-6462(01)01107-1

Shanmugavel, P., Bhaskar, G.B., Chandrasekaran, M., Mani, P.S., Srinivasan, S.P., 2012. An overview of fracture analysis in functionally graded materials. Eur. J. Sci. Res. 68, 412–439.

Tabor, D., The hardness of metals, Oxford University Press, 2000.

Templeton, D. W. (2007). COMPUTATIONAL STUDY OF A FUNCTIONALLY GRADED CERAMIC-METALLIC ARMOR. 23RD INTERNATIONAL SYMPOSIUM ON BALLISTICS, Tarragona, Spain.

Wang, S.S., 1983. Fracture Mechanics for Delamination Problems in Composite Materials. J. Compos. Mater. 17, 210–223. doi:10.1177/002199838301700302

Wang, L. T., Thompson, T., "Self-Propagating High-Temperature synthesis and Dynamic Compaction of Titanium Boride and Titanium Carbide," Army Research Laboratory**:** 51, 1999.

Wang, L., Felicelli, S., Gooroochurn, Y., Wang, P.T., Horstemeyer, M.F., "Optimization of the LENS Process for Steady Molten Pool Size," *Materials Science and Engineering:A*, Vol. 474, Issues 1-2, pp. 148-156, 2008.

Wang, L. T., Levi T. (1999). Self-Propagating High-Temperature synthesis and Dynamic Compaction of Titanium Boride and Titanium Carbide, Army Research Laboratory**:** 51.

Watanabe, Y., Inaguma, Y., Sato, H., Miura-Fujiwara, E., 2009. A Novel Fabrication Method for Functionally Graded Materials under Centrifugal Force: The Centrifugal Mixed-Powder Method. Materials 2, 2510–2525. doi:10.3390/ma2042510

Watari, F., Yokoyama, A., Omori, M., Hirai, T., Kondo, H., Uo, M., Kawasaki, T., 2004. Biocompatibility of materials and development to functionally graded implant for bio-medical application. Compos. Sci. Technol., Functional Biocomposite Materials 64, 893–908. doi:10.1016/j.compscitech.2003.09.005

Woodward, B., Kashtalyan, M., 2012. Performance of functionally graded plates under localised transverse loading. Compos. Struct. 94, 2254–2262. doi:10.1016/j.compstruct.2012.02.012

Xue, Y., Pascu, A., Horstemeyer, M.F., Wang, L., and Wang, P.T., "Microporosity effects on cyclic plasticity and fatigue of LENS-processed steel," Acta Materialia, Vol. 58, 4029-4038, 2010.

Xing, A., Jun, Z., Chuanzhen, H., Jianhua, Z., 1998. Development of an advanced ceramic tool material—functionally gradient cutting ceramics. Mater. Sci. Eng. A 248, 125–131. doi:10.1016/S0921-5093(98)00502-4

Yue, T.M., Li, T., 2008. Laser cladding of Ni/Cu/Al functionally graded coating on magnesium substrate. Surf. Coat. Technol. 202, 3043–3049. doi:10.1016/j.surfcoat.2007.11.007

Zukas, J. A., T. Nicholas, H. F. Swift, L. B. Greszczuk, D. R. Curran and L. Malvern (1983). "Impact dynamics." Journal of Applied Mechanics **50**: 702.

Zukas, J. A., W. Walters and W. W. P. Walters (2002). Explosive effects and applications, Springer.